NASA/TM—2013-217901

The Mechanical Properties of Candidate Superalloys for a Hybrid Turbine Disk

Timothy P. Gabb, Rebecca A. MacKay, Susan L. Draper, Chantal K. Sudbrack, and Michael V. Nathal
Glenn Research Center, Cleveland, Ohio

July 2013

NASA STI Program . . . in Profile

Since its founding, NASA has been dedicated to the advancement of aeronautics and space science. The NASA Scientific and Technical Information (STI) program plays a key part in helping NASA maintain this important role.

The NASA STI Program operates under the auspices of the Agency Chief Information Officer. It collects, organizes, provides for archiving, and disseminates NASA's STI. The NASA STI program provides access to the NASA Aeronautics and Space Database and its public interface, the NASA Technical Reports Server, thus providing one of the largest collections of aeronautical and space science STI in the world. Results are published in both non-NASA channels and by NASA in the NASA STI Report Series, which includes the following report types:

- TECHNICAL PUBLICATION. Reports of completed research or a major significant phase of research that present the results of NASA programs and include extensive data or theoretical analysis. Includes compilations of significant scientific and technical data and information deemed to be of continuing reference value. NASA counterpart of peer-reviewed formal professional papers but has less stringent limitations on manuscript length and extent of graphic presentations.

- TECHNICAL MEMORANDUM. Scientific and technical findings that are preliminary or of specialized interest, e.g., quick release reports, working papers, and bibliographies that contain minimal annotation. Does not contain extensive analysis.

- CONTRACTOR REPORT. Scientific and technical findings by NASA-sponsored contractors and grantees.

- CONFERENCE PUBLICATION. Collected papers from scientific and technical conferences, symposia, seminars, or other meetings sponsored or cosponsored by NASA.

- SPECIAL PUBLICATION. Scientific, technical, or historical information from NASA programs, projects, and missions, often concerned with subjects having substantial public interest.

- TECHNICAL TRANSLATION. English-language translations of foreign scientific and technical material pertinent to NASA's mission.

Specialized services also include creating custom thesauri, building customized databases, organizing and publishing research results.

For more information about the NASA STI program, see the following:

- Access the NASA STI program home page at *http://www.sti.nasa.gov*

- E-mail your question to *help@sti.nasa.gov*

- Fax your question to the NASA STI Information Desk at 443–757–5803

- Phone the NASA STI Information Desk at 443–757–5802

- Write to:
  STI Information Desk
  NASA Center for AeroSpace Information
  7115 Standard Drive
  Hanover, MD 21076–1320

NASA/TM—2013-217901

The Mechanical Properties of Candidate Superalloys for a Hybrid Turbine Disk

Timothy P. Gabb, Rebecca A. MacKay, Susan L. Draper, Chantal K. Sudbrack, and Michael V. Nathal
Glenn Research Center, Cleveland, Ohio

National Aeronautics and
Space Administration

Glenn Research Center
Cleveland, Ohio 44135

July 2013

Acknowledgments

Jonathan Yu of Stanford University is acknowledged for imaging oxidized LDS specimens.

This work was sponsored by the Fundamental Aeronautics Program at the NASA Glenn Research Center.

Level of Review: This material has been technically reviewed by technical management.

Available from

NASA Center for Aerospace Information
7115 Standard Drive
Hanover, MD 21076–1320

National Technical Information Service
5301 Shawnee Road
Alexandria, VA 22312

Available electronically at http://www.sti.nasa.gov

The Mechanical Properties of Candidate Superalloys for a Hybrid Turbine Disk

Timothy P. Gabb, Rebecca A. MacKay, Susan L. Draper, Chantal K. Sudbrack, and Michael V. Nathal
National Aeronautics and Space Administration
Glenn Research Center
Cleveland, Ohio 44135

Abstract

The mechanical properties of several cast blade superalloys and one powder metallurgy disk superalloy were assessed for potential use in a dual alloy hybrid disk concept of joined dissimilar bore and web materials. Grain size was varied for each superalloy class. Tensile, creep, fatigue, and notch fatigue tests were performed at 704 to 815 °C. Typical microstructures and failure modes were determined. Preferred materials were then selected for future study as the bore and rim alloys in this hybrid disk concept. Powder metallurgy superalloy LSHR at 15 μm grain size and single crystal superalloy LDS-1101+Hf were selected for further study, and future work is recommended to develop the hybrid disk concept.

Introduction

Systems studies (Refs. 1 to 3) have shown that in order to achieve substantial gains in fuel efficiency, higher operating temperatures are needed. Furthermore, the turbine and compressor disks are viewed as key components that limit operating temperatures. A disk rim temperature of 815 °C is considered necessary to achieve NASA's N+3 goals for subsonic commercial aircraft. Disk superalloy mechanical properties are relatively stable from room temperature up to 650 °C, but vary at higher temperatures due to time-dependent effects (Refs. 1 and 2). Powder metallurgy disk alloys such as ME3 (also known as Rene´ 104 and ME16) (Ref. 3), Alloy 10 (Refs. 4 and 5), LSHR (Ref. 6), have been designed to allow rim temperature capabilities up to 704 °C for selected applications. Such capabilities allow higher compressor exit temperatures, and also allow the full utilization of advanced combustor and airfoil concepts under development. Attempts to optimize powder metallurgy superalloys for higher temperatures have shown some encouraging thought that additional improvements may still be possible (Refs. 7 to 9). However, work has shown that tensile, creep, and fatigue properties of these alloys are limited at higher temperatures approaching 815 °C, due to enhanced time-dependent deformation combined with environmental degradation (Refs. 10 to 13).

It is well known that the tensile, creep, and dwell fatigue crack initiation and growth properties of disk superalloys at elevated temperatures can vary significantly with heat treatments influencing grain size and γ' precipitate size distributions (Refs. 1 and 2). Yet, the three properties cannot be simultaneously maximized with the same heat treatment and microstructure, and compromises become more difficult with increasing temperatures. For example, faster cooling rates after solution heat treatments have been shown to improve tensile and creep resistance, but can harm ductility and dwell fatigue crack initiation and growth resistance. Processing-microstructure models are in active development (Refs. 2 and 14) that could potentially indicate how processing paths can best tailor such microstructural features and resulting mechanical properties. Yet, the advantages available through optimization of processing for a "single" target microstructure decrease with increasing temperatures.

Due to the mass of disks and the dependence of heat transfer on section size, variations in solution and aging heat treatment temperature paths within a disk are inevitable, which result in variations in microstructure. "Dual" microstructure disks with purposefully varied grain and precipitate microstructures for the disk bore and rim have been shown to offer benefits for optimizing the

microstructure for these different disk locations (Refs. 3, 6, 15, and 16). Dual alloy disks have been studied in the past to further tailor properties with location in the disk, using a powder metallurgy disk superalloy optimized for high strength and fatigue resistance in the bore, joined to another powder metallurgy disk superalloys optimized for creep resistance in the rim (Ref. 17). More recent work has studied combining a powder metallurgy disk superalloy bore to a more dissimilar, higher temperature rim material, a cast polycrystalline blade superalloy (Ref. 18). There has also been work to braze cast single crystal superalloy rim firtrees onto powder metal disk superalloy webs (Ref. 19).

The objective of this study was to screen the mechanical properties possible through choosing different bore and rim materials, for a hybrid material disk concept of joined dissimilar bore and web materials. Several cast blade superalloys and one powder metallurgy disk superalloy were assessed with varied grain sizes. Tensile stress relaxation, creep, uniform gage fatigue, and notch fatigue tests were performed at 704 to 815 °C. The compromises among properties were compared and related to the microstructures and failure modes observed.

Materials and Test Procedures

Materials

The compositions in weight percent of all tested materials are listed in Table 1. LSHR superalloy powder was obtained from Special Metals Corp. The powder was atomized in argon, canned, hot isostatically pressed, extruded and isothermally forged into flat disks. The forging conditions were intentionally varied, to enable different grain sizes after heat treatment (Ref. 20). Rectangular blanks about 1.5 cm square and 5 to 6 cm long were then extracted from forged pancakes. The blanks were placed vertically in a closed fixture in air and supersolvus solution heat treated at 1171 °C for 2 h in a resistance heating furnace. The fixture was then removed to cool in static air. The average cooling rate of the blank cores was 72 °C per minute. They were given an aging heat treatment of 855 °C for 4 h plus 775 °C for 8 h. The blanks were then machined into tensile, creep, and fatigue specimens. Additional blanks of the same dimensions from the rim of an existing dual microstructure heat treated disk of LSHR containing only 0.03 wt% carbon and subjected to similar processing (Ref. 6) were solution heat treated at 1171 °C for 10 min to dissolve all γ′ and cooled in the same fixture. They were also given an aging heat treatment of 855 °C for 4 h plus 775 °C for 8 h.

Mar-M247LC and Rene′ 80 bars were each conventionally cast at PCC, Inc. in a mold of 18 bars using standard casting practices. Additional bars of Mar-M247LC and Rene′ 80 were cast using a microcast process to produce finer grain size. All bars had a nominal diameter of 1.9 cm and length of 15 cm. They were subsequently hot isostatically pressed using standard industry practices. All bars were then solution heat treated in a vacuum furnace at 1221 °C for 2 h with an average argon gas quench rate of 102 °C/min, and aging heat treated at 1079 °C for 4 h with an argon gas quench rate of 92 °C/min., then 871 °C for 20 h and cooled in static air.

Low density, single crystal blade superalloy LDS-1101+Hf, LDS-1101, and LDS-4583 slabs (Refs. 21 and 22) were cast at PCC Airfoils, LLC using standard single crystal casting practices. The slabs each had a nominal width of 5 cm and length of 15 cm, and thicknesses of 0.6 or 1.3 cm. All slabs were solution heat treated for 6 h between 1306 and 1315 °C in a vacuum furnace backfilled with argon, and quenched with argon gas at 43 °C/min to below 1093 °C. Additional details are given in Reference 21. Slabs were then macro-etched and X-rayed, to insure they contained no high angle grain boundaries. They were subsequently heat treated at 1079 °C for 4 h, and aging heat treated at 871 °C for 12 h, with each step performed in vacuum furnaces backfilled with argon gas, at cooling rates near 30 °C/min. and 22 °C/min., respectively. All LDS alloy specimen blanks were extracted so as to be oriented within 8° of the [001] crystallographic direction.

Test Procedures

Tensile tests were performed at the NASA Glenn Research Center (GRC) at 704, 760, and 815 °C on specimens having a nominal gage diameter of 0.41 cm and gage length of 2.1 cm, in a servo-hydraulic testing machine using a resistance heating furnace and axial extensometer, in general accordance with ASTM E21-09. However, tests initiated at the required strain rate of 0.5 percent per min. were interrupted at a strain of 1 percent, and held there for 100 h to measure relaxation of stress as a function of time. They were subsequently tested to failure at a faster average strain rate of 5 percent per min.

Creep tests were performed at NASA GRC on specimens having a nominal gage diameter of 0.32 cm and gage length of 2.1 cm in lever arm constant load creep frames using resistance heating furnaces and shoulder-mounted extensometers, according to ASTM E139-06. These tests were performed at 704 °C with a stress of 793 MPa, 760 °C with a stress of 620 MPa, and at 815 °C with a stress of 448 MPa, and were all continued to rupture.

Notched gage fatigue tests were performed on cylindrical notched specimens (Fig. 1) having a geometric elastic stress concentration factor (K_t) of 2.0. The notch was consistently low-stress ground, then polished parallel to the loading direction to not exceed 0.21 μm average roughness. All these specimens were tested using uniaxial closed-loop servo-hydraulic testing machines with resistance heating furnaces at NASA GRC, in accordance with load-controlled fatigue test specification ASTM E466-07. Notched dwell fatigue resistance was screened using cyclic dwell waveforms which first cycled stress at a frequency of 0.5 Hz and minimum/maximum stress ratio (R_σ) of 0.05, then imposed a dwell at minimum stress for 90 s. This dwell cycle allows minimal time-dependent relaxation of stresses at the notch, and has been shown to be very detrimental to the fatigue life of several disk superalloys (Refs. 23 to 25). These tests were performed at 704 °C with a maximum net section stress of 793 MPa, and at 815 °C with maximum stresses of 621 and 448 MPa. Several additional tests were also performed at 815 °C with maximum stresses of 621 MPa with dwells of 90 s at maximum stress, and with conventional triangular waveforms cycling stress at a constant frequency of 0.33 Hz and R_σ of 0.05.

Machining and testing of uniform gage low cycle fatigue specimens for selected materials, having a gage diameter of 0.64 cm across a gage length of 1.9 cm, were performed by Mar-Test, Inc. These specimens were machined using a low stress grinding procedure, and the gage sections were then polished parallel to the loading direction, in order to not exceed 0.21 μm average roughness. Uniform gage specimens were tested using uniaxial closed-loop servo-hydraulic testing machines with axial extensometers and either induction heating or resistance heating furnaces. The tests were performed according to ASTM E606, with strain initially controlled to fixed limits. Tests were performed using a triangular waveform for the first 24 h of cycling, varying strain at a frequency of 0.5 Hz at a minimum/maximum strain ratio (R_ε) of 0. After 24 h of testing in this manner, surviving specimen tests were completed using a triangular load-controlled waveform at a faster frequency of 10 Hz, which maintained the cyclic stresses stabilized before interruption.

Grain and γ' precipitate microstructures were surveyed using optical and field emission scanning electron microscopy on etched metallographically-prepared sections. Grain sizes were determined from metallographic sections swab etched with waterless Kallings solution, according to ASTM E112-10 linear intercept procedures, using circular grid overlays on optical images. For Mar-M247LC, grain sizes were also determined by electron backscatter diffraction, for additional confirmation. γ' precipitate sizes were determined from metallographic sections etched with 33 percent acetic acid, 33 percent nitric acid, 33 percent H_2O, 1 percent HF by volume, with the area of each precipitate measured using SigmaScan 5.0 (Jandel Corporation) image analysis software. Fracture surfaces were examined to determine failure initiation sites using scanning electron microscopy.

Statistical analyses of variance for strengths and lives were performed using JMP10 (SAS Institute Inc.) software, with a probability of 95 percent required to conclude significant differences among the materials.

Results and Discussion

Microstructures

Mean linear intercept grain size and mean dimensions of secondary and tertiary γ' precipitates are listed for the test materials in Table 2. Grain microstructures are shown in Figure 2. Fine grain LSHR had the smallest grain size of 15 μm, while coarse grain LSHR having 0.05 C and 0.03 C possessed comparable grain sizes of about 50 μm, Figure 2(a) to (c). Microcast Rene´ 80 had a grain size of 200 μm, while conventionally cast Rene´ 80 had an intermediate grain size of 600 μm, Figure 2(d) and (e). Microcast Mar-M247LC had a similar, uniform grain size of about 60 μm, Figure 2(f). Conventionally cast Mar-M247LC (Fig. 2(g)) had the largest grain size among the polycrystalline materials, averaging 1,200 μm. However, these grains were often further elongated in the radial direction from the center of each bar.

Secondary and tertiary γ′ precipitates of the test materials are shown in Figure 3. Secondary precipitate shapes ranged from a mixture of spheres and rounded cubes in LSHR and Mar-M247LC to highly cuboidal in LDS1101+Hf. Tertiary precipitate shapes were consistently spherical, Figure 3(i). The area of each precipitate was measured, and the equivalent radius of a spherical particle is also compared in Table 2. The three tested LSHR materials had comparable, smallest mean secondary γ′ sizes (Fig 3(a) to (c)), followed by Rene´ 80 (Fig. 3(d) and (e)) and LDS-1101+Hf (Fig. 3(h)), and then Mar-M247LC with largest mean sizes (Fig. 3(f) and (g)). Mar-M247LC in both conventionally cast and microcast forms had larger and more highly variable secondary γ´ precipitate sizes (Fig. 4) than Rene′ 80, LSHR, and LDS-1101+Hf, with variability indicated by the large standard deviations measured. Mar-M247LC also had largest mean tertiary γ′ sizes. LDS1101+Hf had very uniform secondary γ´ precipitates, but no appreciable tertiary γ´ precipitates. MC carbides were often observed within grains of all the polycrystalline superalloys, while MC and $M_{23}C_6$ carbides and M_3B_2 borides were observed along grain boundaries of LSHR (Ref. 26), Mar-M247LC (Ref. 27), and Rene´ 80 (Ref. 28). LDS-1101+Hf had MC carbides (Ref. 22), but no borides were detected.

Comparisons of Mechanical Properties and Failure Modes

Tensile Response

Measured elastic modulus and yield strength at 0.1 percent offset plastic strain are compared as functions of temperature in Table 3. As extensively reported (Refs. 1 and 2), single crystal superalloys have about half the longitudinal elastic modulus of polycrystalline superalloys when loaded in the [001] crystallographic direction. Therefore, tensile tests interrupted at 1 percent total strain for measurement of stress relaxation produced significantly less plastic strain in LDS than for polycrystalline superalloys, as indicated in Figure 5. For this reason, yield strength was compared at 0.1 percent offset plastic strain (Fig. 6), as opposed to the more commonly reported value at 0.2 percent offset. This comparative reduction in plastic strain generated for single crystal materials could also occur at strain-limited locations near notches, slots, and bolt holes of a disk, in both monotonic and fatigue loading. However, elastic-plastic multiaxial stress analyses would be needed to fully estimate these effects.

Tensile tests were interrupted at a total strain of 1 percent, and held there for 100 h to measure relaxation of stress as a function of time. Comparisons for all materials of relaxed stress versus time in typical tests at 704 to 815 °C are shown in Figure 5. Stress values at 0, 1, 10, and 100 h of relaxation are also compared in Table 3, with 100 h relaxed stress also shown in Figure 6. Among polycrystalline alloys, LSHR and Rene′ 80 allowed more stress relaxation than Mar-M247LC at each temperature. Finer grain size usually allowed more stress relaxation for each material, though Rene´ 80 at 200 and 600 μm grain sizes had very similar responses. Most polycrystalline superalloys had rapid initial stress relaxation, which slowed down with increasing time. This produced near linear response of stress with logarithm of time for the polycrystalline superalloys, Figure 5. Unlike most of the polycrystalline superalloys, LDS-1101+Hf had an initial "incubation" period of minimal stress relaxation which decreased with increasing

temperature, followed by a period of moderate stress relaxation. Polycrystalline 1,200 μm Mar-M247LC also had an initial "incubation" period of minimal stress relaxation, in tests at 704 and 760 °C. But overall, LDS-1101+Hf allowed the least stress relaxation at each temperature of the tested materials, which will be shown to correlate with higher creep resistance.

Comparisons of typical tensile stress versus average strain response at average strain rate of 5 percent per minute up to failure, after stress relaxation for 100 h, are in Figure 7. Ultimate strength and ductility as indicated by elongation and reduction in area after failure are also compared in Table 3, and plotted in Figure 8. LSHR at 15 and 30 μm grain sizes had higher yield and ultimate strengths than all other tested materials at 704 °C. But at the 815 °C goal rim temperature, LDS-1101+Hf had higher ultimate strength than all other materials at a significance of over 99 percent.

Yield strength and ultimate strength are shown versus varied grain size for LSHR, Mar-M247LC, and Rene´ 80 in Figure 9. Yield strength decreased with increasing grain size in both LSHR and Mar-M247LC at 704 °C, as indicated by the negative slopes in Figure 9. This is consistent with data obtained at room temperature and 760 °C in various superalloys (Ref. 29) as well as other materials. However at 815 °C, ultimate strength increased with increasing grain size for both LSHR and Mar-M247LC. Increasing grain size can improve resistance to grain boundary sliding often encountered at higher temperatures near 815 °C (Ref. 2), which could account for this reversal in response with increasing temperature. However, composition, precipitate size, and precipitate content of the materials would also influence their strengths. Composition effects could well reflect the response of Rene´ 80, consistently having lowest strengths among the materials at all three tested temperatures. 15 and 50 μm LSHR had highest ductilities at 704 °C, but LDS-1101+Hf had highest ductility at 815 °C. 1,200 and 60 μm Mar-M247LC had consistently low ductility at all tested temperatures. Rene´ 80 had intermediate ductility at each tested temperature.

Tensile failure modes are compared in Figures 10 and 11. At 704 °C (Fig. 10), tensile failures of polycrystalline specimens often initiated at the surface, cracking at surface grain boundaries (Fig. 10(a), (d), (f), and (g)) or across relatively large grains (Fig. 10(b), (c), and (e)). At 815 °C (Fig. 11), polycrystalline tensile specimens more consistently initiated failure from oxidized intergranular surface cracks and propagated by transgranular microvoid coalescence. The surface cracks were occasionally associated with surface carbides that had oxidized. As the test temperature increased from 704 to 815 °C, grain boundaries preferentially cracked in comparison to grain interiors as evidenced by the increased frequency and depth of intergranular cracking with increasing temperature. Conventionally cast MarM247C and Rene´ 80, with their large grain sizes, had surface cracks that tended to be widely-spaced due to the large grain size. Single-crystal LDS-1101+Hf samples fractured on a plane at 45° to the tensile axis at all three test temperatures. The number of slip traces on the specimen increased with increasing temperature. Occasionally, cracks initiated at MC carbides on the specimen surface, as shown in Figure 10(h).

Creep Response

Constant load creep rupture testing was performed under the following conditions: 704 °C/793 MPa; 760 °C/621 MPa; and 815 °C/448 MPa. Times to 0.1, 0.2, 1, and 2 percent creep, as well as rupture are listed in Table 4 for all materials tested. Creep curves of strain versus time are displayed in Figures 12(a) to (c) for these tests at 704, 760, and 815 °C, respectively. At each temperature, the full creep curve to rupture is shown in Figure 12 on the left and the shorter time creep curve displaying up to 1 percent creep strain is shown on the right. It is evident that single crystal LDS-1101+Hf had far superior creep rupture resistance compared to all polycrystalline materials, with about a factor of ten times longer rupture lives between 704 and 815 °C. Times to 1 percent creep strain for single crystal LDS were also longer at all temperatures compared to the polycrystalline materials, except at 704 °C (Fig. 12(a)), where the longest times to 1 percent creep were observed for 60 μm grained Mar-M247 LC and all grain sizes of LSHR. Times for 0.2 percent creep strain were comparable at 704 °C for LDS and LSHR and exceeded those for 60 μm Mar-M247LC and Rene´ 80.

Clearly, the alloy composition can be expected to influence the resultant creep properties and Table 1 shows distinct compositional differences among alloys. LDS-1101+Hf contains high Mo and Re levels for creep strengthening and high Al and Ta contents for γ' precipitation. The polycrystalline materials contain lower quantities of refractories and of γ'—formers, both of which reduce overall creep resistance. As compared to the other polycrystalline alloys, Mar-M247LC contains a high W content for improved creep resistance of superalloys (Ref. 2) through solid solution hardening and has higher contents of γ' formers Al, Hf, Ta, and Ti. As a result, Mar-M247LC has ~70 vol% of γ' precipitates (Ref. 26), compared to 57 vol% γ' in LSHR (Ref. 26). Similarly, LSHR contains more W and higher contents of the γ' formers Al, Nb, and Ta than Rene´ 80. Rene´ 80 exhibited the lowest creep resistance of all alloys at all temperatures.

Grain size is well known to affect creep resistance in superalloys (Refs. 1 and 2). Grain size effects in this study are evident in the creep curves in Figure 12. At 760 and 815 °C, creep properties were significantly improved with increasing grain size since grain boundary sliding likely becomes an operative deformation mechanism. However, at the lower temperature of 704 °C, grain size effects were alloy dependent. For example, finer grained Mar-M247LC showed greater creep resistance at 704 °C, whereas a smaller grain size in Rene´ 80 provided slightly improved creep properties at 704 °C. In contrast, LSHR with different grain sizes had fairly comparable creep resistances at this low temperature, although 50 μm LSHR exhibited a slightly higher life compared to the 15 μm LSHR at 704 °C. LSHR with 0.03 wt% C and 50 μm had a markedly inferior creep resistance at 704 °C in comparison to the 0.05 wt% C alloy with the same grain size.

The ranking of these alloys as a function of testing temperature is best seen by the Larson-Miller Parameter plots shown in Figure 13(a) and (b) for time to 0.2 percent creep strain and rupture life, respectively. Additionally, creep rupture elongation and creep rupture reduction in area are displayed in Figure 13(c) and (d), respectively, and most alloys display sufficient rupture ductility between 704 to 815 °C. Reduction in area and elongation of Mar-M247LC at grain sizes of both 60 and 1200 μm was lowest of the tested alloys, and could be marginal for some applications. Larson-Miller Parameter plots typically display applied stress versus the Larson-Miller Parameter (LMP) which is defined in the following equation (Ref. 30):

$$LMP = (T + 273.15)(20 + \log t)/1000$$

where T is temperature in °C and t is time in hours. This parameter has a direct dependence on temperature and a weaker logarithmic dependence on time. At a given applied stress level, data to the right in the LMP plot represent higher creep resistance with either longer time at the same temperature, or higher temperature for the same time. Simple linear regression equations are included on the plot for estimating creep response in this intermediate temperature regime only. However, it is not advisable to use these equations to estimate creep response outside this regime because the shape of the LMP curve is not linear at higher temperatures and lower applied stresses. Resulting LPM curves presented in Figure 13(a) and (b) confirm the consistently higher rupture life for LDS-1101+Hf at all tested conditions, as well as the alloy responses described earlier. Although this single crystal LDS alloy and its heat treatment were designed for application as coated turbine blades at temperatures near 982 to 1100 °C (Refs. 21 and 22), LDS-1101+Hf showed excellent creep response between 760 to 815 °C in the present study. Additional creep tests and analyses are necessary to fully estimate variability under these testing conditions, but this screening evaluation of creep properties indicates significant potential for LDS-1101+Hf as a hybrid disk rim to withstand creep deformation at rim temperatures from 760 °C to at least 815 °C. PM disk superalloys such as LSHR would not be capable of withstanding a disk rim application at temperatures between 760 to 815 °C, since this alloy was designed for service to temperatures near 700 °C.

Creep resistance is shown versus grain size of the polycrystalline superalloys in Figure 14. Both LSHR and Mar-M247LC had increasing creep life with increasing grain size for tests near 815 °C. However, this was not the case in tests at 704 °C, with life actually decreasing for increasing grain size in Mar-M247LC. This may represent a change in deformation mechanisms with decreasing temperature.

Creep rupture failure modes are compared in Figures 15 and 16. The polycrystalline creep specimens failed from surface-initiated intergranular cracks at all test temperatures, with typical fractures shown. Fracture surfaces of polycrystalline materials were similar at all test temperatures from 704 to 815 °C. Single crystal LDS initiated multiple cracks around the circumference of the gage length near the fracture surface, as seen in the failed specimen at 815 °C in Figure 16(h).

To further examine the cracking characteristics in failed creep specimens, longitudinal sections of creep rupture specimens of selected alloys were metallographically polished through the center of the specimen gage and examined by optical microscopy in the unetched condition. Both grain sizes of LSHR and single crystal LDS-1101+Hf were selected for comparison. The initiation of cracks along the specimen surface is shown in Figures 17 and 18 for 15 and 50 μm, respectively, grain size LSHR after creep rupture at 704 °C. These images confirm that multiple secondary cracks initiated at the specimen surface of both grain sizes of LSHR and progressed inward during 704 °C creep, although the pore in Figure 17(b) also initiated fine cracks. It is interesting to note that the LSHR specimen with the larger, 50 μm grain size exhibited fewer surface cracks at 704 °C (Fig. 18), likely due to the fewer number of grain boundaries intersecting the specimen surface. This may help to explain the slightly improved creep life at this temperature for the 50 μm LSHR material. The longitudinal sections through the fracture surfaces of the LSHR material in Figure 19(a) and (b) also indicate the effects of grain size differences. The 15 μm, fine grained material in Figure 19(a) predominantly produced a more planar fracture surface as the primary crack progressed across the gage diameter until the final ligament failed on the right side, whereas the 50 μm grain material in Figure 19(b) produced a more ragged fracture due to cracks following the grain boundaries along its larger grain size.

A polished, longitudinal section near the fracture surface of single crystal LDS-1101+Hf is shown for comparison in Figure 20 after a lengthy creep rupture life of 2680.9 h at 704 °C and 793 MPa. Several secondary cracks initiated at the specimen surface along with cracks that initiated from internal porosity. Cracking was only observed in the vicinity of the fracture surface and was not seen well away from the fracture in the uniform gage section. Figure 19(c) shows that the central portion of the fracture surface was perpendicular to the loading axis, while the outer regions appear to have fractured along crystallographic directions. Some secondary cracking may be seen at internal pores that were aligned along the growth direction of the single crystal material. The creep specimens of LDS-1101+Hf at 704 °C had significant ductility with elongations of 20 to 22 percent and reductions in area of 31 to 34 percent, Table 4 and Figure 13(c) and (d).

The appearance and density of cracking after creep rupture at 815 °C and 448 MPa was significantly different in LSHR, as compared to that observed at the lower testing temperature. Figures 21 and 22 show the initiation of both surface and internal cracks in the 15 and 50 μm LSHR materials, respectively, after creep rupture at 815 °C. As seen in Figure 21, the secondary surface cracks in the 15 μm material were observed to extend to depths of ~50 μm, and internal cracks were quite numerous, but typically much shorter in length than the observed surface cracks. It is readily apparent that many more cracks were initiated along the grain boundaries in the 15 μm LSHR at 815 °C than at 704 °C. Figure 22 clearly demonstrates the longer secondary cracks along the grain boundaries in the 50 μm LSHR at 815 °C, compared to that in 15 μm LSHR. Despite these longer secondary cracks in the failed specimens of the larger grained material, 50 μm LSHR had a low density of crack initiation sites and exhibited nearly double the creep rupture life of the 15 μm LSHR at 815 °C. Grain boundary sliding mechanisms are expected to become operative at higher testing temperatures, thus favoring larger grained material over finer grained material. Additionally, the longer-lived material had more time to initiate these secondary cracks. These above mentioned characteristics of secondary cracking were also evident in sections taken directly through the fracture surfaces, as seen in Figure 23(a) and (b).

The cracking observed in single crystal LDS-1101+Hf at 815 °C appeared similar to that at 704 °C in that both surface cracks and cracks at internal pores were observed, as seen by comparison of Figures 24 and 20, respectively. The main difference appeared to be that at 815 °C secondary cracking was seen away from the fracture surface as well as in vicinity of the fracture surface. Figure 23(c) shows the necked region behind the fracture surface. Again secondary cracking is seen at the surface as well as at internal pores that are aligned along the growth direction of the single crystal. Part of the specimen appears to have fractured along crystallographic directions. The creep specimens of LDS-1101+Hf at 815 °C exhibited significant overall ductility with elongations of 34 to 38 percent and reductions in area of 39 to 40 percent, Table 4 and Figure 13(c) and (d).

Notch Fatigue

The materials were initially subjected to notch dwell fatigue tests, with 90 s dwells applied at minimum stress. One additional low density single crystal blade alloy, LDS-1101 having no Hf (Table 1), was also tested (Refs. 21 and 22). Notch dwell fatigue test lives are compared in Table 5 and Figure 25. At 704 °C, the materials had comparable fatigue lives, with no significant differences identified either with respect to grain size or alloy in these limited tests. However, the combined LDS alloys had higher mean fatigue lives than those of LSHR, Mar-M247LC, and Rene´ 80 at 815 °C, at a statistical significance of over 99 percent.

Notch fatigue life in tests with dwells at minimum applied stress is shown versus grain size of LSHR in Figure 26. No significant relationship between fatigue life and grain size was present in tests at 704 °C. LSHR had increasing fatigue life with increasing grain size for tests at 815 °C, which was also consistent with the creep response at 815 °C.

The associated notch fatigue failure modes for tests with dwells at minimum stress are compared in Figures 27 and 28. Transgranular cracks initiated failure at ten or more locations along the oxidized surface of the notch for each material at both 704 and 815 °C. Additional cracks were also observed on the sides of notches, adjacent to major cracks on the fracture surface. LSHR with both 15 and 50 μm grain sizes had no evidence of grain boundary failure initiations, and quite comparable failure modes. This failure mode has been observed on other notch fatigue evaluations of fine and coarse grain powder metal disk superalloys including LSHR (Ref. 24), ME3 (Ref. 25), and RR1000 (Ref. 23) for cycles with dwells at minimum applied stress at temperatures near 704 °C. Similar failures also occurred here for Mar-M247LC and Rene´ 80. The surface cracks in LDS specimens did not appear to be very flat and crystallographic, but remained roughly normal to the loading axis. These surface cracks did not appear to have preferred secondary crystallographic orientations of initiation and growth, with respect to the specimen's crystallographic orientation. Instead, cracks were evenly distributed along the 360° circumference of the specimen.

This dwell cycle had been selected for testing because minimal stress relaxation was predicted to occur in the notch during the dwells near zero stress (Ref. 25). This allowed evaluation of time-dependent environmental effects on a material's fatigue resistance at comparable notch stresses to that for tests with no dwells. In order to quantify the effect of this dwell, several fatigue tests of the LDS alloys and LSHR notched specimens were performed at 815 °C using the same applied stresses, but without the dwell of 90 s at minimum load. Resulting lives are compared in Table 5 and Figure 29. Mean lives were improved over 20x for both alloys by removing the 90 s dwell at minimum stress. Still, LDS alloys again had higher mean life than that of LSHR at 815 °C.

Failure modes in cyclic tests with no dwells are compared in Figure 30. Cracks initiated in LSHR at grain boundaries connected to the surface. They quickly transitioned to predominantly transgranular crack growth, after traversing the surface-connected grains. However, with further crack growth to depths of 100 to 200 μm, the cracks eventually transitioned back to predominantly intergranular cracking. LDS alloys again had surface cracking that did not appear to be crystallographic, but remained near normal to the loading axis.

One possible reason for the higher relative lives of LDS alloys in these notch fatigue tests could be associated with the concentration of stresses in the notch of these single crystal superalloys. The stresses generated in the specimen's notch would be influenced by the anisotropic elastic and inelastic properties of the LDS alloys, and could differ significantly from those generated in the polycrystalline superalloys. Tensile tests produced lower relative plasticity for LDS-1101+Hf than for the polycrystalline superalloys at 1 percent total strain for each test temperature, and such differences due to the anisotropic elastic properties of single crystals oriented parallel to the [001] axial loading direction could produce lower plastic strains and effective axial stresses in notch fatigue tests without dwells and with dwells at minimum applied stress. However, the multiaxial stresses generated at notches would be influenced by elastic and plastic properties in other crystallographic directions beyond the LDS specimens' [001] axial loading direction. Elastic-visco-plastic modeling using single crystal and polycrystal elastic properties along with the measured tensile and creep properties would be needed to estimate relative stress states in these notches for different fatigue cycles. An additional reason for the higher LDS lives could be related to potentially better oxidation resistance and elimination of surface grain boundaries susceptible to cracking.

Notch fatigue tests with dwells at maximum stress have been shown to encourage stress relaxation in the notch, so that with continued cycling, materials which allow more stress relaxation can have lower stabilized peak stresses in the notch to improve fatigue life. The monotonic stress relaxation tests had indicated LSHR allowed significantly more stress relaxation than LDS, Figure 5(c). Therefore, several additional fatigue tests of LDS and LSHR notched specimens were also performed at 815 °C using the same applied stresses, but with the dwell of 90 s at maximum load in order to screen this effect. Resulting lives are also compared in Table 5 and Figure 29. Again, LDS had significantly higher mean life than that of LSHR, in spite of the greater resistance of LDS to stress relaxation previously observed in tensile tests. This indicated that time-dependent stress relaxation in the notch could not perturb the life differences for the two materials here, and could not account for the differences.

Failure modes in notch fatigue tests with dwells at maximum stress are compared in Figure 31. Intergranular cracks were initiated at the environment-affected surface of LSHR specimens. These cracks continued to grow along grain boundaries. But this process appeared to be eventually superceded by rupture overload of the remaining interior, with a different morphology. LDS specimen failures initiated at the oxidized superalloy surface layers and sometimes at surface-connected MC carbides or pores. The cracks did not appear to be overly flat or crystallographic, but again gently undulated.

In summary, the improved life of LDS over LSHR in notched gage fatigue is likely related to different stabilized effective stress states in the single crystal notched specimens, better inherent environmental resistance, and the lack of grain boundaries, since grain boundaries can enable accelerated environment-assisted intergranular cracking. Further analyses are necessary to fully understand and rank these effects.

Uniform Gage Fatigue

Based on their favorable results in tensile, creep, and notch fatigue tests, LSHR and LDS materials were selected for uniform gage fatigue tests at 704 to 815 °C, and these results are summarized in Table 6. Two other low density single crystal blade alloys, LDS-1101 and LDS-4583, were also tested to assess the effects of varied compositions (Refs. 21 and 22). Typical stress-strain hysteresis loops after stabilization of cyclic stresses are compared in Figure 32 for tests at 704 and 815 °C. Similar to the previously presented tensile stress-strain curves, tests at a fixed total strain range produced significantly less plastic strain range in lower modulus LDS alloys than for LSHR. Fatigue lives are compared versus total strain range and plastic strain range in Figure 33. Based on their lower elastic modulus, the LDS alloys clearly had superior fatigue life to LSHR as a function of total strain range in all test conditions. When lives are compared versus the plastic strain range generated in each test, the ranking is reversed, with fine grain LSHR having higher lives. However, there is substantial scatter in this limited screening data, and further testing would be needed for correlations to generate predictive relationships.

The stabilized stresses did vary between LDS and LSHR materials, as indicated in Figure 32. The elastic stress range could be approximated using (Ref. 31) an alternating pseudo-stress ($\Delta\sigma_{pseudo}$), defined as:

$$\Delta\sigma_{pseudo} = \Delta\varepsilon_t/E$$

where $\Delta\varepsilon_t$ is the total strain range, and E is the axial elastic modulus. Both maximum stress (σ_{max}) and stress range ($\Delta\sigma$) differences could be accounted for using a Smith-Watson-Topper stress parameter (Ref. 32):

$$\sigma_{SWT} = (\sigma_{max}\,\Delta\sigma / 2)^{0.5}$$

Fatigue life is compared using these stress parameters in Figure 34. On this basis, the ranking was dependent on temperature. At 704 °C, 15 μm LSHR had highest life, followed by 50 μm LSHR, and then the LDS alloys grouped together. At 815 °C, lives were comparable for LSHR and LDS.

Failure initiation modes for these uniform gage fatigue tests are compared in Figures 35 and 36. The 15 and 50 μm LSHR specimens tested at 704 and 760 °C typically failed from internal cracks initiating at nonmetallic Type 2 (Ref. 31) granulated inclusions. Qualitative energy dispersive X-ray analyses in the SEM indicated they were rich in aluminum and oxygen, and assumed to be representative of Al_2O_3. However, failures at 815 °C initiated at the surface, from environment-effected surface layers. LDS-1101+Hf, 1101, and 4583 specimens all failed from cracks initiating at casting pores, which were 42 to 115 μm long and 19 to 58 μm wide.

The stabilized hysteresis loops generated in these fatigue tests of uniform gage specimens suggest that lower stresses could be generated in LDS than LSHR at disk features, such as holes and corners, surrounded and thereby constrained by bulk material. This could also be the case in the notched gage specimen tests performed here. Elastic-viscoplastic finite element modeling of the notched gage specimen would be necessary to estimate relative differences in stresses for the different materials and test conditions. Beyond these aspects, the consistent failures at pores for LDS alloys suggest pore content and size should be controlled through process modifications, to potentially improve LDS alloy fatigue resistance.

Environmental Resistance

The oxide scale thickness and γ' phase depletion depths of LDS specimens often appeared to be significantly smaller than that for LSHR on the fracture surfaces of tested specimens. This was apparent in spite of the fact that the LDS creep and notch dwell fatigue tests lasted longer total times at the highest test temperature of 815 °C. However, the depth of environmental attack was not always visible on fracture surfaces, as crack faces were also oxidized during testing.

Oxidation attack of LDS and LSHR was briefly screened after equivalent static exposures of unstressed coupons at 815 °C for 440 h. Images from metallographically-prepared cross sections of these specimens are compared in Figure 37. LDS-1101+Hf had significantly thinner oxide layers and γ'-depleted zone than for LSHR. This indicated that LDS-1101+Hf had improved oxidation resistance over the LSHR materials in these conditions. That could help explain the higher elongations and reductions in area observed in tensile and creep tests of LDS over that of LSHR at 815 °C, and the much higher life of LDS over that of LSHR in notch dwell tests at 815 °C. However, additional evaluations would be necessary to quantify the effects of environment for each mechanical test regime.

Selection of Hybrid Disk Materials

Results of monotonic tensile and creep tests were compared together in Figures 38 and 39 by considering yield strength, ultimate strength, time to 0.2 percent creep, and time to rupture for all tested materials. Excessive plasticity or creep in the bore and web of a hybrid disk reaching up to 704 °C would be unacceptable, due to their large effective radius and the tight clearances necessary for efficient

operation of a turbine stage. Figure 38 with 0.1 percent yield strength versus time to 0.2 percent creep indicated 15 μm LSHR and LDS provided the best combinations of properties at 704 °C for the present test conditions, while LDS was superior at 815 °C. More plasticity and creep could be allowable in the rim section of a hybrid disk for some cases, which would approach the goal temperature of 815 °C. However, failure would still be unacceptable. Figure 39 with ultimate strength versus time to creep rupture indicated single crystal LDS provided the best combination of failure properties, with about 10x higher creep rupture life and superior ultimate strength at 815 °C. Therefore, monotonic property comparisons suggested 15 μm LSHR for the bore and web, and LDS for the rim of a hybrid disk.

The choice of LDS for the rim was strongly reinforced by its 8x to 10x higher notch fatigue life over all other materials at 815 °C, for cycles with or without dwells. Figure 40 displays dwell versus no dwell notch fatigue life at 815 °C, and shows the clear advantage of LDS in these test conditions. For equivalent applied total strains in tests of uniform gage specimens, LDS also had superior fatigue life over LSHR at 704 to 815 °C. However, fatigue tests of uniform gage specimens indicated 15 μm LSHR would give longer fatigue life than LDS at equivalent applied alternating pseudo-stress and Smith-Watson-Topper stress for temperatures of 704 and 760 °C. But lives at 815 °C were comparable on the Smith-Watson-Topper basis, which considers stress range as well as maximum applied stress. Therefore, LSHR with a grain size of 15 μm was confirmed worthy of further study as the bore/web, and LDS-1101+Hf was confirmed for the rim of a hybrid disk, based on tensile, creep, and fatigue crack initiation properties.

Recommended Future Work

1. Hybrid disk design trade studies are now necessary, to assess the potential benefits of a hybrid disk to engine performance and efficiency for different advanced engines and associated disk configurations. These studies can point out the design-limiting mechanical properties, most favorable configurations, material transition location, and associated application temperature profiles in preliminary designs of hybrid disks.
2. Elastic-viscoplastic modeling is necessary to compare the effective stresses generated by continued fatigue and dwell fatigue cycling of notched LDS and LSHR specimens. This could be used to understand current results and guide further testing of notched specimens.
3. LDS-1101+Hf processing refinement trials are necessary, to attempt reducing the size and number of pores. This can be used to determine the effects of reduced porosity on its cyclic fatigue resistance in uniform gage fatigue tests.
4. Dwell fatigue crack growth, cyclic crack growth, additional tensile, creep, and low cycle fatigue tests are necessary, including additional temperatures and stresses, to support the design trade studies and allow preliminary design of prototype hybrid disk configurations.
5. Joining trials are required to begin screening joining processes versus potential joint configuration, microstructure, and mechanical properties. The joining process could influence processing of each material, both before and after the joining operation.
6. The processing-microstructure-mechanical property relationships relevant for a hybrid disk need to be understood. This requires optimization of the joining process as well as heat treatments, in order to optimize tensile strength, creep, and fatigue properties for hybrid disk applications.

Summary and Conclusions

The mechanical properties of several cast blade superalloys and one powder metallurgy disk superalloy, each with varied grain sizes, were assessed for a hybrid material disk concept of joined dissimilar bore and web materials. Tensile stress relaxation, creep, uniform gage, and notch fatigue tests were performed at 704 to 815 °C. These properties were compared and related to the microstructures and failure modes observed. It was concluded that:

1. Mechanical properties can vary substantially among these cast and powder metal superalloys and associated grain sizes, such that different alloys are clearly preferable at different temperatures.
2. LSHR with a fine grain size of 15 μm appears preferable for temperatures up to 704 °C. Conversely, single crystal (grain) LDS is preferable at temperatures approaching 815 °C, based on tensile, creep, and fatigue crack initiation properties.
3. Therefore, LSHR with a grain size of 15 μm was confirmed worthy of further study as the bore/web, and LDS-1101+Hf was confirmed for the rim of a hybrid disk.
4. Design trade studies, modeling, material processing refinements, and additional mechanical testing are necessary to now develop and demonstrate this concept.

References

1. C.S. Sims, N.S. Stoloff, W.C. Hagel, ed. Superalloys II, John Wiley and Sons, New York, NY, 1987.
2. R.C. Reed, The Superalloys, Cambridge University Press, Cambridge, U.K., 2006.
3. D.P. Mourer, J.L. Williams, "Dual Heat Treat Process Development for Advanced Disk Applications," Superalloys 2004: Proceedings of the 10th International Symposium on Superalloys, ed. K.A. Green, T.M. Pollock, H. Harada, T.E. Howson, R.C. Reed, J.J. Schirra, S. Walston, The Minerals, Metals, & Materials Society, Warrendale, PA, 2004, pp. 401-407.
4. H. Merrick, R.C. Benn, P.R. Bhowal, "High Strength Powder Metallurgy Nickel Base Alloy," U.S. Patent 6,468,368, U.S. Patent and Trademark Office, Washington, D.C., 2002.
5. A.F. Hieber, H.F. Merrick, "High Temperature Powder Metallurgy Superalloy With Enhanced Fatigue and Creep Resistance," U.S. Patent 6,866,727, U.S. Patent and Trademark Office, Washington, D.C., 2005.
6. J. Gayda, T.P. Gabb, P.T. Kantzos, "The Effect of Dual Microstructure Heat Treatment on an Advanced Nickel-Base Superalloy," Superalloys 2004: Proceedings of the 10th International Symposium on Superalloys, ed. K.A. Green, T.M. Pollock, H. Harada, T.E. Howson, R.C. Reed, J.J. Schirra, S. Walston, The Minerals, Metals, & Materials Society, Warrendale, PA, 2004, pp. 323-329.
7. C. Duquenne, J.C. H. Lautridou, M. Marty, M. Soucail, A. Walder, "Nickel-based Superalloys With High Temperature Stability," U.S. Patent 5,815,792, U.S. Patent and Trademark Office, Washington, D.C., 1998.
8. D.P. Mourer, E.S. Huron, K.R. Bain, E.E. Montero, P.L. Reynolds, J.J. Schirra, "Superalloy Optimized for High-temperature Performance in High-Pressure Turbine Disks," U.S. Patent 6,521,175, U.S. Patent and Trademark Office, Washington, D.C., 2003.
9. P.L. Reynolds, "Superalloy Compositions, Articles, and Methods of Manufacture," U.S. Patent 8,147,749, U.S. Patent and Trademark Office, Washington, D.C., 2012.
10. D.A. Woodford, "Gas Phase Embrittlement and Time Dependent Cracking of Nickel Based Superalloys," Energy Materials, V. 1, No. 1, 2006, pp. 59-79.
11. T.P. Gabb, J. Telesman, P.T. Kantzos, A. Garg, "Effects of Temperature on Failure Modes for a Nickel-Base Disk Superalloy," J. Failure Analysis and Prevention, V. 7, Feb. 2007, pp. 56-65.
12. A. Encinas-Oropesa, G.L. Drew, M.C. Hardy. A.J. Leggett, J.R. Nicholls, N.J. Simms, "Effects of Oxidation and Hot Corrosion in a Nickel Disc Alloy," Superalloys 2008: Proceedings of the 11th International Symposium on Superalloys, ed. R.C. Reed, K.A. Green, P. Caron, T.P. Gabb, M.G. Fahrmann, E.S. Huron, S.A. Woodard, TMS, Warrendale, PA, 2008, pp. 609-618.
13. C. Sudbrack, S. Draper, T. Gorman, J. Telesman, T. Gabb, D. Hull, "Oxidation and the Effects of High Temperature Exposures on Notched Fatigue Life of an Advanced Powder Metallurgy Disk Superalloy," Superalloys 2012: 12th International Symposium on Superalloys, ed. E.S. Huron, R.C. Reed, M.C. Hardy, M.J. Mills, R.E. Montero, P.D. Portella, J. Telesman, TMS, Warrendale, PA, 2012, pp. 863-872.

14. H.-J. Jou, P. Voorhees, G.B. Olson, "Computer Simulations for the Prediction of Microstructure/ Property Variation in Aeroturbine Disks," Superalloys 2004: Proceedings of the 10th International Symposium on Superalloys, ed. K.A. Green, T.M. Pollock, H. Harada, T.E. Howson, R.C. Reed, J.J. Schirra, S. Walston, The Minerals, Metals, & Materials Society, Warrendale, PA, pp. 877-886.
15. G.F. Mathey, "Method of Making Superalloy Turbine Disks Having Graded Coarse and Fine Grains," U.S. Patent 5,312,497, U.S. Patent and Trademark Office, Washington, D.C., May, 1994.
16. R.J. Mitchell, J.A. Lemsky, R. Ramanathan, H.Y. Li, K.M. Perkins, L.D. Connor, "Process Development & Microstructure & Mechanical Property Evaluation of a Dual Microstructure Heat Treated Advanced Nickel Disc Alloy," Superalloys 2008: Proceedings of the 11th International Symposium on Superalloys, ed. R.C. Reed, K.A. Green, P. Caron, T.P. Gabb, M.G. Fahrmann, E.S. Huron, S.A. Woodard, TMS, Warrendale, PA, 2008, pp. 347-356.
17. D.P. Mourer, E. Raymond, S. Ganesh, J. Hyzak, Dual Alloy Disk Development, Superalloys 1996: Proceedings of the 8th International Symposium on Superalls, ed. R.D. Kissinger, D.J. Deye, D.L. Anton, A.D. Cetel, M.V. Nathal, T.M. Pollock, D.A. Woodford, TMS, 1996, pp. 637-643.
18. W.C. Baker, T.E. Strangman, D.A. Rice, J.S. Perron, C. Zollars, U.S. Patent 7,832,986, U.S. Patent and Trademark Office, Washington, D.C., 2010.
19. D.D. Dierksmeier, T.M. Heffernan, High Temperature Rotor Blade Attachment, U.S. Patent 5688108 A, U.S. Patent Office, Nov. 18, 1997.
20. T.P. Gabb, J. Gayda, J. Falsey, "Forging of Advanced Disk Alloy LSHR", NASA/TM—2005-213649, Washington, D.C., June, 2005.
21. R.A. MacKay, T.P. Gabb, J.L. Smialek, M.V. Nathal, "A New Approach of Designing Superalloys for Low Density," Journal of Metals, V. 62, No. 1, 2010, pp. 48-54.
22. R.A. MacKay, T.P. Gabb, A. Garg, R.B. Rogers, M.V. Nathal, "Influence of Composition on Microstructural Parameters of Single Crystal Nickel-base Superalloys," Materials Characterization, V. 70, 2012, pp. 83-100.
23. M.R. Bache, J.P. Jones, G.L. Drew, M.C. Hardy, N. Fox, "Environment and Time Dependent Effects on the Fatigue Response of an Advanced Nickel Base Superalloy," Int. J. Fatigue, V. 31, 2009, pp. 1719-1723.
24. T.P. Gabb, J. Telesman, L. Ghosn, A. Garg, J. Gayda, "Factors Influencing Dwell Fatigue Cracking in Notches of Powder Metallurgy Superalloys," NASA/TM—2011-217118, Washington, DC, June 2011.
25. J. Telesman, T. Gabb, Y. Yamada, L. Ghosn, D. Hornbach, N. Jayaraman, "Dwell Notch Low Cycle Fatigue Behavior of a Powder Metallurgy Nickel Disk Alloy," Superalloys 2012: Proceedings of the 12th International Symposium on Superalloys, ed. E.S. Huron, R.C. Reed, M.C. Hardy, M.J. Mills, R.E. Montero, P.D. Portella, J. Telesman, TMS, Warrendale, PA, 2012, pp. 853-862.
26. T.P. Gabb, J. Gayda, J. Telesman, P.T. Kantzos, "Thermal and Mechanical Property Characterization of the Advanced Disk Alloy LSHR," NASA/TM—2005-213645, Washington, D.C., June, 2005.
27. T.P. Gabb, J. Gayda, "Tensile and Creep Property Characterization of Potential Brayton Cycle Impeller and Duct Materials," NASA/TM—2006-214110, Washington, D.C., Feb. 2006.
28. J. Safari, S. Nategh, "On the Heat Treatment of Rene 80 Nickel-Base Superalloy," J. Mat. Proc. Tech., V. 176, 2006, pp. 240-250.
29. H-E Huang and C-H Koo, "Characteristics and Mechanical Properties of Polycrystalline CM247LC Superalloy Castings," Mater. Trans. A, Vol. 45, No. 2, 2004, pp. 562-568.
30. F.R. Larson, J. Miller, "A Time-Temperature Relationship for Rupture and Creep Stresses," Trans. ASME, vol. 74, 1952, pp. 765-766.
31. C.E. Shamblen, D.R. Chang, "Effect of Inclusions on LCF Life of HIP Plus Heat Treated Powder Metal Rene′ 95," Met. Trans B., V. 16, No. 4, 1985, pp. 775-784.
32. K.N. Smith, P. Watson, T.H. Topper, "A Stress-strain Function for the Fatigue of Metals," Journal of Metals, V. 5, 1970, pp. 767-778.

TABLE 1.—ALLOY COMPOSITIONS IN WEIGHT PERCENT, MEASURED BY INDUCTIVELY COUPLED PLASMA-OPTICAL EMISSION SPECTROMETER AT SUPPLIER (S) OR NASA GRC (n)

Alloy – weight percent	Al	B	C	Co	Cr	Fe	Hf	Mn	Mo	Ni	Nb	O	Re	Si	S	Ta	Ti	V	W	Y	Zr
LSHR (s)	3.54	0.027	0.045	20.4	12.3	0.1	0.0	0.0	2.71	Bal.	1.49	0.02		0.012	<.0010	1.52	3.45	0.006	4.28	<.0005	0.049
LSHR 0.03C (s)	3.46	0.028	0.029	20.7	12.52	0.070	0.0	<.01	2.73	Bal.	1.45			0.0300	<0.001	1.60	3.500		4.33		0.0490
Rene´ 80 (s)	3.06	0.015	0.16	9.41	13.92	0.04	<.01	<.01	4.03	Bal.	0.01	0.0006		0.04	<.0010	<.01	4.98	<.01	3.97	0.0003	0.03
Mar-M247LC (s)	5.63	0.014	0.075	9.28	8.31	0.05	1.48	<.01	0.50	Bal.	<.01	0.0005	0.01	0.02	<.0010	3.19	0.77	<.01	9.48	0.0001	0.01
LDS-1101 +Hf (n)	6.10		0.024	10.0	5.00	0.013	0.19		7.30	Bal.		0.0017	3.10	0.11	<.0001	6.50				0.0078	0.004
LDS-1101 (n)	6.00	0.004	0.016	9.90	4.70	0.02	0.00		7.10	Bal.		0.0021	3.00	0.04	<.0004	6.20	0.0009			0.0050	0.008
LDS-4583 (n)	6.00	0.003	0.0104	5.00	3.90	0.03	0.20		8.10	Bal.		0.0013	3.00	0.015	<.0003	6.30	0.0005			0.0057	0.003

TABLE 2.—GRAIN AND γ´ PRECIPITATE SIZES

		Secondary γ‘							Tertiary γ'						
Alloy	Grain Size - μm	Count -n	Median γ' Area - μm²	Mean γ' Area - μm²	Standard Deviation - μm²	Median γ' Equiv. Radius - μm	Mean γ' Equiv. Radius - μm	Standard Deviation -μm	Count - n	Median γ' Area -nm²	Mean γ' Area - nm²	Standard Deviation -nm²	Median γ' Equiv. Radius -nm	Mean γ' equiv. radius - nm	Standard Deviation - nm
LSHR	15	204	0.051	0.051	0.024	0.128	0.124	0.031	119	678	761	423	14.7	15.1	4.0
LSHR	50	203	0.059	0.060	0.030	0.138	0.134	0.036	113	845	1092	945	16.4	17.3	6.9
LSHR 0.03C	50	200	0.041	0.044	0.024	0.115	0.112	0.035	114	601	677	376	13.8	14.2	3.8
Rene´ 80	200	200	0.127	0.143	0.083	0.201	0.204	0.061	139	740	927	732	15.3	16.2	5.7
Rene´ 80	600	201	0.110	0.125	0.088	0.187	0.187	0.069	138	749	943	717	15.4	16.3	5.9
Mar-M247LC	60	201	0.185	0.825	1.574	0.242	0.388	0.335	149	1529	2319	2103	22.1	24.6	11.6
Mar-M247LC	1200	202	0.149	0.408	0.563	0.218	0.300	0.201	140	1360	2461	2682	20.8	24.0	14.4
LDS1101+Hf		202	0.103	0.118	0.066	0.181	0.187	0.052							

TABLE 3.—TENSILE TEST RESULTS

Material	Specimen	Temperature - ° C	0.1 % Yield Strength - MPa	0 h Relaxed Stress -MPa	1 h Relaxed Stress -MPa	10 h Relaxed Stress -MPa	100 h Relaxed Stress -MPa	Ultimate Tensile Strength - MPa	Elongation - %	Reduction in Area -%	Specimen Degrees off [001]
LSHR-15 µm	P3-T2	704	999	1073	817	736	629	1341	22.9	31.6	
LSHR-15 µm	P3-T3	704	993	1063	786	700	591	1302	24.1	31.1	
LSHR-15 µm	P3-18-1	760	969	1003	605	495	369	1151	16.1	22.5	
LSHR-15 µm	P3-18-2	760	967	1009	616	520	380	1161	18.9	26.0	
LSHR-15 µm	P3-T1	815	885	842	443	325	221	956	16.4	23.6	
LSHR-15 µm	P3-T4	815	887	841	446	336	228	941	20.1	29.5	
LSHR-50 µm	T4-T2	704	968	1039	787	716	601	1298	20.7	27.5	
LSHR-50 µm	T4-T4	760	960	1025	658	565	438	1260	17.8	21.3	
LSHR-50 µm	T4-T1	815	887	857	474	366	275	967	19.6	27.8	
LSHR(0.03C)-50 µm	DRO3-T3	704	978	1051	841	761	648	1343	15.6	22.3	
LSHR(0.03C)-50 µm	DRO3-T4	760	956	1025	663	562	430	1150	18.0	25.6	
LSHR(0.03C)-50 µm	DRO3-T1	815	894	864	480	372	288	981	14.7	20.2	
Rene´ 80-200 µm	RMX3-T3	704	661	718	636	610	541	1118	6.0	8.4	
Rene´ 80-200 µm	RMX3-T4	760	683	761	578	515	415	1094	11.1	11.0	
Rene´ 80-200 µm	RMX3-T2	815	652	732	434	373	302	906	14.3	22.8	
Rene´ 80-600 µm	RE2-T3	704	669	728	636	593	518	1123	9.9	10.8	
Rene´ 80-600 µm	RE2-T4	760	685	756	587	538	440	1076	12.8	21.8	
Rene´ 80-600 µm	RE2-T2	815	638	763	484	423	351	932	16.3	37.3	
MM247LC-60 µm	MMX12-T3	704	774	846	768	733	675	1102	8.8	13.3	
MM247LC-60 µm	MMX18-T1	704	790	867	740	681	609	1115	9.9	15.7	
MM247LC-60 µm	MMX18-T3	760	800	897	677	639	515	1070	8.0	15.4	
MM247LC-60 µm	MMX12-T2	815	745	844	553	440	277	949	7.8	12.2	
MM247LC-60 µm	MMX12-T4	815	774	858	568	476	309	952	5.9	11.3	
MM247LC-1200 µm	MME4-T3	704	738	789	731	672	636	1061	7.7	17.6	
MM247LC-1200 µm	MME4-5T	704	740	793	714	663	610	1045	6.5	9.0	
MM247LC-1200 µm	MME4-7T	760	719	784	646	601	516	1030	6.6	13.9	
MM247LC-1200 µm	MME4-T2	815	804	894	622	511	349	993	5.8	12.1	
MM247LC-1200 µm	MME4-T4	815	783	869	599	492	334	981	4.9	5.2	
LDS1101+Hf	7M-2T	704	874	880	875	772	658	1236	6.4	11.8	0.3
LDS1101+Hf	7M-3T	704	860	869	841	750	657	1293	6.9	8.9	0.3
LDS1101+Hf	7M-1T	760	887	884	687	640	593	1260	12.3	14.4	0.3
LDS1101+Hf	7M-6T	760	872	875	695	642	599	1243	10.2	20.4	0.3
LDS1101+Hf	7M-4T	815	976	957	629	549	466	1225	26.0	30.4	0.3
LDS1101+Hf	7M-5T	815	884	888	615	572	498	1207	24.6	22.3	0.3

TABLE 4.—CREEP TEST RESULTS

Material–Grain Size	Specimen	Temperature °C	Stress -MPa	Minimum Creep Rate - s^{-1}	0.1 % creep life - h	0.2 % creep life - h	1 % creep life - h	2 % creep lif e- h	Rupture Life - h	Elongatio n - %	Reduction in Area - %	Specimen Degrees off [001]
LSHR-15 µm	P3-C1	704	793	2.14E-08	10.8	24.0	83.9	132.7	351.6	10.3	12.0	
LSHR-15 µm	P3-C3	704	793	1.94E-08	11.9	26.2	87.5	140.0	383.2	12.0	17.7	
LSHR-15 µm	P3-18-3	760	621	2.58E-08	8.5	13.5	35.7	53.6	116.6	15.7	16.7	
LSHR-15 µm	P3-C2	815	448	4.83E-08	3.6	9.1	31.8	45.7	77.5	11.5	18.5	
LSHR-15 µm	P3-C4	815	448	5.15E-08	4.9	10.0	31.0	44.5	78.0	15.0	16.8	
LSHR-50 µm	T4-C3	704	793	2.29E-08	8.9	18.8	92.9	150.6	404.2	9.7	14.2	
LSHR-50 µm	T4-C1	760	621	3.01E-08	3.1	11.7	53.2	88.1	214.0	13.3	16.1	
LSHR-50 µm	T4-C2	815	448	1.57E-08	17.1	26.7	66.2	91.7	157.7	12.9	13.9	
LSHR(0.03C)-50 µm	DRO1-C1	704	793	1.33E-08	13.7	33.2	112.2	171.4	326.5	6.5	9.5	
LSHR(0.03C)-50 µm	DRO1-C2	815	448	2.47E-08	8.5	19.4	62.9	89.7	143.4	12.4	13.7	
Rene´ 80-200 µm	RMX3-C3	704	793	1.17E-07	0.1	0.3	13.0	36.0	85.3	16.8	27.1	
Rene´ 80-200 µm	RMX3-C2D	815	448	6.34E-08	0.1	0.2	13.0	56.0	206.6	15.7	20.5	
Rene´ 80-600 µm	RE2-C3	704	793	1.46E-07	0.1	0.3	10.1	27.2	52.1	9.2	20.2	
Rene´ 80-600 µm	RE2-C2	815	448	4.49E-08	0.1	0.3	21.5	82.0	231.6	9.5	24.5	
MM247LC-60 µm	MMX12-C3	704	793	1.49E-08	1.0	5.8	134.3	293.3	314.7	3.2	7.8	
MM247LC-60 µm	MMX12-C5	704	793	1.39E-08	4.8	11.4	149.9	327.2	373.2	3.5	5.8	
MM247LC-60 µm	MMX12-C2	815	448	1.10E-08	2.2	14.1	184.7	312.2	457.9	4.9	6.5	
MM247LC-60 µm	MMX12-C4	815	448	1.36E-08	0.8	7.5	150.4	269.8	353.4	3.8	6.4	
MM247LC-1200 µm	MME4-C1	704	793	3.33E-08	1.3	2.8	33.9	112.0	182.1	5.0	7.9	
MM247LC-1200 µm	MME4-C3	704	793	4.69E-08	0.8	1.9	20.3	80.6	121.5	5.2	18.8	
MM247LC-1200 µm	MME4-C2	815	448	7.13E-09	3.3	23.6	276.8	450.9	691.6	5.8	13.1	
MM247LC-1200 µm	MME4-C4	815	448	6.64E-09	22.1	66.3	291.9	450.7	602.7	4.5	8.0	
LDS1101+Hf	7P-8	704	793	4.18E-09	18.0	22.7	50.5	338.8	3716.2	22.1	31.1	3.2
LDS1101+Hf	7N-9T	704	793	7.33E-09	16.6	20.9	42.1	164.1	2680.9	20.3	33.5	0.8
LDS1101+Hf	7N-13T	760	621	1.40E-09	24.0	191.4	1378.4	2268.7	4977.1	21.4	28.3	0.8
LDS1101+Hf	7N-10T	760	621	1.67E-09	10.0	32.5	1119.7	2072.8	4653.2	29.7	19.5	0.8
LDS1101+Hf	7O-9	815	448	4.31E-10	485.0	913.0	2100.0	2460.0	4154.2	37.5	38.5	2.7
LDS1101+Hf	7N-14T	815	448	1.03E-09	35.4	195.0	1873.8	2365.5	4125.7	33.8	39.5	0.8

TABLE 5.—NOTCHED GAGE FATIGUE TEST RESULTS

Material-Grain Size	Specimen	Temperature – °C	Maximum Stress -MPa	Minimum Stress -MPa	Frequency or Dwell	Fatigue Life -cycles	Life-h	Degrees off [001]	Notes
LSHR-15 μm	P3-19	704	793	40	0.5 hertz	583,474	324.2		
LSHR-15 μm	P3-13	815	621	31	0.5 hertz	223,928	124.4		
LSHR-15 μm	T2W-SPL1	815	621	31	0.33 hertz	62,003	51.7		
LSHR-15 μm	P3-3	704	793	40	90 s Min. Stress	25,089	332.9		
LSHR-15 μm	P3-8	704	793	40	90 s Min. Stress	12,910	329.9		
LSHR-15 μm	P3-4	815	448	22	90 s Min. Stress	8,707	332.9		
LSHR-15 μm	P3-11	815	448	22	90 s Min. Stress	9,313	238.0		
LSHR-15 μm	P3-14	815	621	31	90 s Min. Stress	3,060	78.2		
LSHR-15 μm	P3-15	815	621	31	90 s Min. Stress	3,147	80.4		
LSHR-15 μm	P3-16	815	448	22	90 s Max. Stress	12,395	316.8		
LSHR-15 μm	P3-12	815	621	31	90 s Max. Stress	1,372	35.1		
LSHR-15 μm	T1N-SPL1	815	621	31	90 s Max. Stress	2,345	59.9		
LSHR-50 μm	T4-11	704	793	40	0.5 hertz	301,610	167.6		
LSHR-50 μm	T4-14	815	621	31	0.5 hertz	124,404	69.1		
LSHR-50 μm	T4-7	704	793	40	90 s Min. Stress	24,238	619.4		
LSHR-50 μm	T4-9	704	793	40	90 s Min. Stress	10,809	276.2		
LSHR-50 μm	T4-8	815	448	22	90 s Min. Stress	23,330	596.2		
LSHR-50 μm	T4-10	815	448	22	90 s Min. Stress	17,335	443.0		
LSHR-50 μm	T4-16	815	621	31	90 s Min. Stress	3,913	100.0		
LSHR-50 μm	T4-19	815	621	31	90 s Min. Stress	4,842	123.7		
LSHR(.03C)-50 μm	DRO-7	815	621	31	0.33 hertz	45,531	37.9		
LSHR(.03C)-50 μm	DRO-11	815	621	31	90 s Max. Stress	2,548	65.1		
LSHR(.03C)-50 μm	DRO-15	815	621	31	90 s Max. Stress	2,801	71.6		
MM247LC-60 μm	MMX11	704	793	40	90 s Min. Stress	16,500	421.7		
MM247LC-60 μm	MMX16	704	793	40	90 s Min. Stress	18,039	461.0		
MM247LC-60 μm	MMX14	815	448	22	90 s Min. Stress	30,778	786.5		
MM247LC-1200 μm	ME7	704	793	40	90 s Min. Stress	13,025	332.9		
MM247LC-1200 μm	ME12	704	793	40	90 s Min. Stress	3,177	81.2		
MM247LC-1200 μm	ME2	815	448	22	90 s Min. Stress	10,359	264.7		
MM247LC-1200 μm	ME9	815	448	22	90 s Min. Stress	45,047+	1,151.2 +		Interrupted
LDS1101+Hf	7K-N1	815	621	31	0.33 hertz	561,260	467.7	4.5	
LDS1101+Hf	7M2	704	793	40	90 s Min. Stress	54,215	1,385.5	0.3	
LDS1101+Hf	7M1	815	448	22	90 s Min. Stress	99,901 +	2,553 +	0.3	Interrupted
LDS1101+Hf	7M3	815	621	31	90 s Min. Stress	29,994	766.5	0.3	
LDS1101+Hf	7M4	815	621	31	90 s Min. Stress	25,376	648.5	0.3	
LDS1101+Hf	7K-N2	815	621	31	90 s Max. Stress	37,311	953.5	4.8	
LDS1101	64-N2	815	621	31	0.33 hertz	894,274	745.2	2.5	
LDS1101	64-N1	704	793	40	90 s Min. Stress	20,156	515.1	2.5	
LDS1101	64-N3	815	621	31	90 s Min. Stress	23,503	600.6	2.5	
LDS1101	64-N4	815	621	31	90 s Max. Stress	31,096	794.7	2.5	

TABLE 6.—UNIFORM GAGE FATIGUE TEST RESULTS

Material-Grain Size	Specimen	Temperature °C	Modulus -GPa	Total Strain Range - %	Plastic Strain Range -%	Maximum Stress - MPa	Minimum Stress - MPa	Alternating Pseudo-Stress - MPa	Smith-Watson-Topper Stress - MPa	Fatigue Life -cycles	Life -h	Specimen Degrees off [001]
LSHR-15 μm	T2-L6	704	187	0.53	0.01	903	-68	495	662	714,295	44.2	
LSHR-15 μm	T2-L3	704	187	0.76	0.04	903	-433	710	776	80,855	25.2	
LSHR-15 μm	P3-33	704	187	1.00	0.12	936	-706	934	876	7,635	4.2	
LSHR-15 μm	T2-L1	704				993	-317	655	806	113,540	94.6	
LSHR-15 μm	T2-L2	760	184	0.53	0.00	922	-34	488	664	283,728	31.0	
LSHR-15 μm	P3-35	760	181	0.76	0.06	843	-427	689	731	65,590	24.7	
LSHR-15 μm	P3-34	815	174	0.53	0.01	719	-187	460	571	1,395,924	61.8	
LSHR-15 μm	P3-36	815	178	0.76	0.06	749	-479	676	678	22,309	12.4	
LSHR-15 μm	T2-L5	815	174	1.00	0.11	845	-702	869	809	2,542	1.4	
LSHR-50 μm	T4-29	704	185	0.53	0.00	917	-50	490	666	272,625	40.7	
LSHR-50 μm	T4-26	704	185	0.76	0.01	953	-408	702	805	7,359	4.1	
LSHR-50 μm	T4- 3	704	183	1.00	0.06	967	-743	914	909	2,552	1.4	
LSHR-50 μm	T4-18	704				993	-317	655	806	55,058	45.9	
LSHR-50 μm	T4-25	760	180	0.53	0.00	904	-40	477	653	131,269	26.9	
LSHR-50 μm	T4- 5	760	179	0.76	0.03	880	-402	681	751	13,996	7.8	
LSHR-50 μm	T4- 4	815	177	0.53	0.01	765	-152	468	592	56,086	31.2	
LSHR-50 μm	T4-17	815	175	0.76	0.04	792	-451	666	702	6,983	3.9	
LSHR-50 μm	T4-28	815	177	1.00	0.13	833	-670	883	791	1,938	1.1	
LDS1101+Hf	7JL3	704	105	1.00	0.01	785	-268	524	642	31,284	17.4	5.0
LDS1101+Hf	7JL2	815	101	0.76	0.01	717	-37	383	520	1,331,508	60.8	7.5
LDS1101+Hf	7JL4	815	95	1.00	0.01	790	-154	476	611	51,444	25.4	4.2
LDS1101+Hf	7JL1	815	96	1.35	0.00	818	-481	647	729	6,071	3.4	7.7
LDS1101	66L1	704	103	1.00	0.00	832	-195	517	654	36,832	20.5	2.9
LDS1101	66L4	815	94	0.76	0.01	647	-59	356	478	2,604,099	96.2	5.5
LDS1101	66L2	815	95	1.00	0.01	793	-153	476	612	33,915	18.8	3.8
LDS1101	66L3	815	93	1.35	0.01	827	-423	628	719	5,295	2.9	4.6
LDS4583	24L3	704	107	1.00	0.00	821	-248	534	662	23,625	13.1	3.2
LDS4583	24L2	815	96	0.76	0.00	648	-84	364	487	1,091,905	115.8	2.3
LDS4583	24L1	815	98	1.00	0.01	841	-131	490	639	25,007	13.9	3.0
LDS4583	24L4	815	96	1.35	0.02	879	-394	647	748	5,439	3.0	3.6/6.8*

* Subgrain

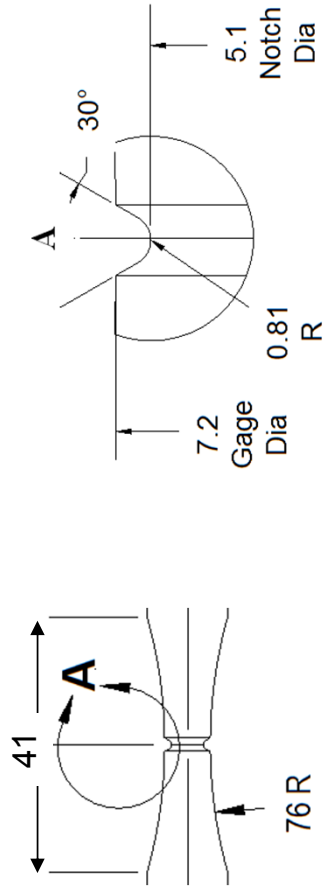

Fig. 1.—Notch fatigue specimen configuration, dimensions in mm.

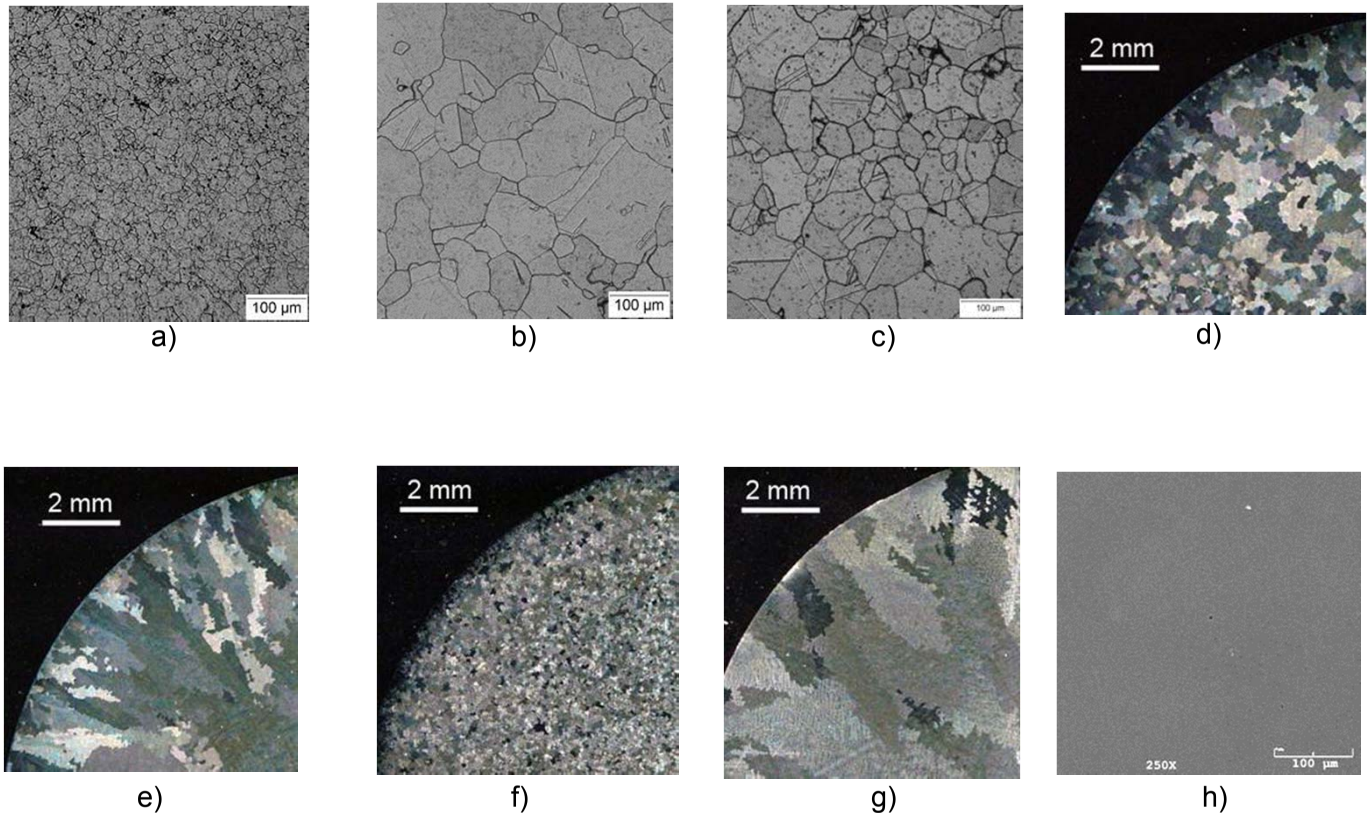

Fig. 2.—Typical alloy microstructure images illustrating (mean linear intercept) grain sizes for: a) LSHR (15 µm), b) LSHR (50 µm), c) LSHR 0.03C (50 µm), d) Rene´ 80 (200 µm), e) Rene´ 80 600 µm, f) Mar-M247LC (60 µm), g) Mar-M247LC (1200 µm), h) LDS-1101+Hf (single crystal).

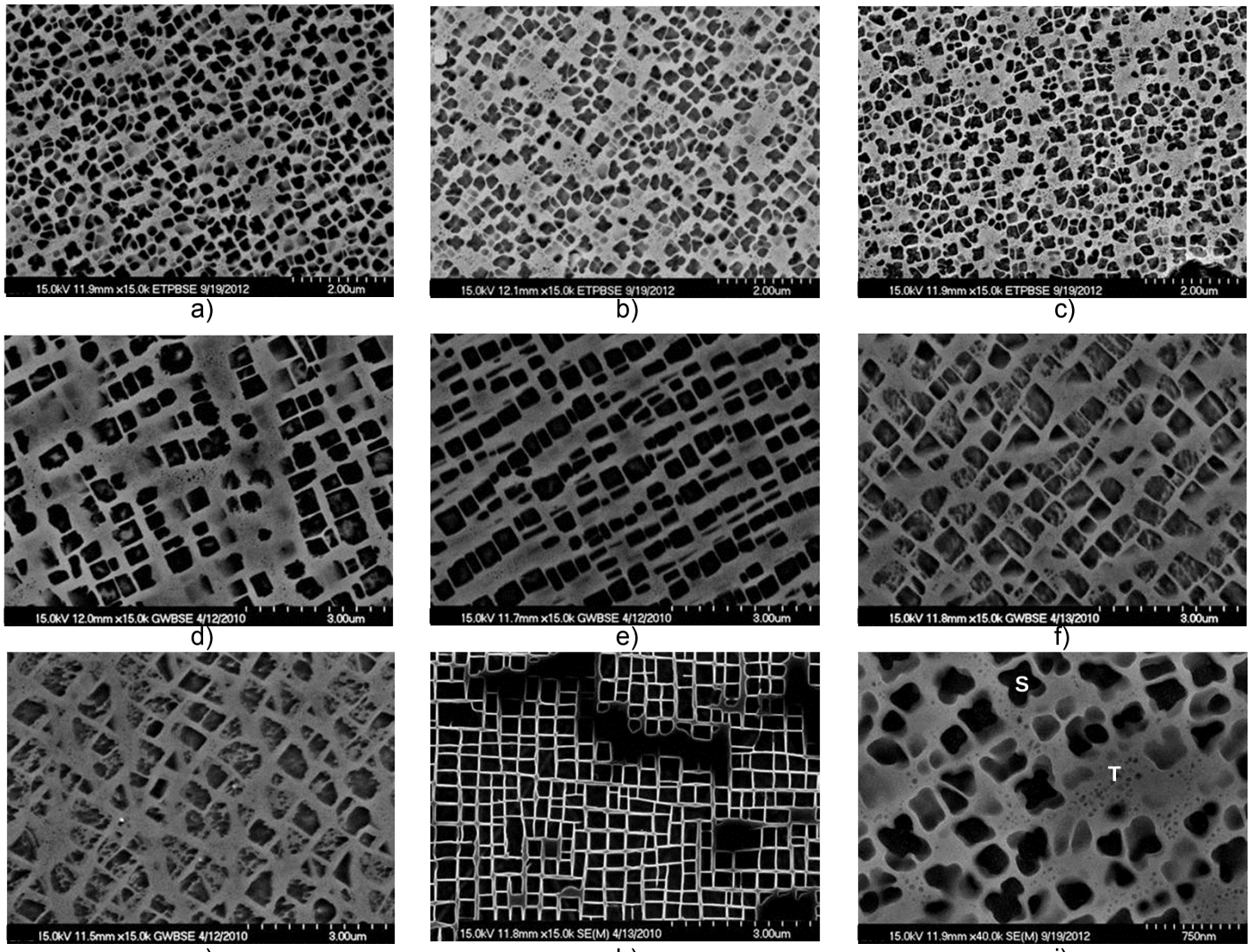

Fig. 3.—Typical alloy microstructure images illustrating γ ′ precipitates: a) LSHR (15 μm), b) LSHR (50 μm), c) LSHR 0.03C (50 μm), d) Rene′ 80 (200 μm), e) Rene′ 80 (600 μm), f) Mar-M247LC (60 μm), g) Mar-M247LC (1200 μm), h) LDS-1101+Hf (single crystal), i) LSHR (15 μm), higher magnification image showing representative secondary (S) and tertiary (T) γ’ precipitates.

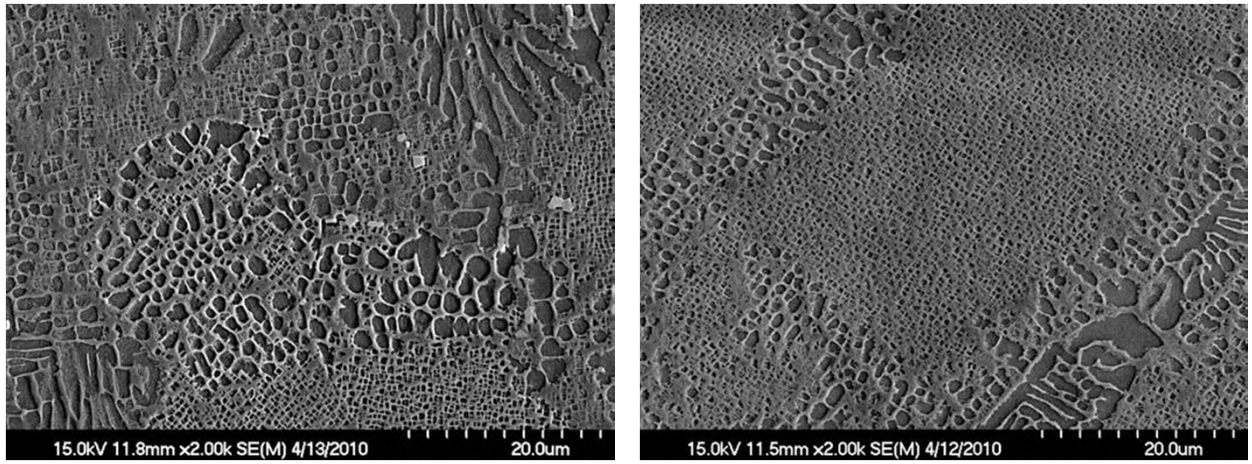

a) b)

Fig. 4.—Images illustrating wide range of γ ´ precipitate sizes present for: a) Mar-M247LC (60 μm grain size), b) Mar-M247LC (1200 μm grain size).

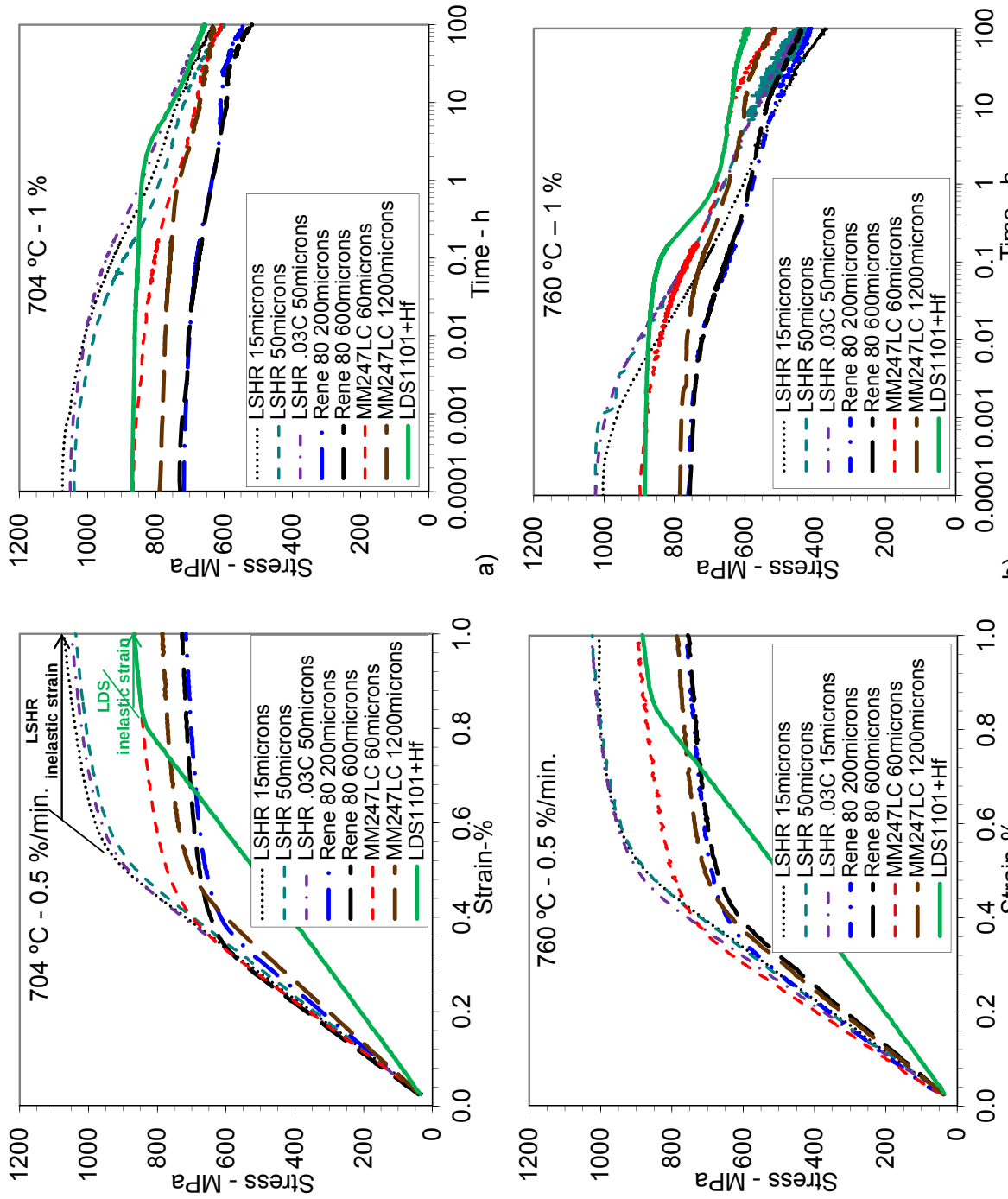

Fig. 5.—Comparisons of typical initial tensile stress versus strain response and subsequent stress relaxation at 1% strain: a) 704 °C, with typical LSHR and LDS inelastic strains indicated, and b) 760 °C.

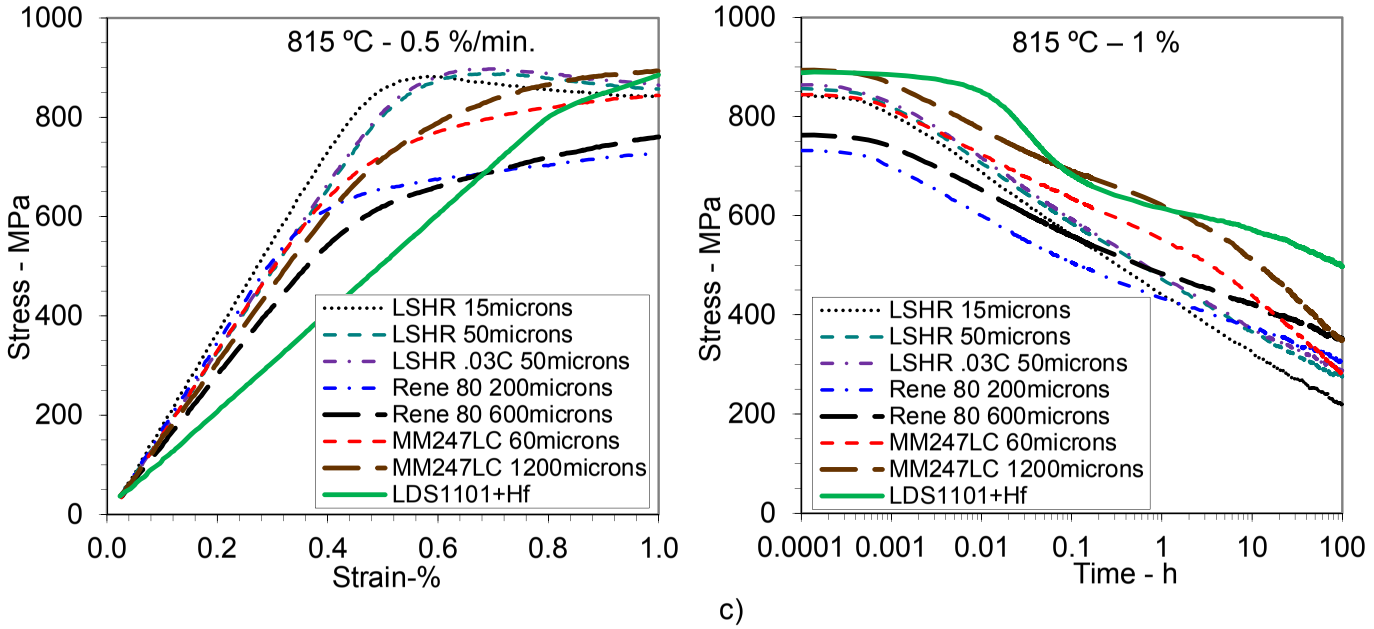

c)

Fig. 5 (cont.).—Comparison of typical initial tensile stress versus strain response and subsequent stress relaxation at 1% strain: c) 815. °C.

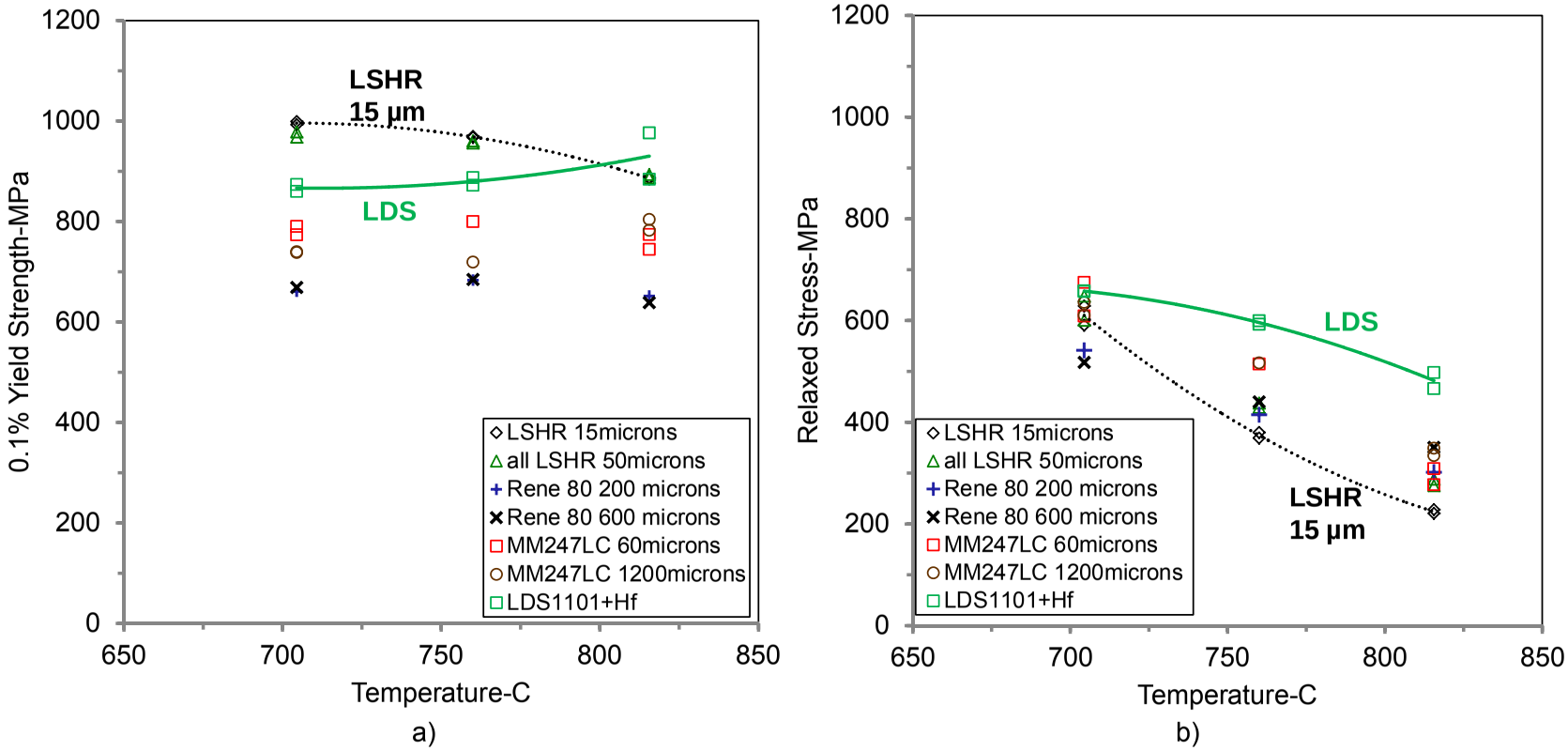

Fig. 6.—Comparisons of tensile responses as function of temperature: a) 0.1% yield strength, b) stress at 1% strain after relaxation for 100 h.

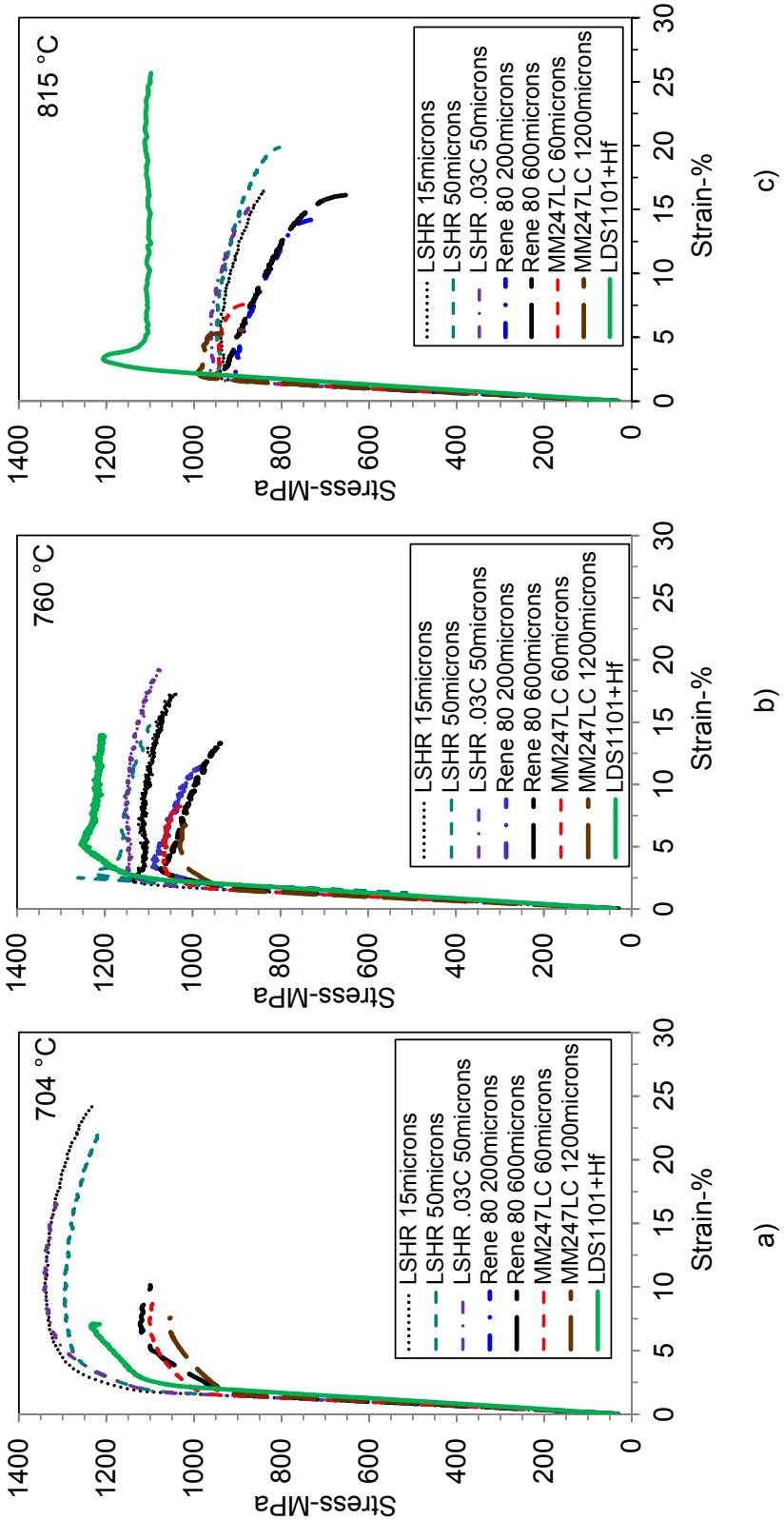

Fig. 7.—Comparisons of typical tensile stress versus average strain response at average strain rate of 5%/min up to failure, after completion of stress relaxation for 100 h: a) 704 °C, b) 760 °C , c) 815 °C.

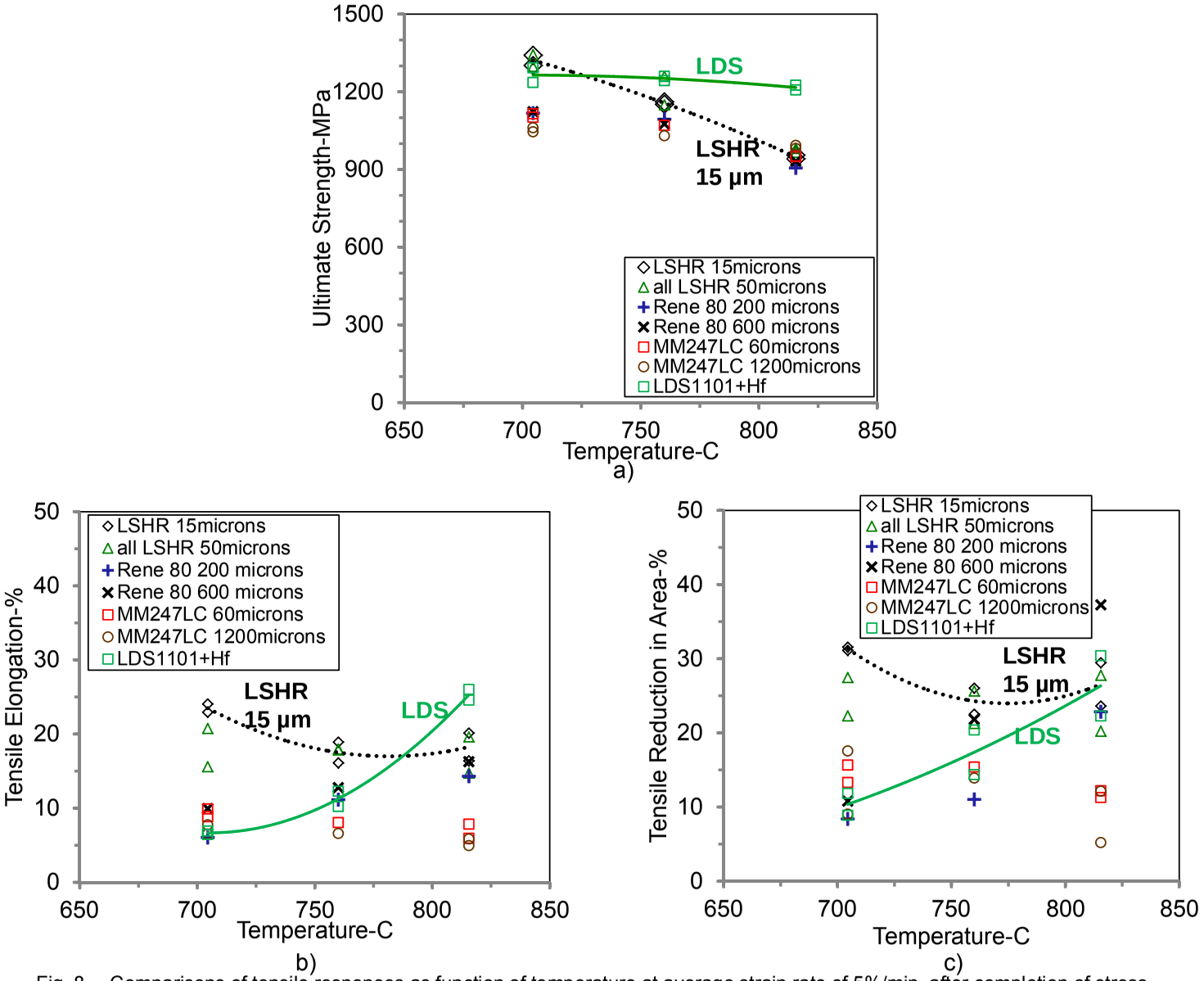

Fig. 8.—Comparisons of tensile responses as function of temperature at average strain rate of 5%/min, after completion of stress relaxation for 100 h: a) ultimate strength, b) elongation at failure, c) reduction in area at failure.

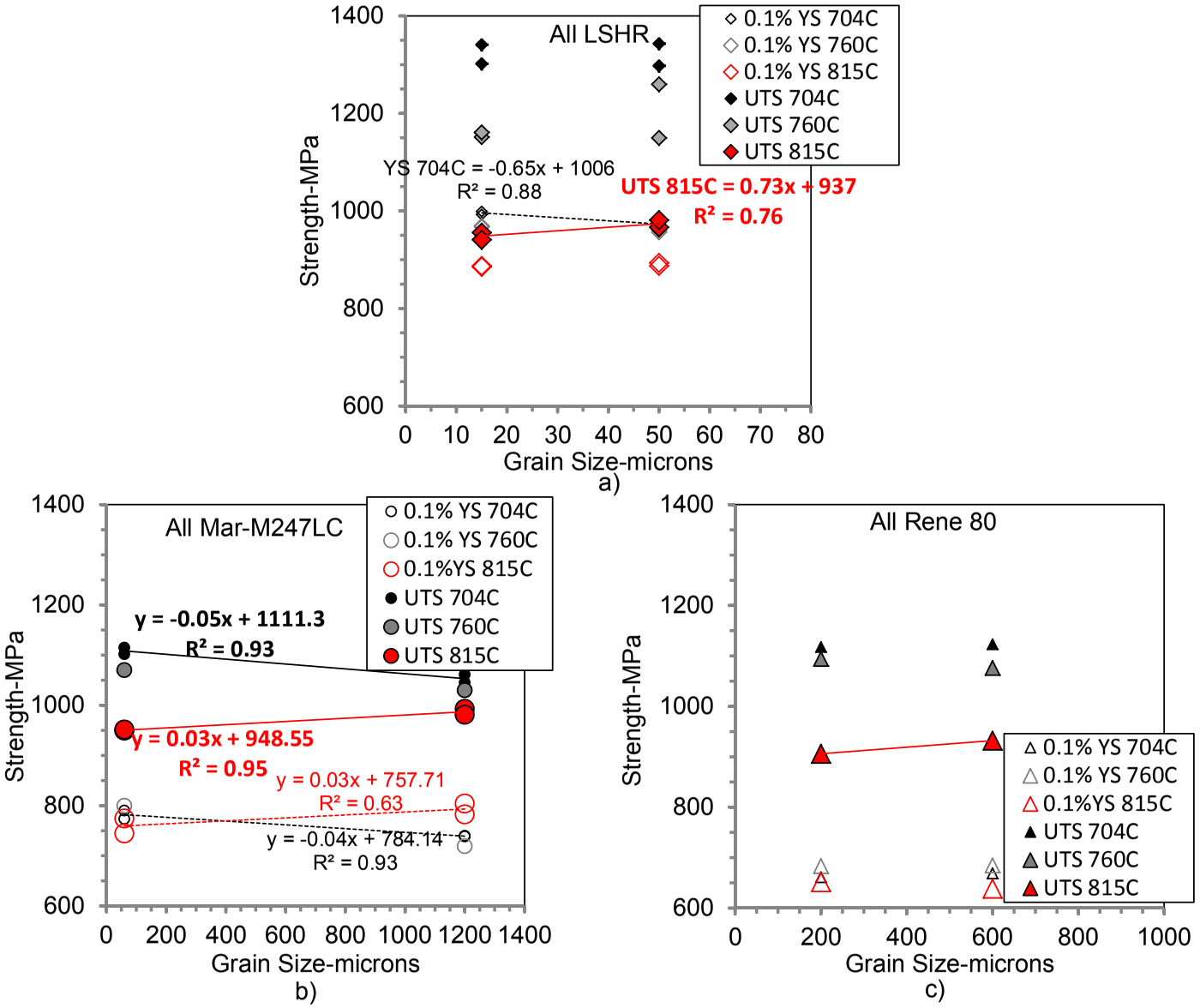

Fig. 9.—Comparisons of yield and ultimate strength versus grain size for a) LSHR, b) Mar-M247LC, c) Rene′ 80.

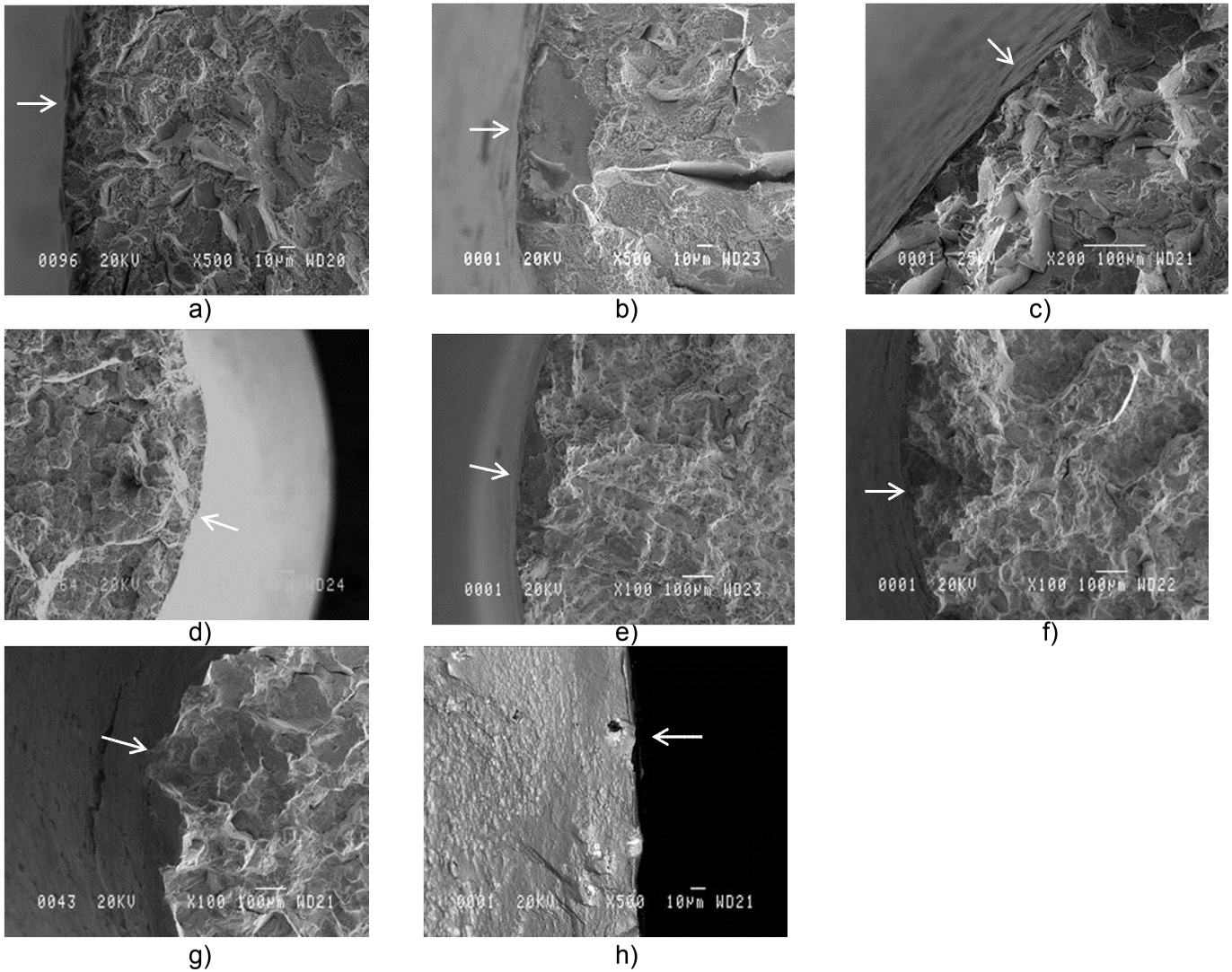

Fig. 10.—Comparison of surface failure initiation points (arrows) for tensile tests at 704 °C: a) LSHR (15 µm), b) LSHR (50 µm), c) LSHR 0.03C (50 µm), d) Rene´ 80 (200 µm), e) Rene´ 80 (600 µm), f) Mar-M247LC (60 µm), g) Mar-M247LC (1200 µm), h) LDS-1101+Hf (single crystal).

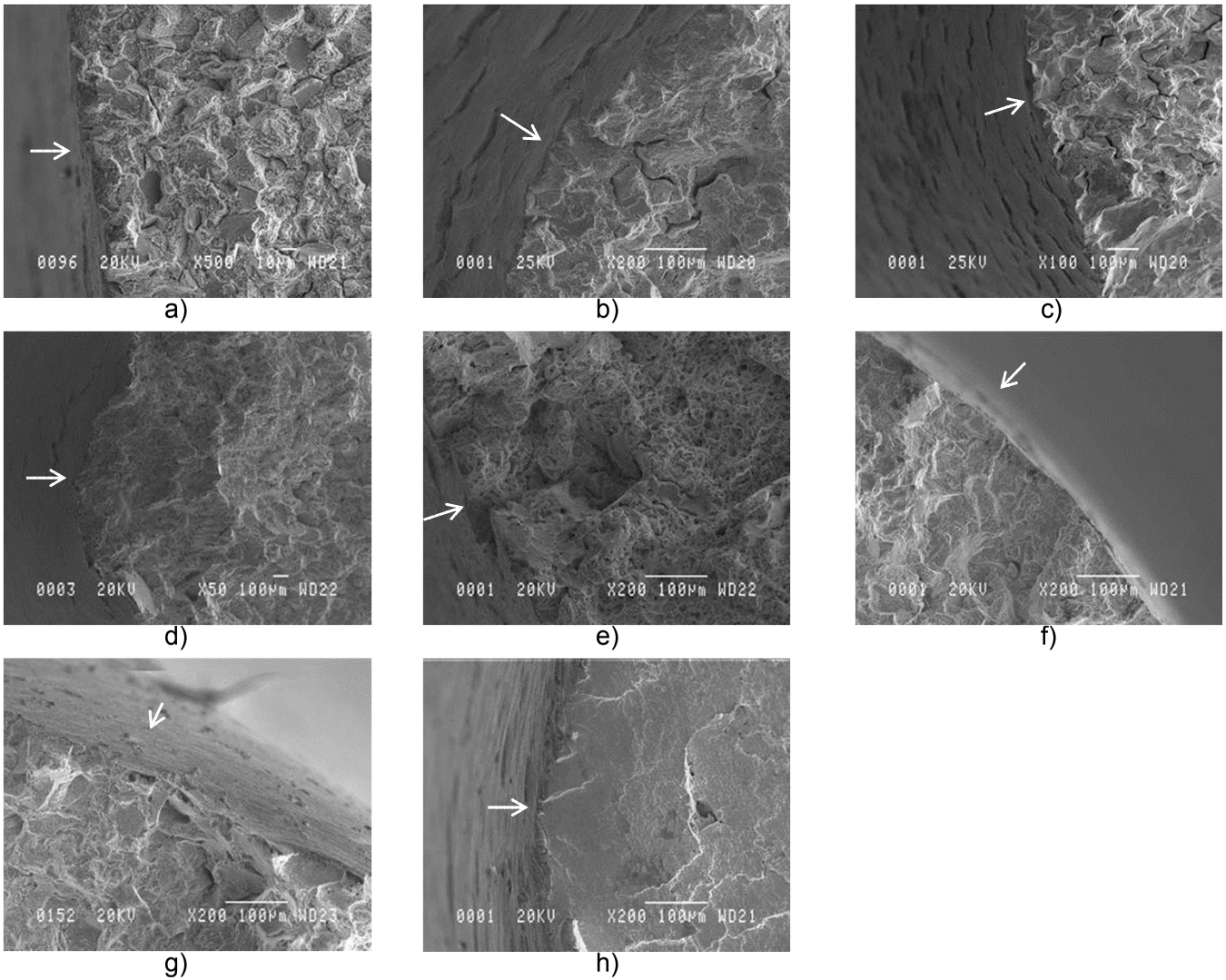

Fig. 11.—Comparison of surface failure initiation modes for tensile tests at 815 °C: a) LSHR (15 µm), b) LSHR (50 µm), c) LSHR 0.03C (50 µm), d) Rene´ 80 (200 µm), e) Rene´ 80 (600 µm), f) Mar-M247LC (60 µm), g) Mar-M247LC (1200 µm), h) LDS-1101+Hf (single crystal).

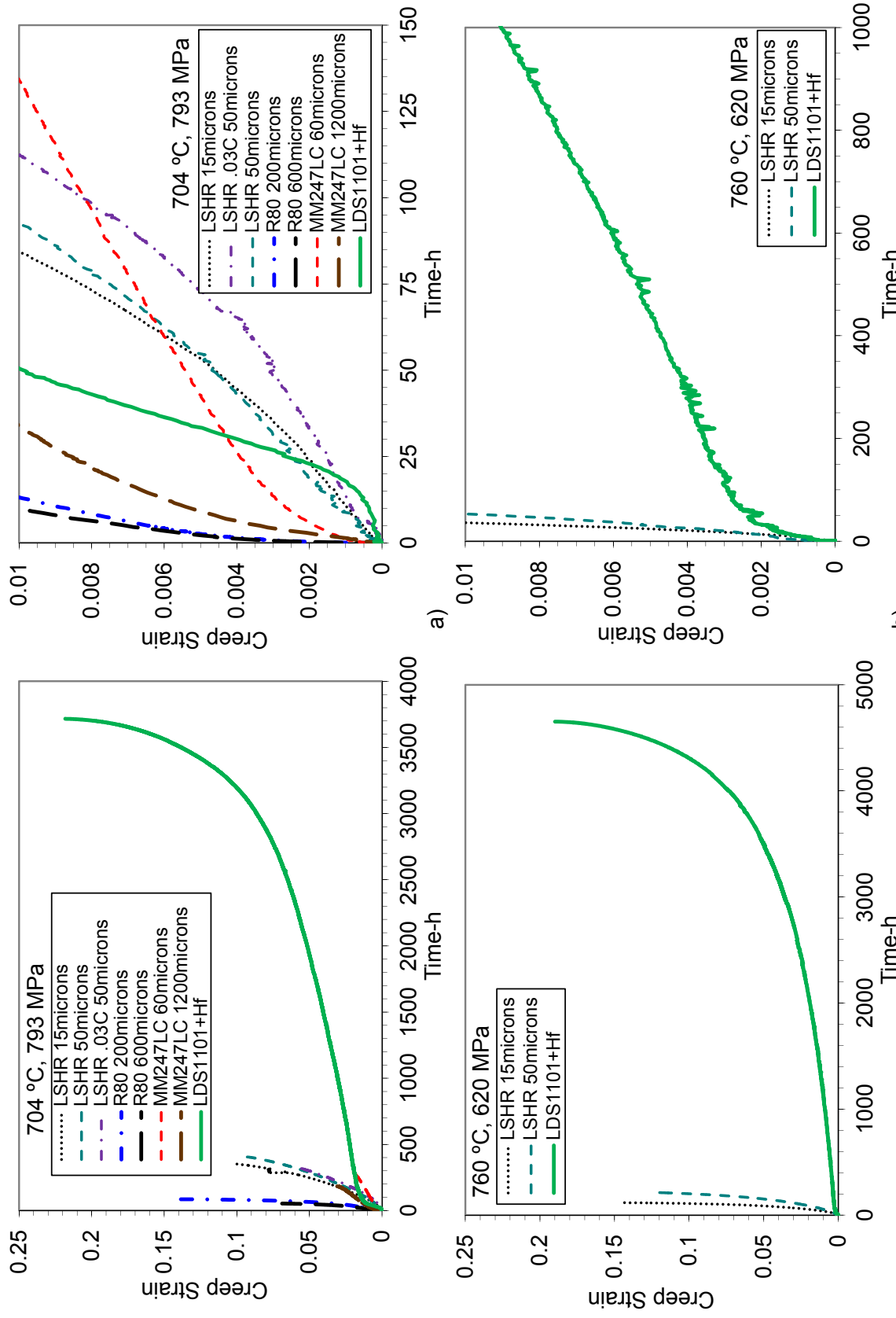

Fig. 12.—Comparisons of typical creep strain versus time responses at: a) 704 °C, b) 760 °C.

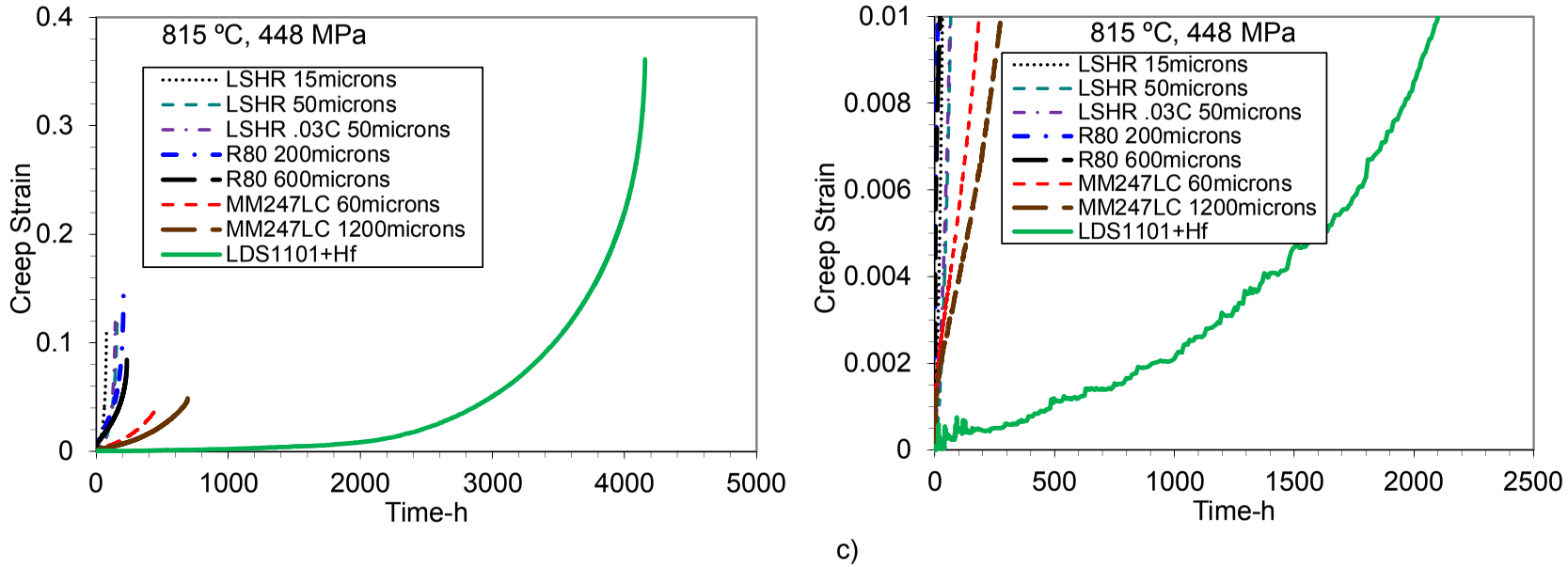

c)

Fig. 12 (cont.).—Comparisons of typical creep strain versus time responses at: c) 815 °C.

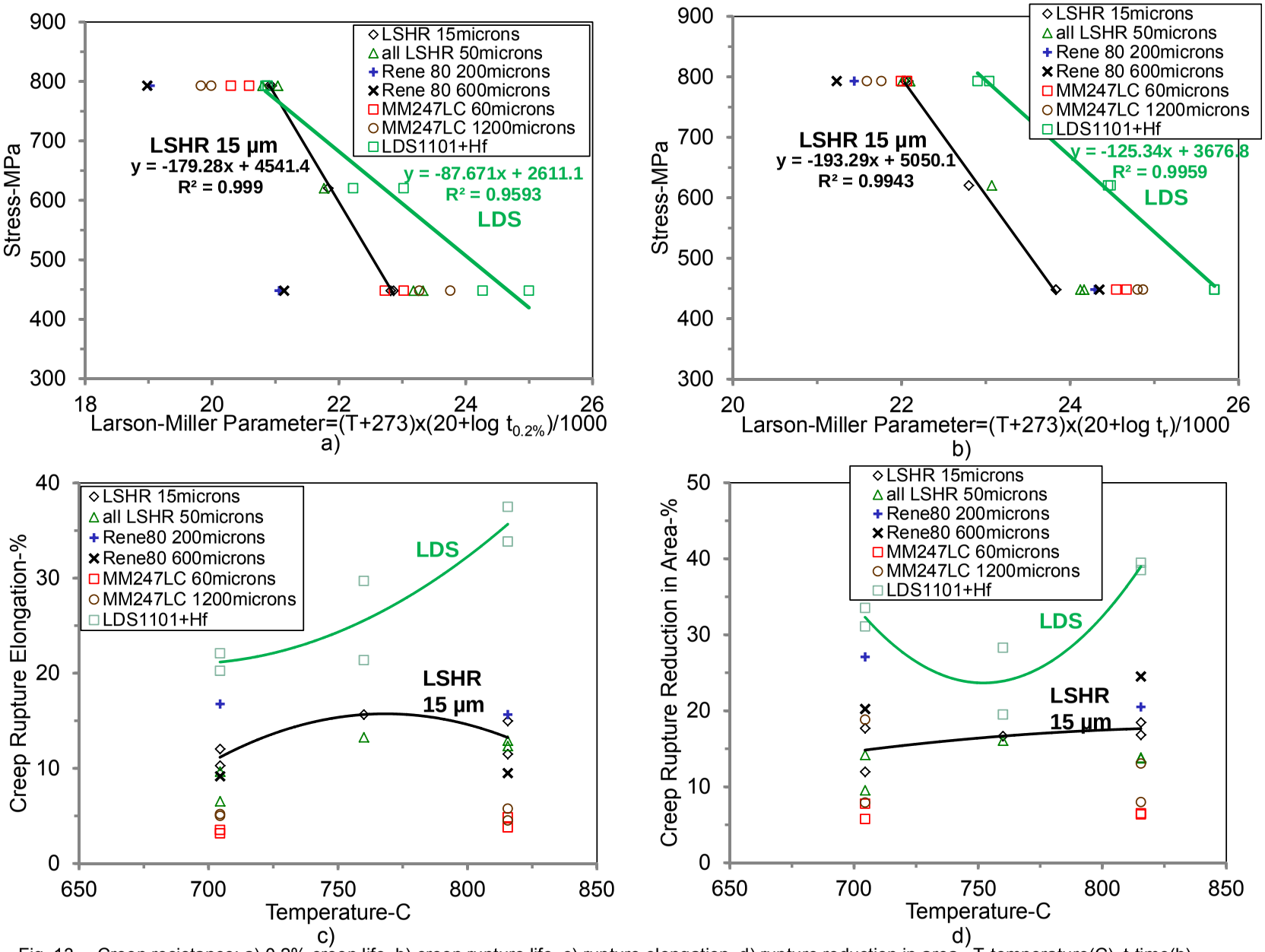

Fig. 13.—Creep resistance: a) 0.2% creep life, b) creep rupture life, c) rupture elongation, d) rupture reduction in area. T-temperature(C), t-time(h).

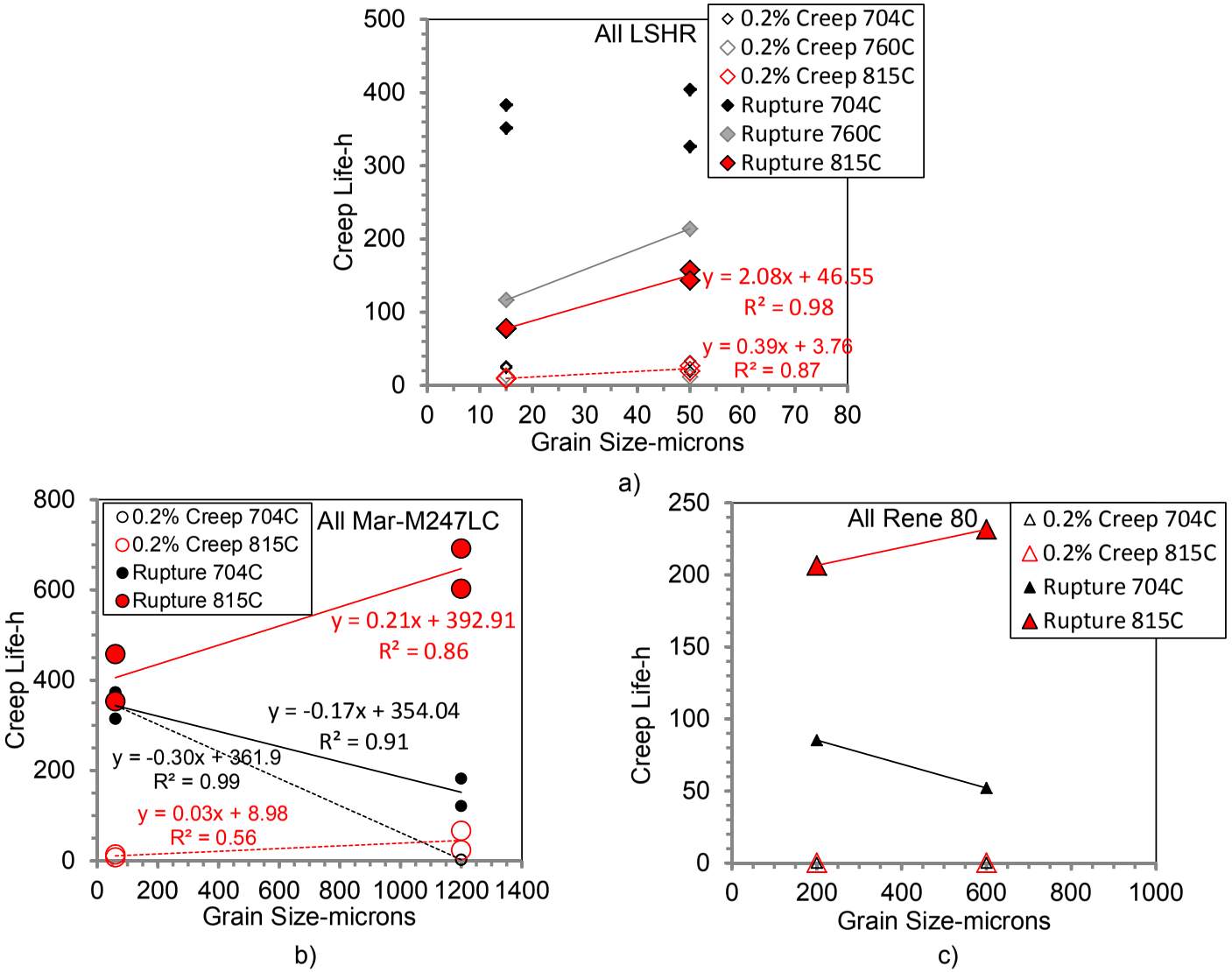

Fig. 14.—Creep resistance versus grain size for: a) LSHR, b) Mar-M247LC, c) Rene′ 80.

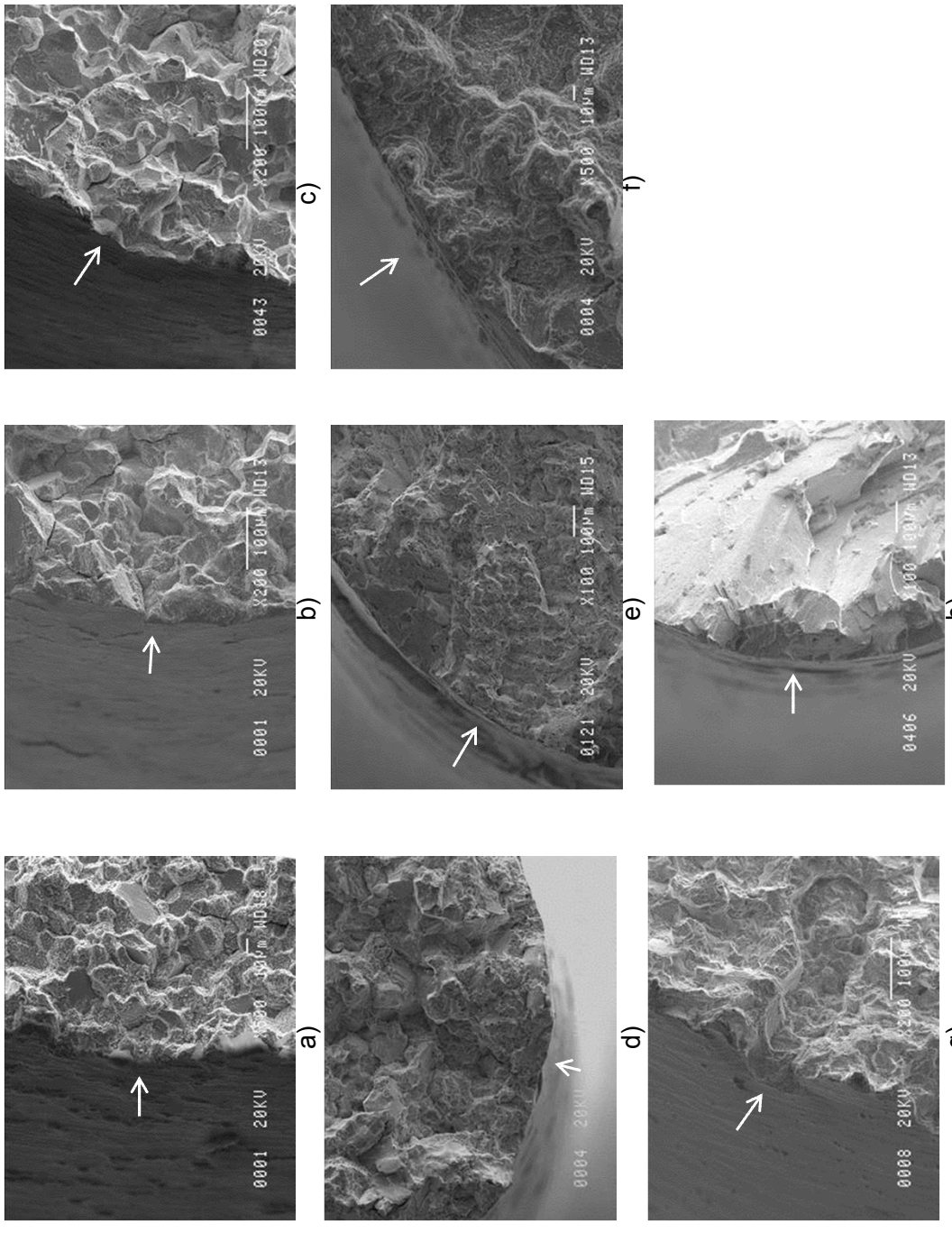

Fig. 15.—Comparison of typical surface failure initiation sites for creep tests at 704 °C: a) LSHR (15 µm), b) LSHR (50 µm), c) LSHR 0.03C (50 µm), d) Rene´ 80 (200 µm), e) Rene´ 80 (600 µm), f) Mar-M247LC (60 µm), g) Mar-M247LC (1200 µm), h) LDS-1101+Hf (single crystal).

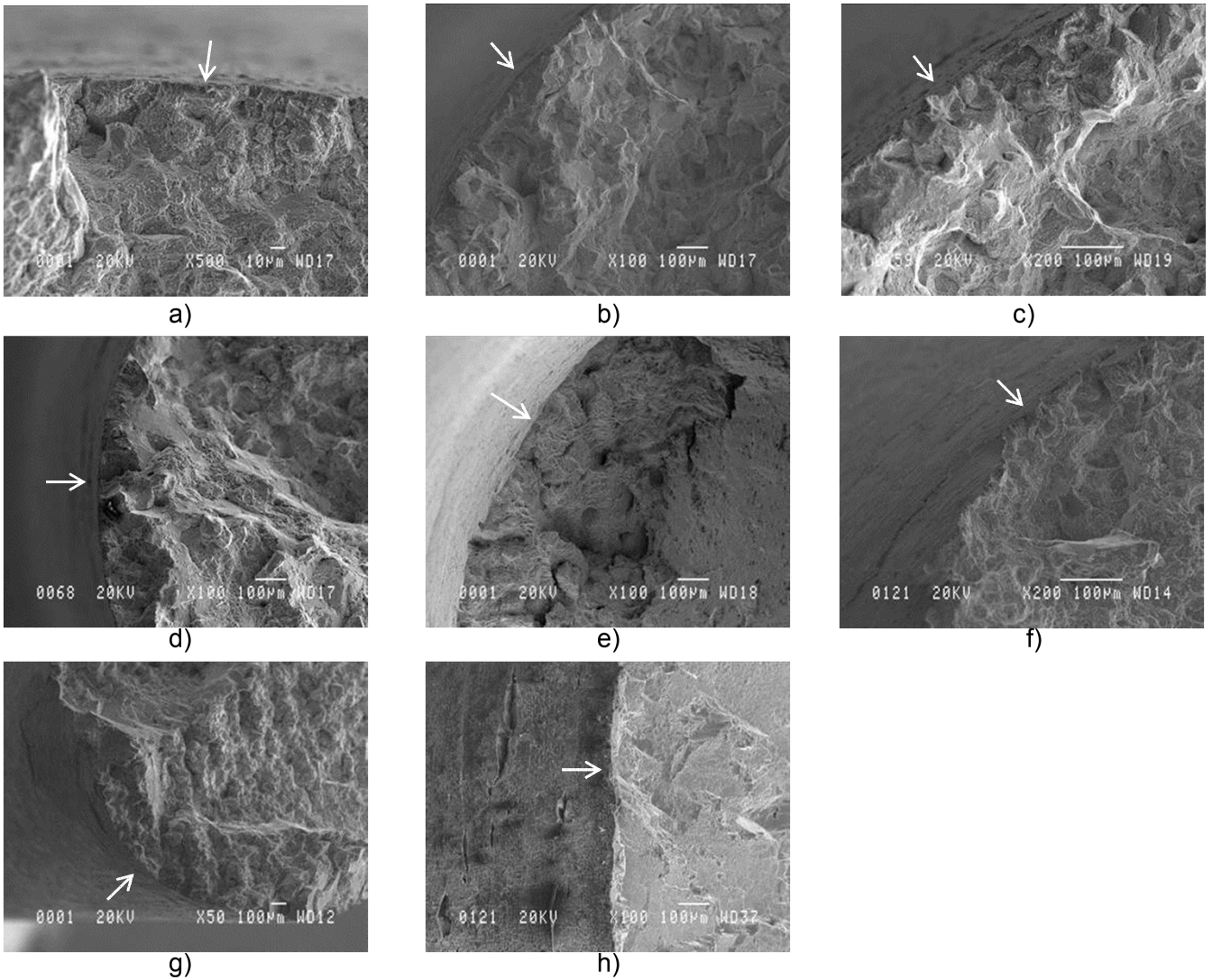

Fig. 16.—Comparison of surface failure initiation sites for creep tests at 815 °C: a) LSHR (15 µm), b) LSHR (50 µm), c) LSHR 0.03C (50 µm), d) Rene´ 80 (200 µm), e) Rene´ 80 (600 µm), f) Mar-M247LC (60 µm), g) Mar-M247LC (1200 µm), h) LDS-1101+Hf (single crystal).

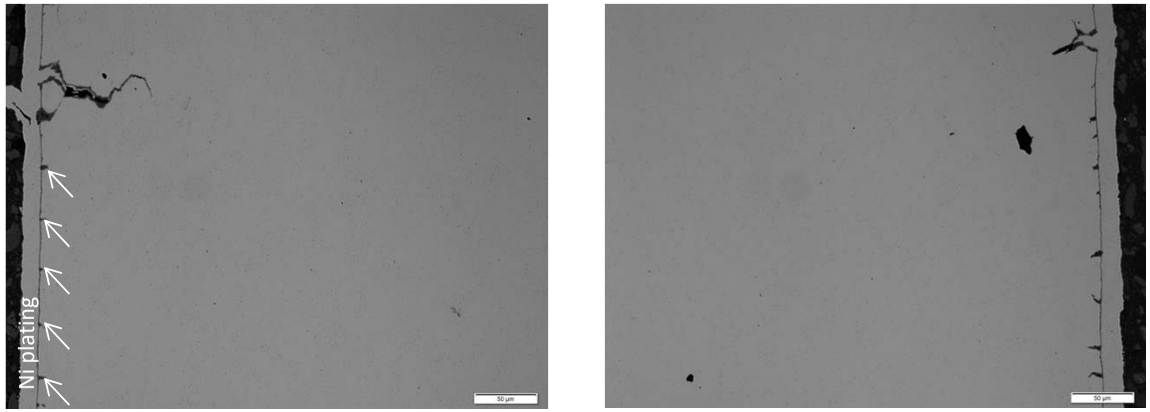

Fig. 17.—Images a) and b) from polished, longitudinal section near fracture surface of 15 µm LSHR after creep rupture life of 383.2 h at 704 °C and 793 MPa. Cracks initiated at the specimen surface and progressed inward along grain boundaries. Smaller cracks are indicated by arrows. Specimens were plated with Ni after testing was completed to protect specimen surfaces during subsequent metallographic preparation.

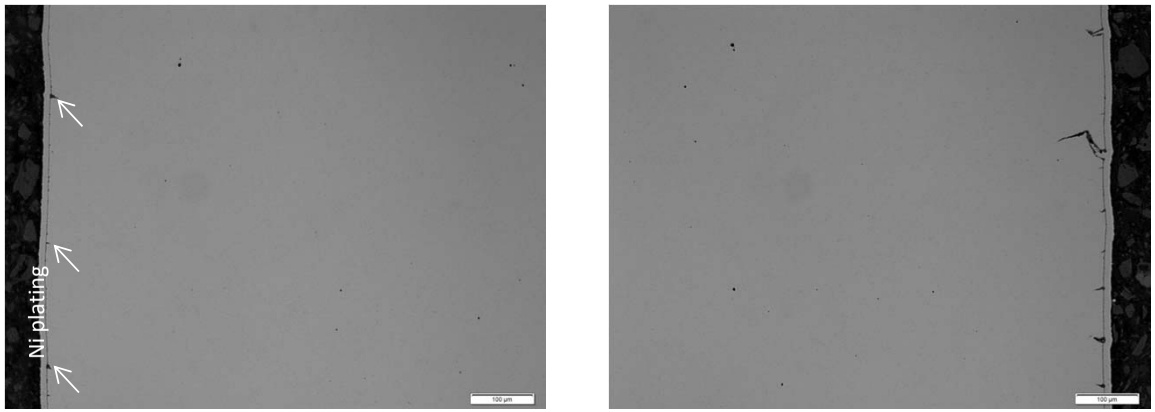

Fig. 18.—Images a) and b) from polished, longitudinal section near fracture surface of 50 µm LSHR after creep rupture life of 404.2 h at 704 °C and 793 MPa. A few cracks initiated at the specimen surface and progressed inward along grain boundaries. Smaller cracks are indicated by arrows.

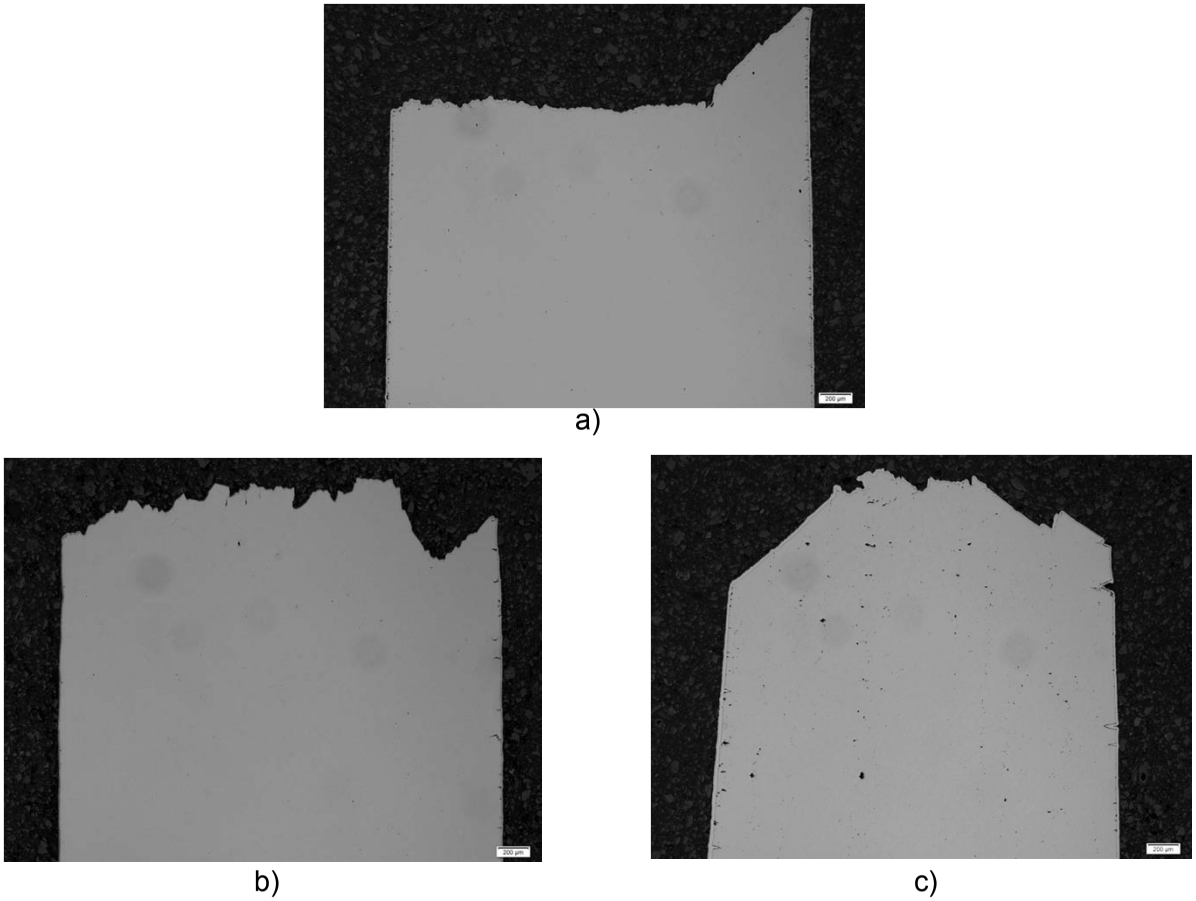

Fig 19.—Polished, longitudinal sections through fracture surfaces after creep rupture at 704 °C and 793 MPa: (a) 15 µm grain size LSHR; (b) 50 µm grain size LSHR; and (c) single crystal LDS-1101+Hf.

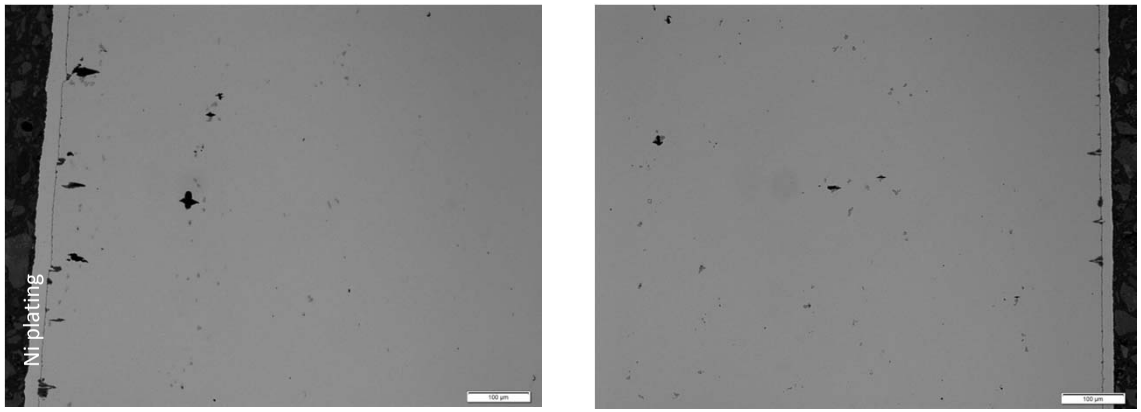

Fig. 20.—Images a) and b) from polished, longitudinal section near fracture surface of single crystal LDS-1101+Hf after creep rupture life of 2680.9 h at 704 °C and 793 MPa. Cracking was only observed in the vicinity of the fracture surface and not well away in the uniform gage section.

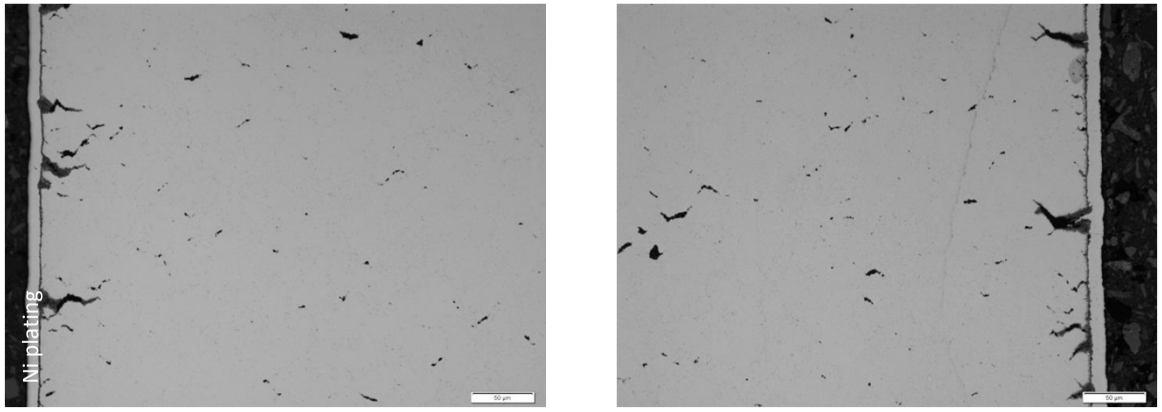

Fig. 21.—Images a) and b) from polished longitudinal section near fracture surface of 15 μm LSHR after creep rupture life of 78 h at 815 °C and 448 MPa. Large cracks were observed to initiate along grain boundaries at the specimen surface, smaller cracks occurred at internal grain boundaries.

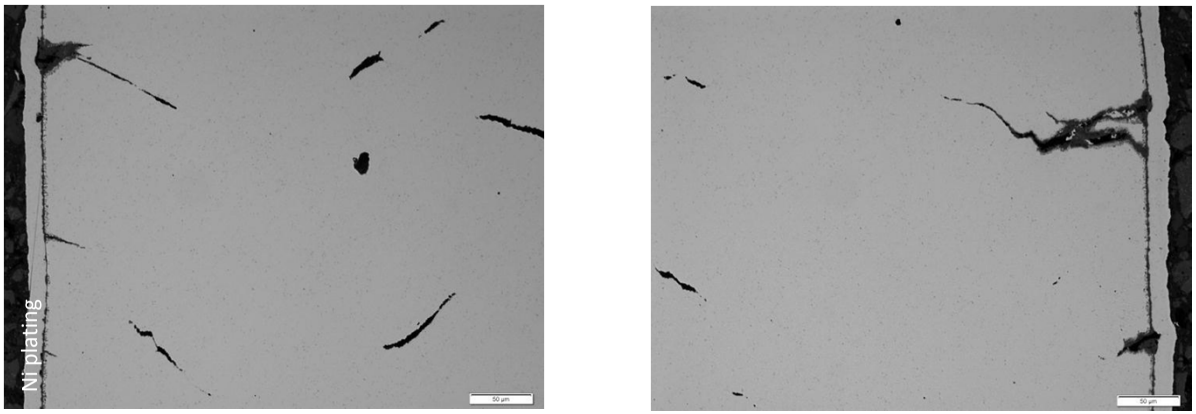

a) b)

Fig. 22.—Polished, longitudinal section near fracture surface of 50 µm LSHR after creep rupture life of 157.7 h at 815 °C and 448 MPa. Large cracks were observed to initiate at grain boundaries along the specimen surface, smaller cracks occurred at internal grain boundaries.

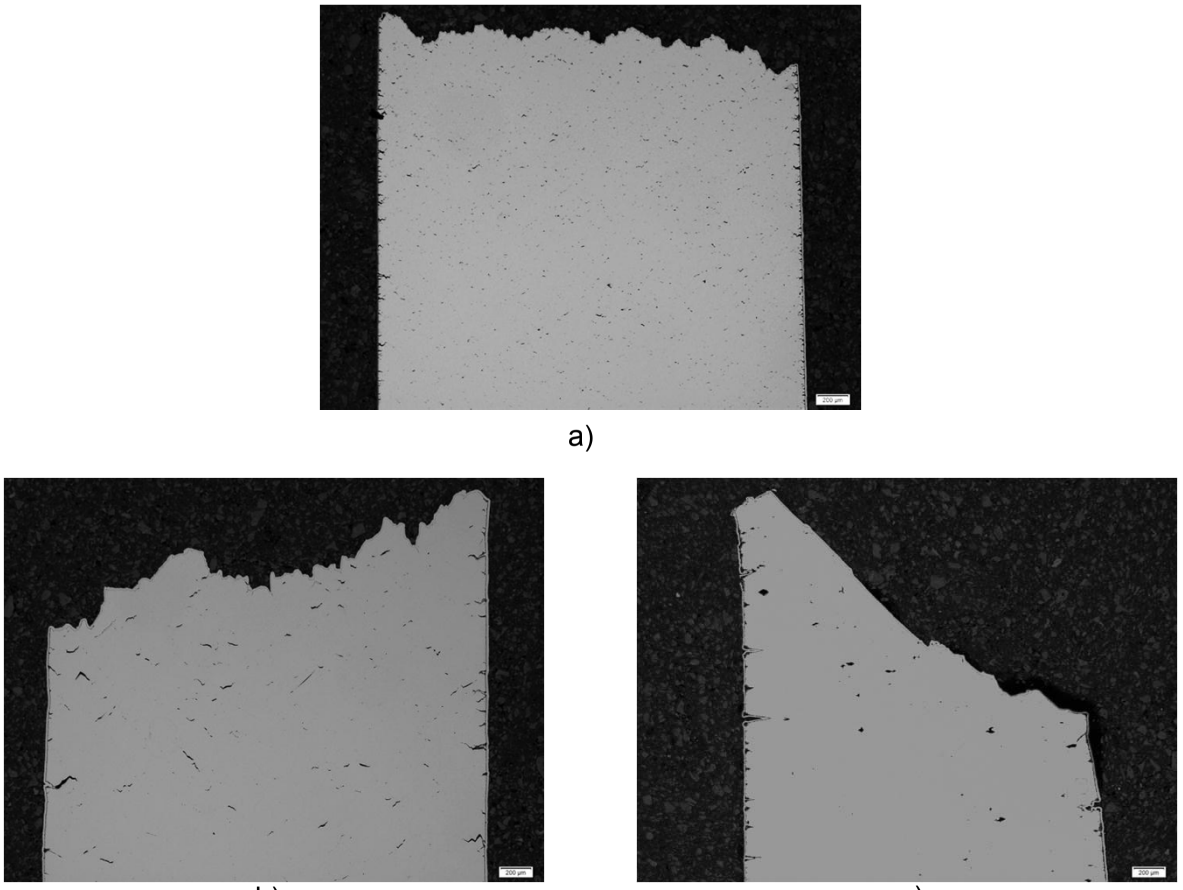

Fig. 23.—Polished, longitudinal sections through fracture surfaces after creep rupture at 815 °C and 448 MPa: (a) 15 µm grain size LSHR; (b) 50 µm grain size LSHR; and (c) single crystal LDS-1101+Hf.

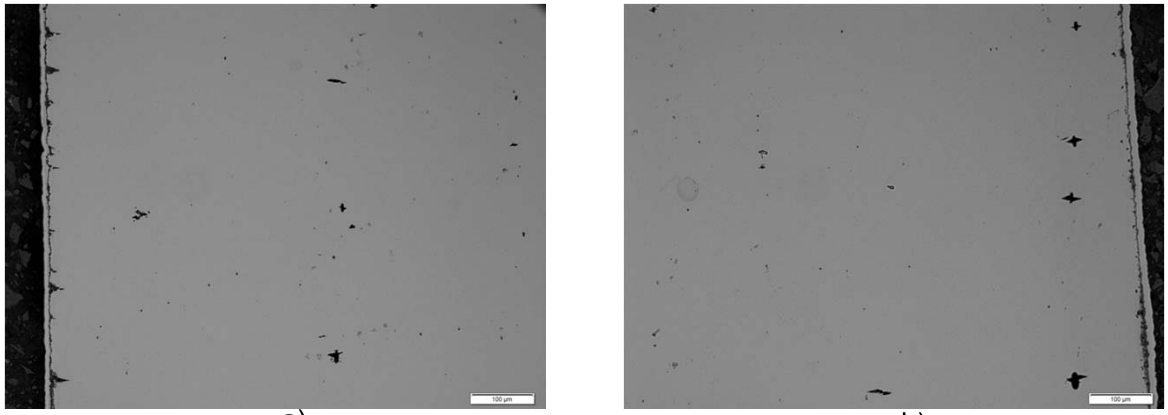

Fig. 24.—Polished, longitudinal section near fracture surface of single crystal LDS-1101+Hf after creep rupture life of 4125.7 h at 815 °C and 448 MPa. Cracks were observed to initiate at the specimen surface as well as at internal porosity. Cracking was observed in the vicinity of the fracture surface and not well away from the fracture surface in the uniform gage section.

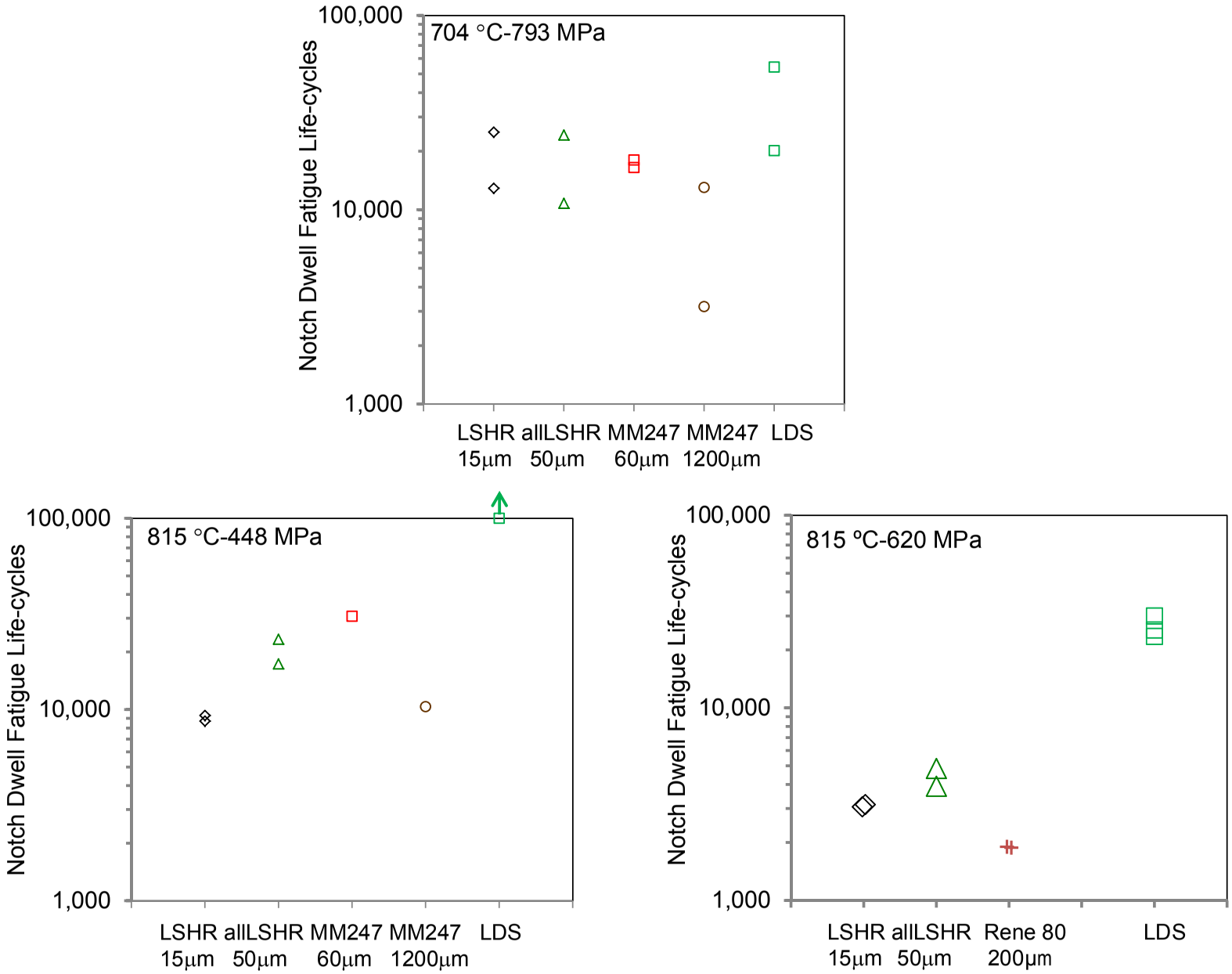

Fig. 25.—Comparisons of notch fatigue lives in cycles with a 90 s dwell at minimum applied stress.

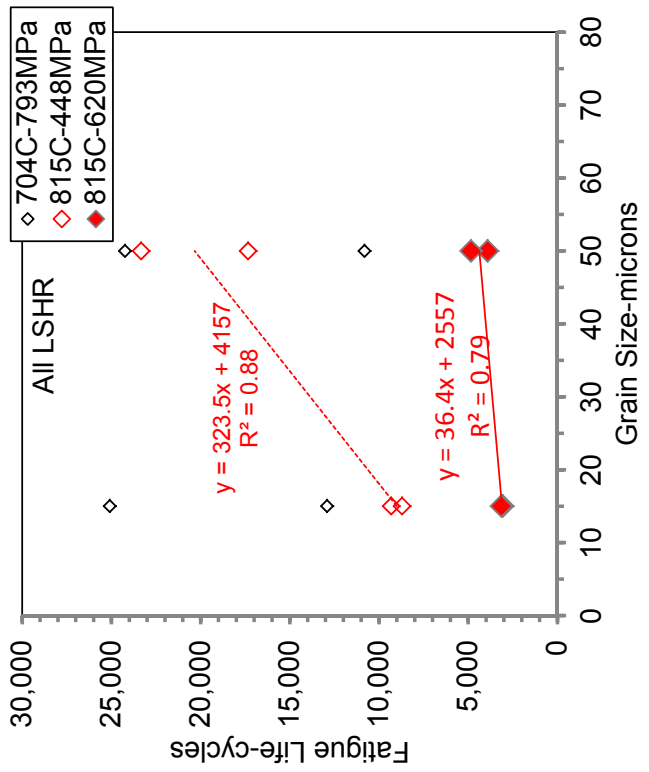

Fig. 26.—Comparisons of notch fatigue life with minimum load dwells versus grain size.

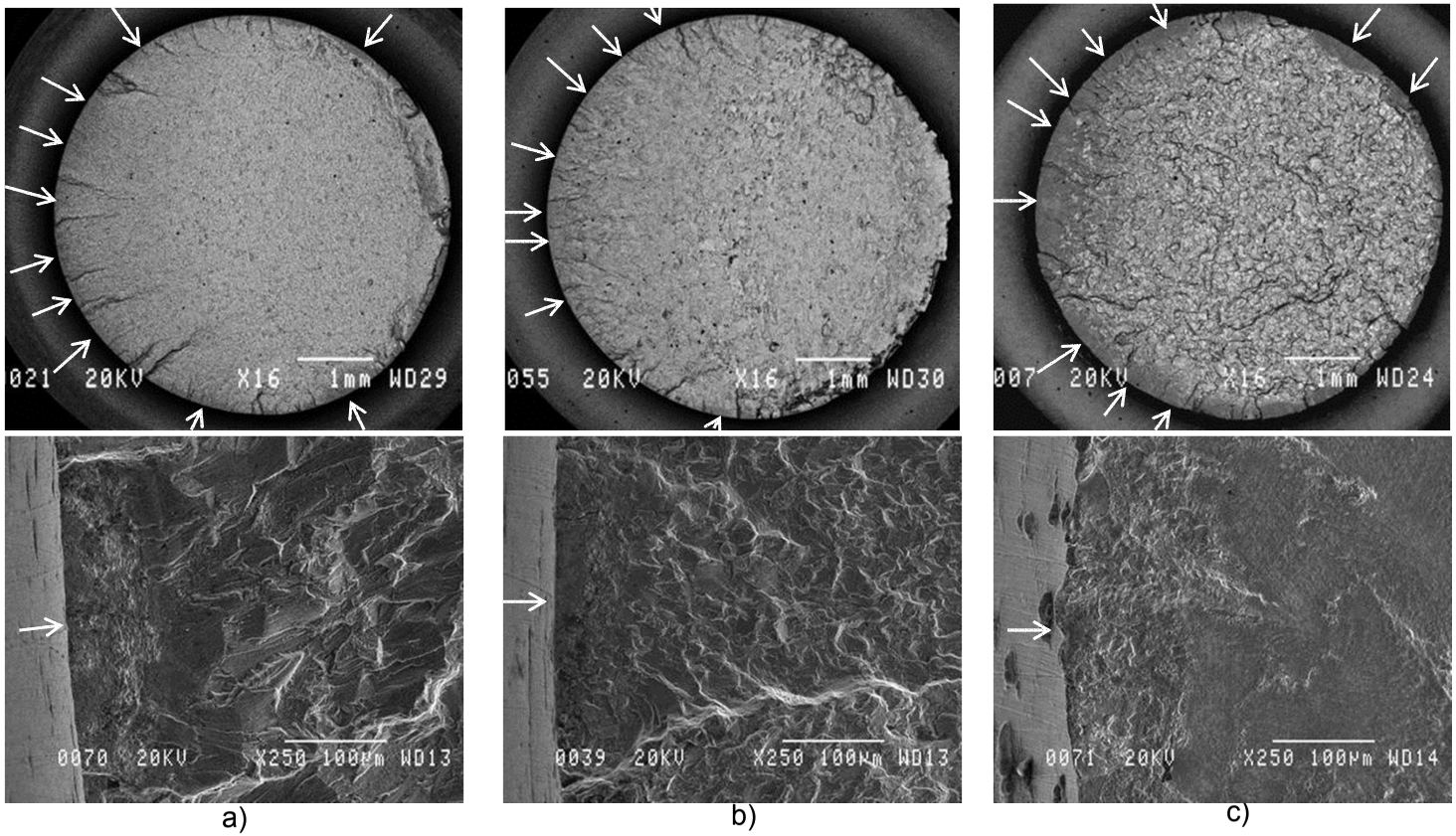

Fig. 27.—Comparisons of typical fatigue failure initiation modes for notch fatigue with a 90 s dwell at minimum stress, 704 °C-793 MPa: a) LSHR (15 µm), b) LSHR (50 µm), c) Mar-M247LC (60 µm), showing transgranular surface cracks at exposed surfaces.

.

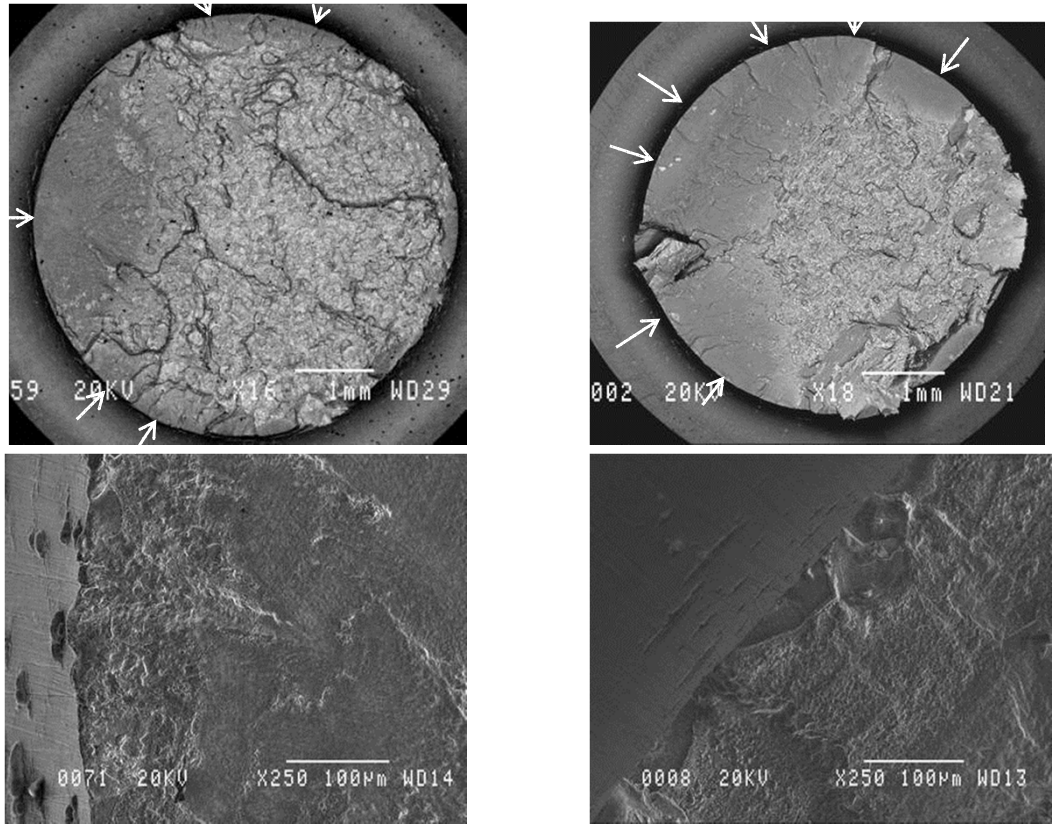

d) e)

Fig. 27 (cont.).—Comparisons of typical fatigue failure initiation modes for notch fatigue with a 90 s dwell at minimum stress, 704 °C-793 MPa: d) Mar-M247LC (1200 µm), e) LDS-1101+Hf (single crystal), showing transgranular surface cracks at exposed surfaces.

.

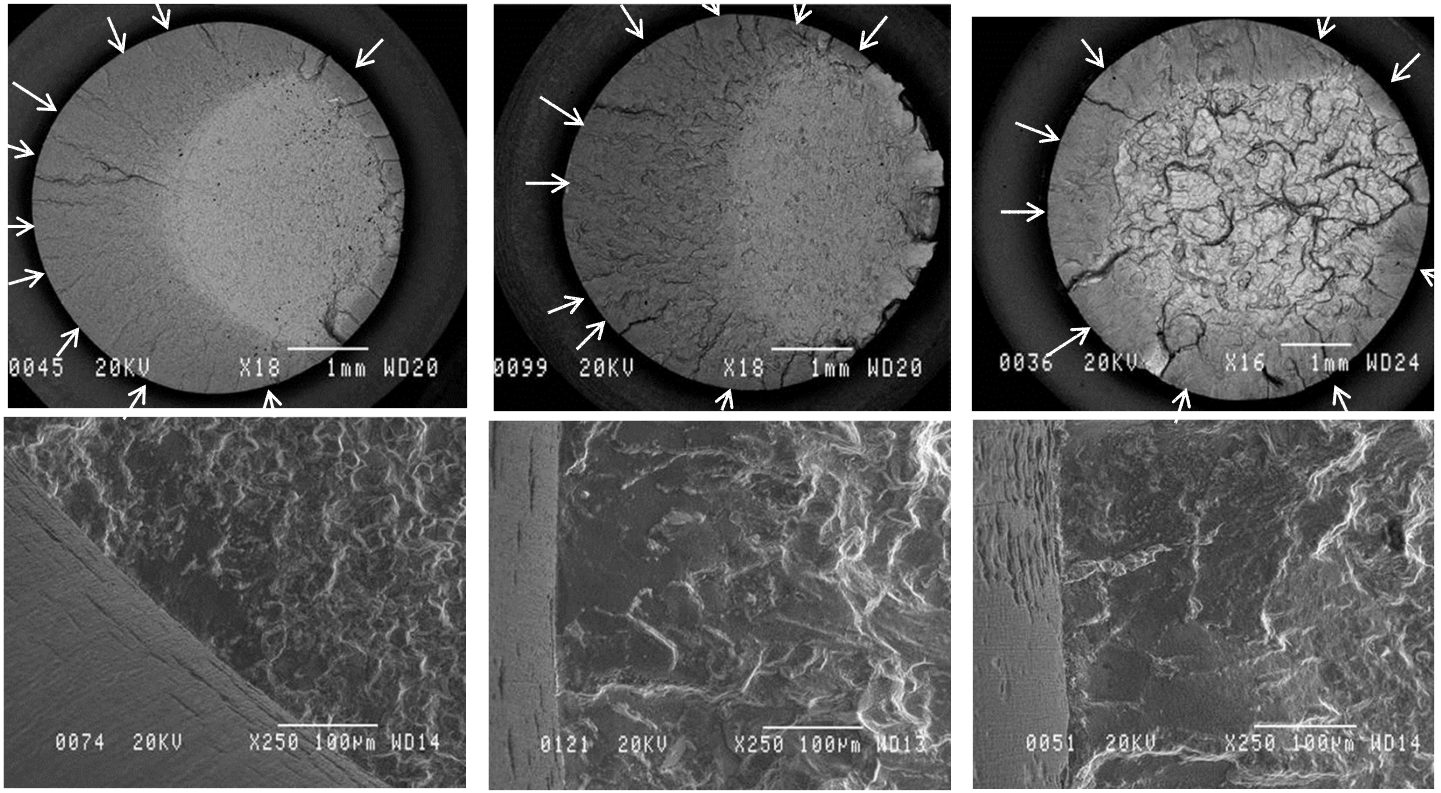

Fig. 28.—Comparisons of typical fatigue failure modes for notch fatigue with a 90 s dwell at minimum stress, 815 °C-620 MPa: a) LSHR (15 µm), b) LSHR (50 µm), c) Rene′ 80 (200 µm), showing transgranular cracks at oxidized surfaces.

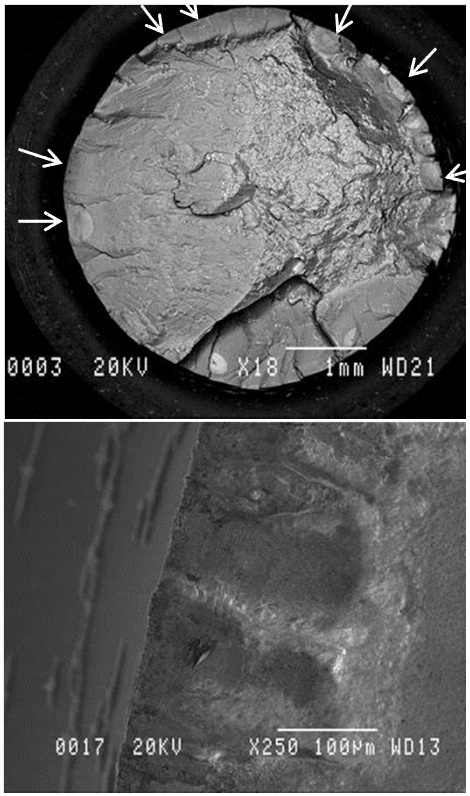

d)

Fig. 28 (cont.).—Comparisons of typical fatigue failure modes for notch fatigue with a 90 s dwell at minimum stress, 815 °C-620 MPa: d) LDS-1101+Hf (single crystal), showing cracks at oxidized surfaces.

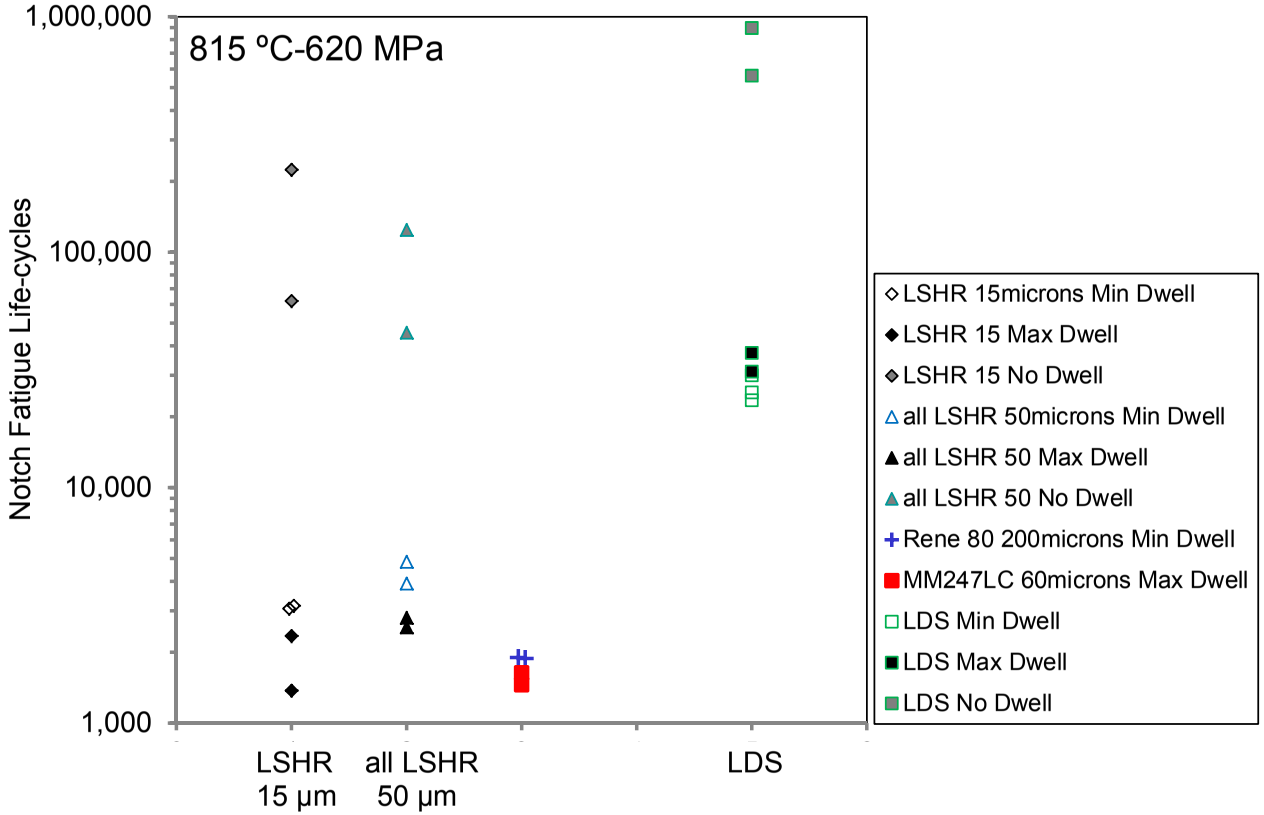

Fig. 29.—Comparisons of notch fatigue lives at 815 °C and 620 MPa maximum stress for cycles having 90 s dwells at maximum stress (Max Dwell) and minimum stress (Min Dwell) versus no dwells.

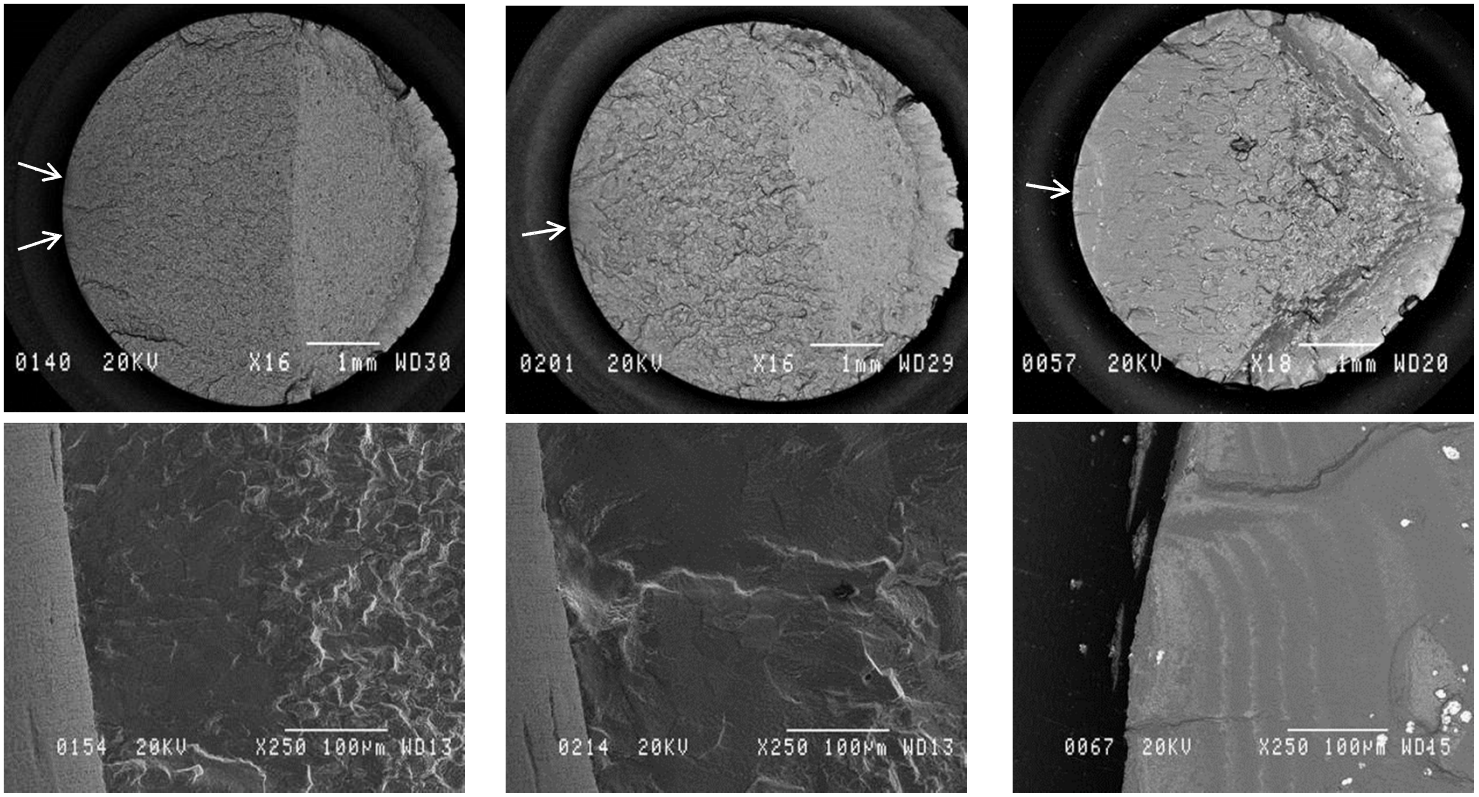

Fig. 30.—Comparisons of typical fatigue failure modes showing cracks for notch fatigue tests with no dwell at 815 °C-620 MPa: a) LSHR (15 µm), intergranular surface crack initiation, b) all LSHR at 50 µm, intergranular surface crack initiation, c) LDS-1101+Hf (single crystal), MC carbide surface crack initiation.

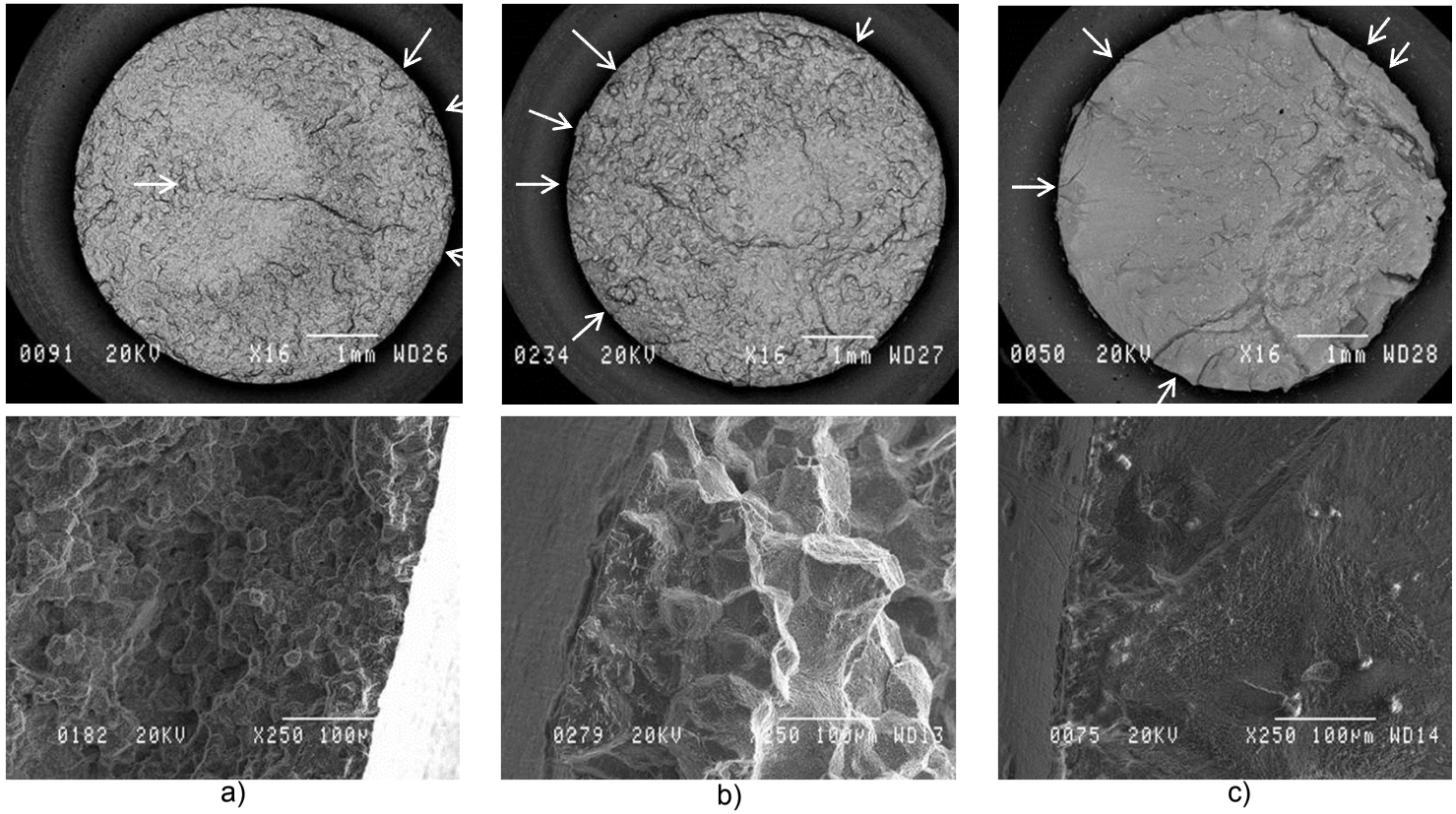

Fig. 31.—Comparisons of typical fatigue failure modes showing cracks for notch fatigue tests with 90 s dwell at maximum stress at 815 °C-620 MPa: a. LSHR (15 µm), surface and internal intergranular cracks, b) all LSHR at 50 µm, surface intergranular cracks, c) LDS-1101+Hf (single crystal), surface oxide cracks.

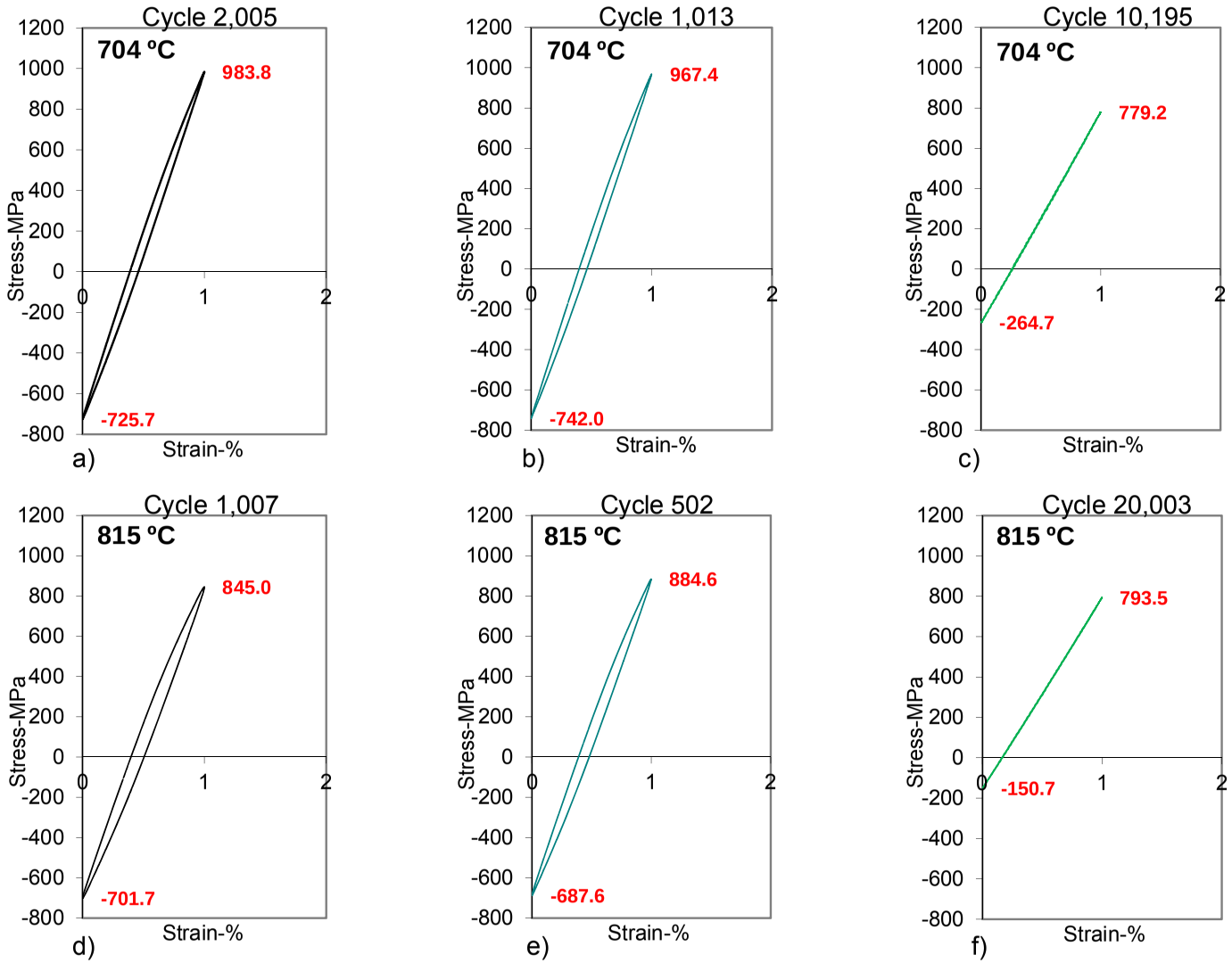

Fig. 32.—Stabilized stress-strain hysteresis loops of uniform gage specimens in strain-controlled fatigue tests at 1 percent strain range, stabilized maximum and minimum stresses indicated in red: a) LSHR (15 μm) at 704 °C, b) LSHR (50 μm) at 704 °C, c) LDS-1101+Hf at 704 °C, d) LSHR (15 μm) at 815 °C, e) LSHR (50 μm) at 815 °C, f) LDS-1101+Hf at 815 °C.

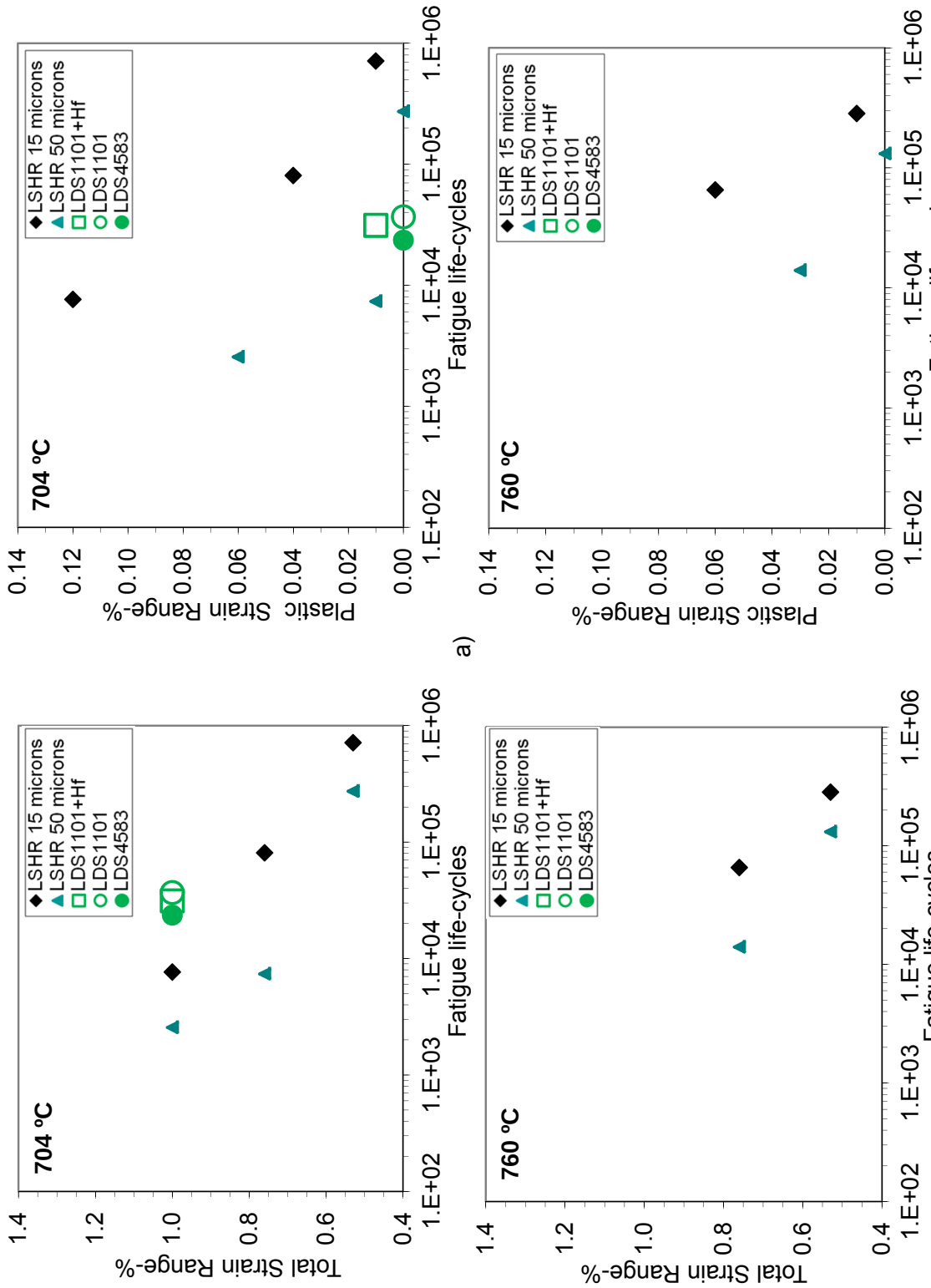

Fig. 33.—Fatigue life versus total strain range and plastic strain range in tests of uniform gage specimens at: a) 704 °C, b) 760 °C.

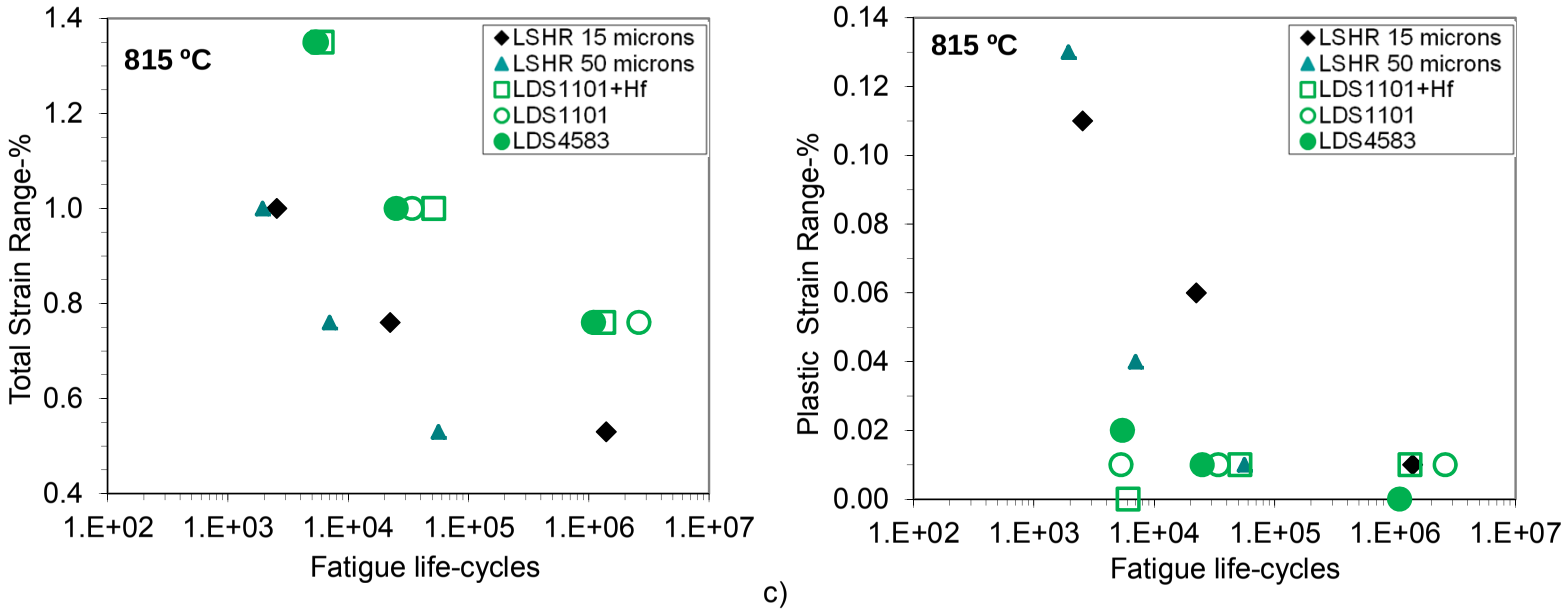

c)

Fig. 33 (cont.).—Fatigue life versus total strain range and plastic strain range in tests of uniform gage specimens at: c) 815 °C.

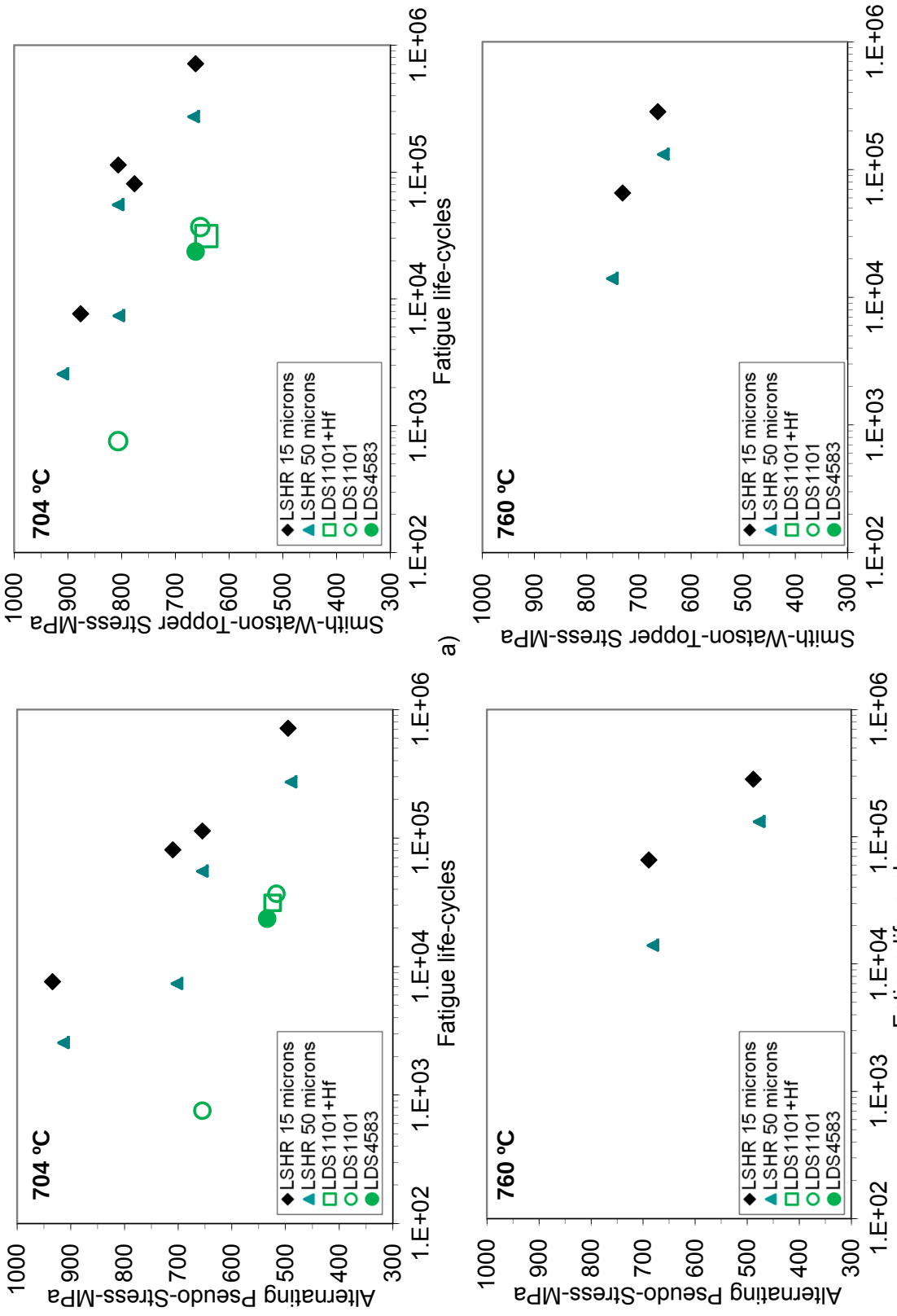

Fig. 34.—Fatigue life versus alternating pseudo-stress and Smith-Watson-Topper stress of uniform gage specimens in tests of uniform gage specimens at: a) 704 °C, b) 760 °C.

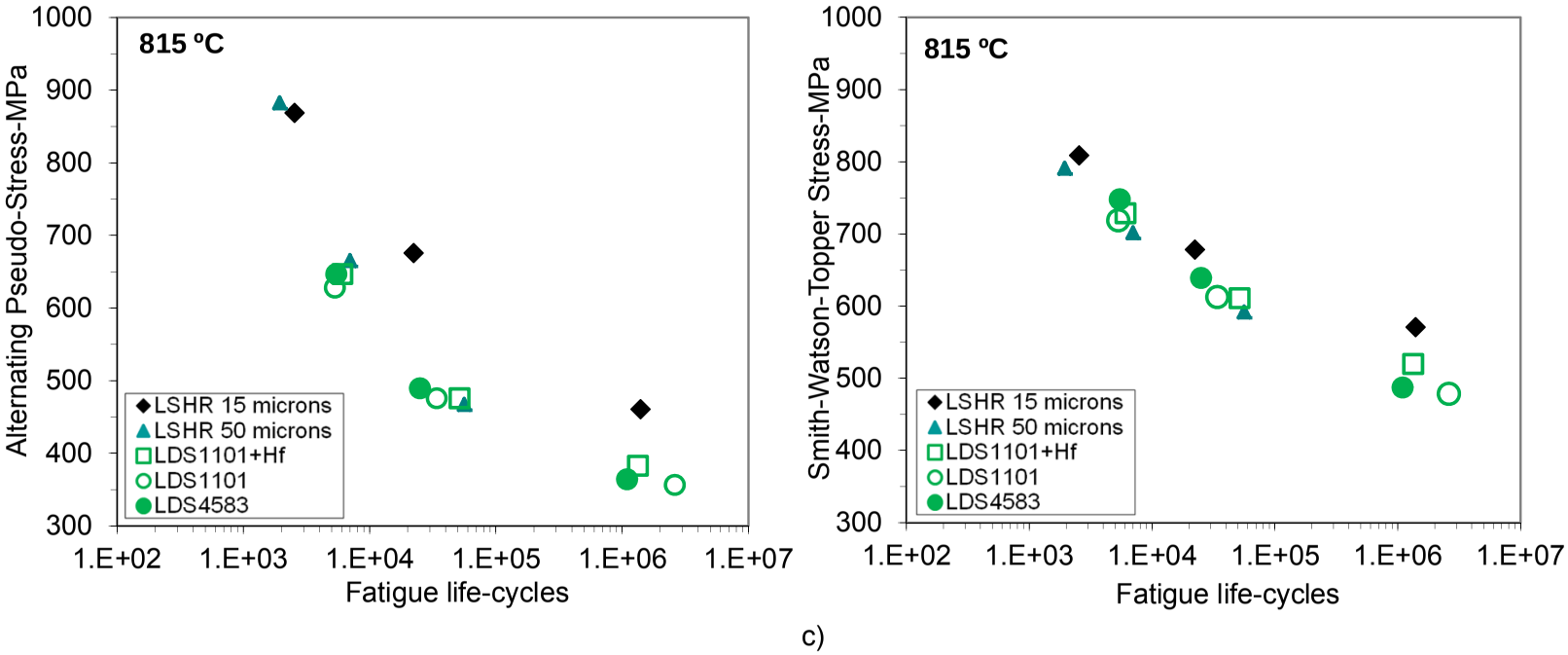

c)

Fig. 34 (cont.).—Fatigue life versus alternating pseudo-stress and Smith-Watson-Topper stress of uniform gage specimens in tests of uniform gage specimens at: c) 815 °C.

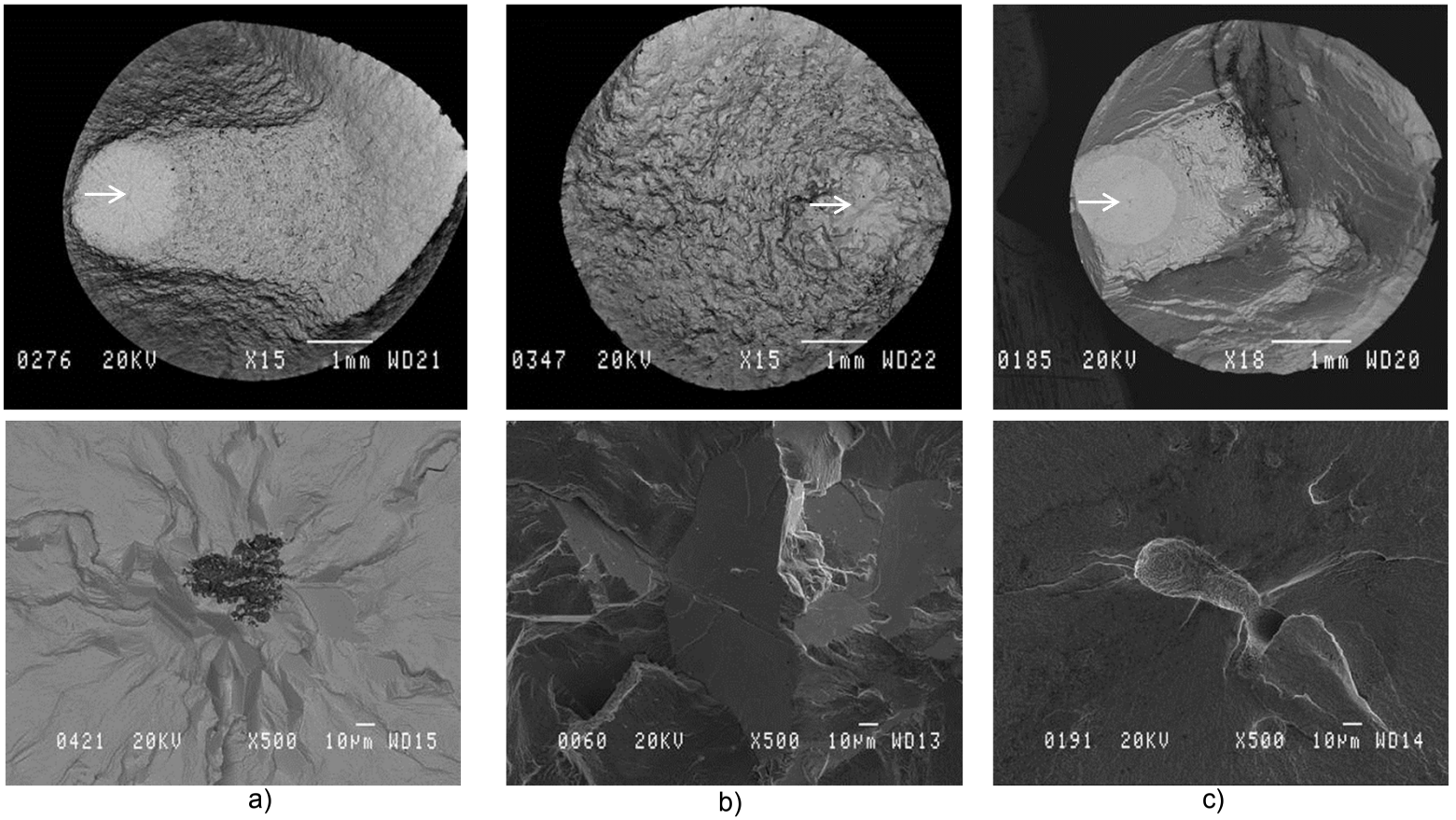

Fig. 35.—Comparisons of typical uniform gage fatigue failure initiation modes at 704 °C: a) LSHR (15 μm), internal inclusion, b) LSHR (50 μm), internal grain facet, c) LDS-1101+Hf, internal pore.

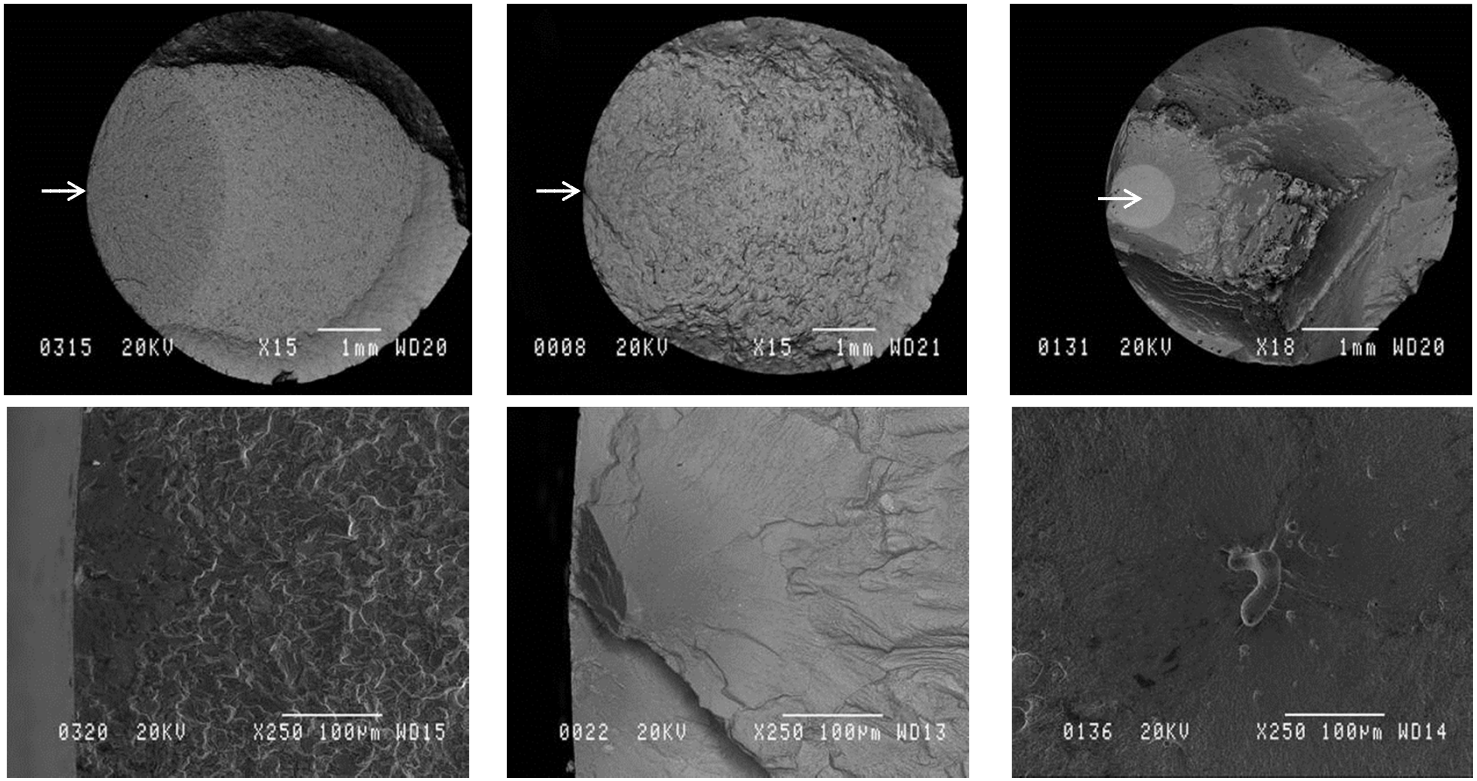

Fig. 36.—Comparisons of typical fatigue failure modes at 815 °C: a) LSHR (15 µm), surface oxide, b) LSHR (50 µm), surface facet, c) LDS-1101+Hf, internal pore.

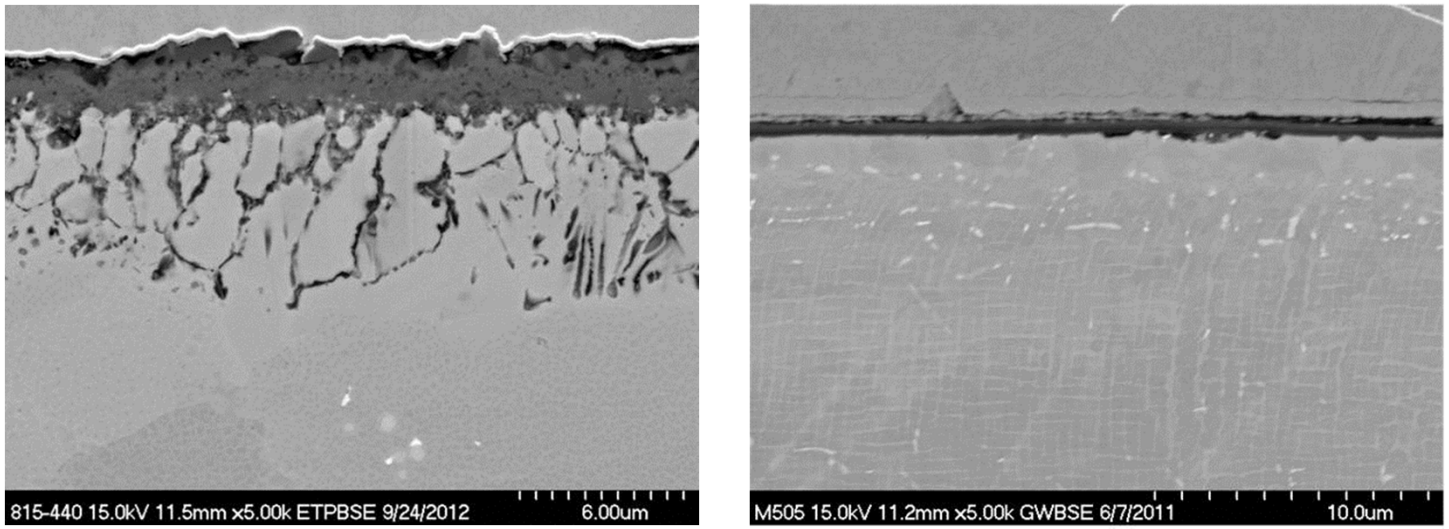

a) b)

Fig. 37.—Comparison of surfaces for specimens exposed 815 °C for 440 h: a) LSHR (15 μm), b) LDS-1101+Hf (single crystal).

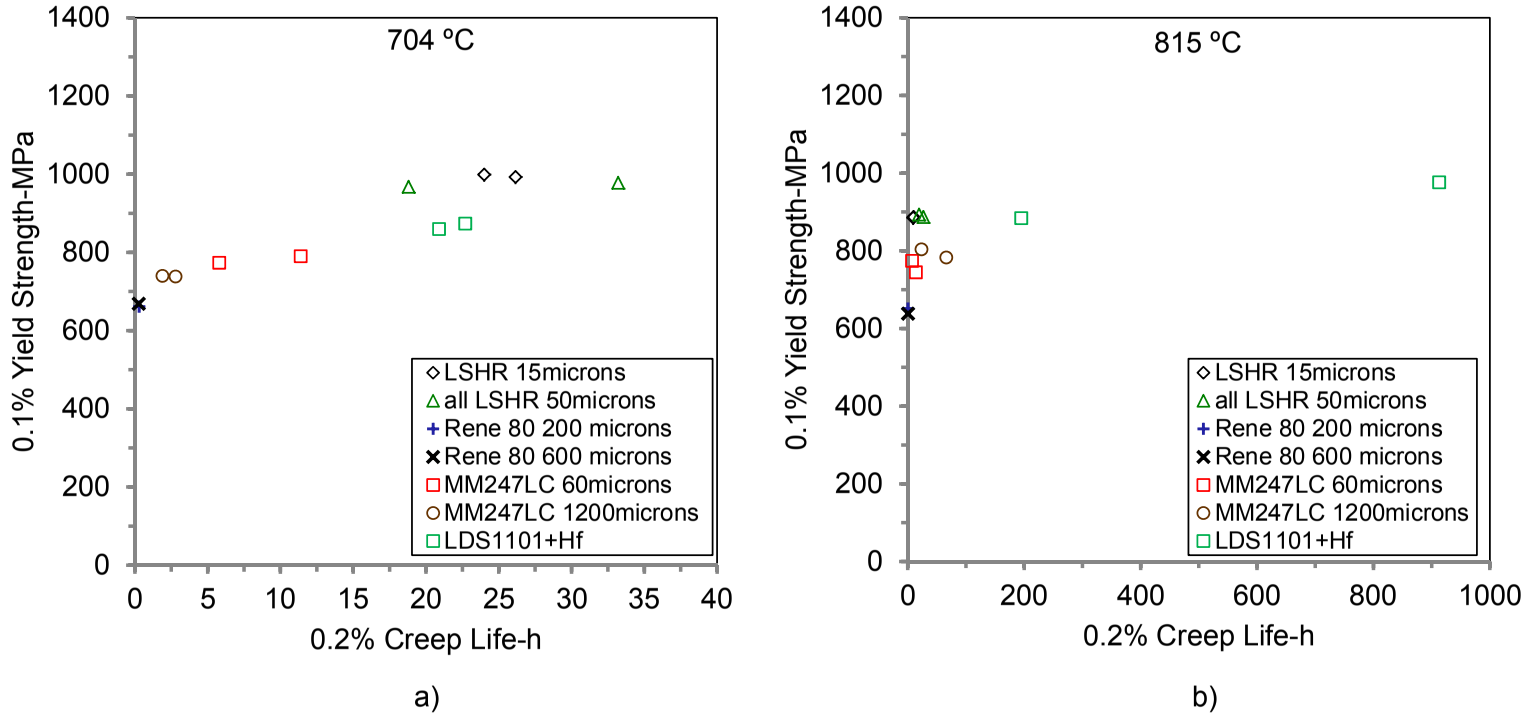

Fig 38.—Comparison of 0.1% tensile yield strength versus 0.2% creep life: a) 704 °C, b) 815 °C.

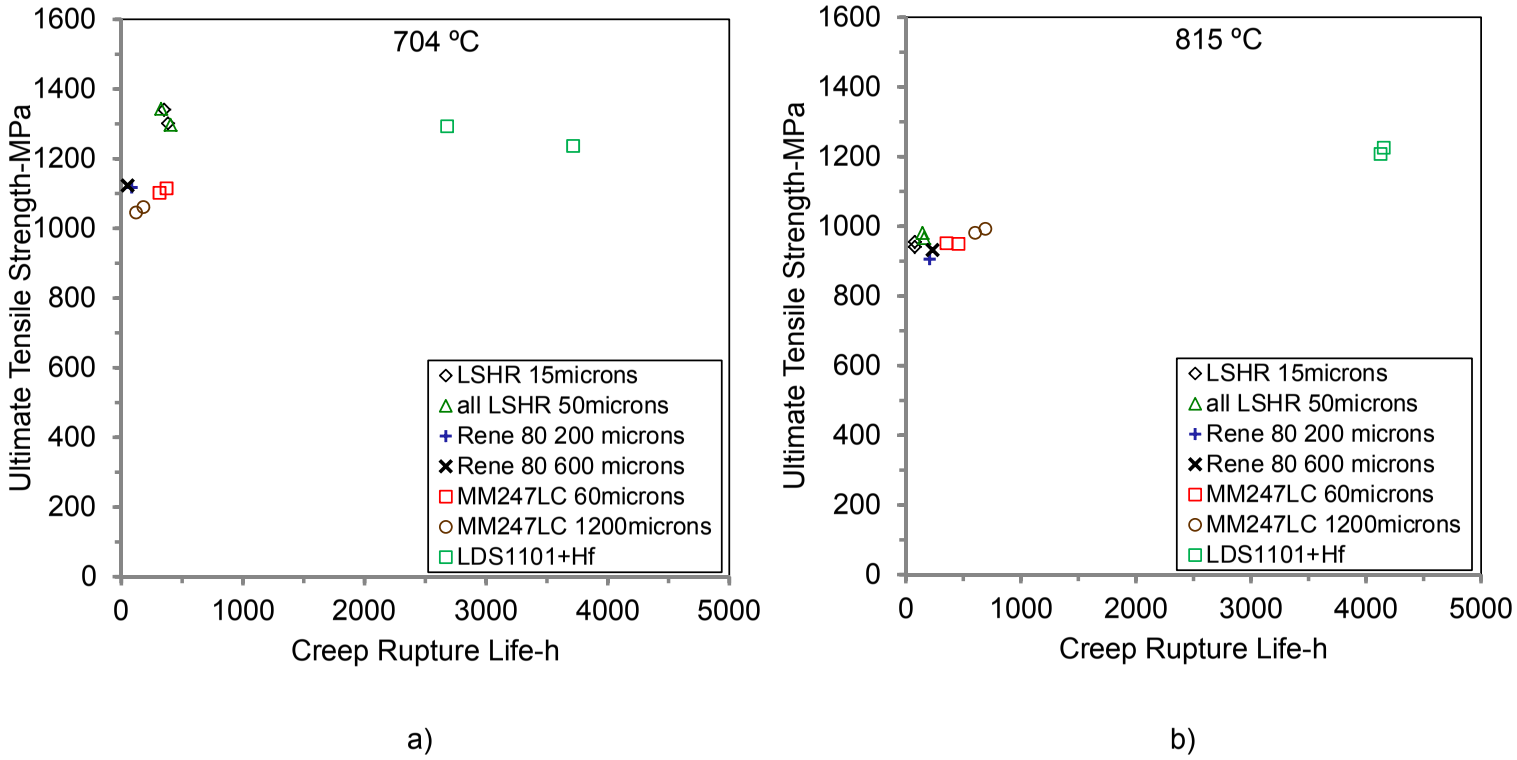

Fig. 39.—Comparison of ultimate tensile strength versus creep rupture life: a) 704 °C, b) 815 °C.

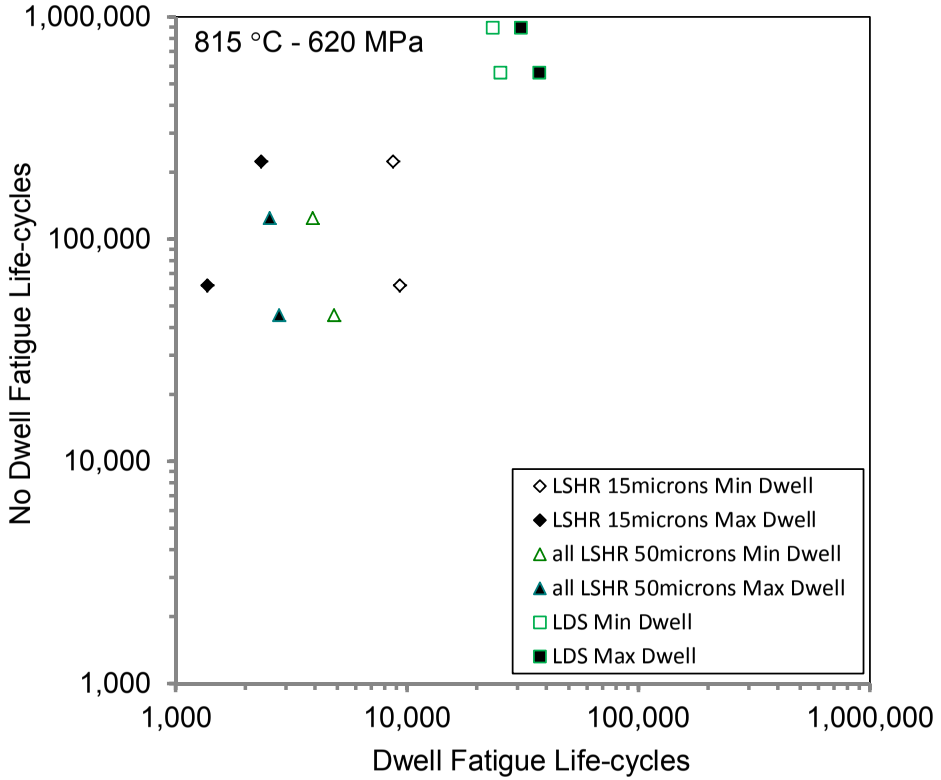

Fig. 40.—Comparison of no dwell versus minimum (min) dwell and maximum (max) dwell fatigue lives at 815 °C and maximum applied stress of 620 MPa.

REPORT DOCUMENTATION PAGE	Form Approved OMB No. 0704-0188

1. REPORT DATE *(DD-MM-YYYY)*	2. REPORT TYPE	3. DATES COVERED *(From - To)*
01-07-2013	Technical Memorandum	

4. TITLE AND SUBTITLE
The Mechanical Properties of Candidate Superalloys for a Hybrid Turbine Disk

5a. CONTRACT NUMBER

5b. GRANT NUMBER

5c. PROGRAM ELEMENT NUMBER

6. AUTHOR(S)
Gabb, Timothy, P.; MacKay, Rebecca, A.; Draper, Susan, L.; Sudbrack, Chantal, K.; Nathal, Michael, V.

5d. PROJECT NUMBER

5e. TASK NUMBER

5f. WORK UNIT NUMBER
WBS 473452.02.03.05.04.01.01

7. PERFORMING ORGANIZATION NAME(S) AND ADDRESS(ES)
National Aeronautics and Space Administration
John H. Glenn Research Center at Lewis Field
Cleveland, Ohio 44135-3191

8. PERFORMING ORGANIZATION REPORT NUMBER
E-18713

9. SPONSORING/MONITORING AGENCY NAME(S) AND ADDRESS(ES)
National Aeronautics and Space Administration
Washington, DC 20546-0001

10. SPONSORING/MONITOR'S ACRONYM(S)
NASA

11. SPONSORING/MONITORING REPORT NUMBER
NASA/TM-2013-217901

12. DISTRIBUTION/AVAILABILITY STATEMENT
Unclassified-Unlimited
Subject Category: 07
Available electronically at http://www.sti.nasa.gov
This publication is available from the NASA Center for AeroSpace Information, 443-757-5802

13. SUPPLEMENTARY NOTES

14. ABSTRACT
The mechanical properties of several cast blade superalloys and one powder metallurgy disk superalloy were assessed for potential use in a dual alloy hybrid disk concept of joined dissimilar bore and web materials. Grain size was varied for each superalloy class. Tensile, creep, fatigue, and notch fatigue tests were performed at 704 to 815 °C. Typical microstructures and failure modes were determined. Preferred materials were then selected for future study as the bore and rim alloys in this hybrid disk concept. Powder metallurgy superalloy LSHR at 15 µm grain size and single crystal superalloy LDS-1101+Hf were selected for further study, and future work is recommended to develop the hybrid disk concept.

15. SUBJECT TERMS
Gas turbine engines; Rotating disks; Heat resistant alloys; Fatigue

16. SECURITY CLASSIFICATION OF:			17. LIMITATION OF ABSTRACT	18. NUMBER OF PAGES	19a. NAME OF RESPONSIBLE PERSON
a. REPORT	b. ABSTRACT	c. THIS PAGE			STI Help Desk (email:help@sti.nasa.gov)
U	U	U	UU	72	19b. TELEPHONE NUMBER *(include area code)* 443-757-5802